

Electronic Thesis and Dissertation Repository

---

2-18-2014

## Control of Wind Energy Conversion Systems for Large-Scale Integration with the Power System

Omid Alizadeh  
*The University of Western Ontario*

Supervisor  
Dr. Amirnaser Yazdani  
*The University of Western Ontario*

Graduate Program in Electrical and Computer Engineering  
A thesis submitted in partial fulfillment of the requirements for the degree in Doctor of Philosophy  
© Omid Alizadeh 2014

Follow this and additional works at: <https://ir.lib.uwo.ca/etd>



Part of the [Power and Energy Commons](#)

---

### Recommended Citation

Alizadeh, Omid, "Control of Wind Energy Conversion Systems for Large-Scale Integration with the Power System" (2014). *Electronic Thesis and Dissertation Repository*. 1907.  
<https://ir.lib.uwo.ca/etd/1907>

This Dissertation/Thesis is brought to you for free and open access by Scholarship@Western. It has been accepted for inclusion in Electronic Thesis and Dissertation Repository by an authorized administrator of Scholarship@Western. For more information, please contact [wlsadmin@uwo.ca](mailto:wlsadmin@uwo.ca).

CONTROL OF WIND ENERGY CONVERSION SYSTEMS FOR  
LARGE-SCALE INTEGRATION WITH THE POWER SYSTEM  
(Thesis format: Monograph)

by

Omid Alizadeh

Graduate Program in Electrical and Computer Engineering

A thesis submitted in partial fulfillment  
of the requirements for the degree of  
Doctor of Philosophy

The School of Graduate and Postdoctoral Studies  
Western University  
London, Ontario, Canada

© Omid Alizadeh 2014

# Abstract

This thesis is mainly focused on (i) mathematical modeling and real power control of a direct-drive wind energy conversion system (WECS) that employs a high-pole permanent-magnet synchronous generator (PMSG), and (ii) the contribution of the WECS to the frequency regulation process in a host power system. In the first part, a strategy is proposed for real power control of the WECS, which augments the maximum power-point tracking (MPPT) feature of modern WECSs. The proposed strategy is based on rapid torque control, rather than the (slow) pitch-angle control. Moreover, a supplementary damping scheme is presented and tuned for the proposed power control strategy, based on a detailed mathematical model and eigenvalue analysis of the WECS. The supplementary mechanism damps the WECS drive-train oscillations and maintains its internal stability, even if its output power is regulated. The thesis also presents an alternative control structure for the WECS which mitigates the sensitivity of the WECS output power to power fluctuations caused by wind speed variations and drive-train oscillatory modes. Thus, a damping strategy and a tuning procedure are proposed for the aforementioned control structure, such that a stable performance of the WECS over the operating range is ensured.

In the second part of the thesis, an enhanced control strategy is proposed that enables a WECS to contribute to frequency regulation process by effectively using its available generation reserve and the kinetic energy of its rotor, such that the stability of the WECS is maintained over the operating range. The performances of direct-drive PMSG-based WECSs with the proposed control strategy are examined in an example host power system and the impact of wind speed intermittency on the frequency responses of WECSs is assessed, based on which the parameters of the proposed control are adjusted to maintain the reliability of the example power system in response to a specific contingency event, under different wind speed regimes. The effectiveness of the proposed control strategies is demonstrated through time-domain simulation studies conducted in the PSCAD/EMTDC software environment.

**Keywords:** Control, Damping, Drive-Train Torsional Modes, Frequency Response, Grid Support, Power Electronics, Real Power Control, Voltage-Sourced Converter, Wind Energy Conversion Systems.

I dedicate this work to my parents

# Acknowledgement

I would like to express my sincere gratitude to Dr. Amirnaser Yazdani for his excellent supervision, bright ideas, and continuous encouragement throughout the course of this research. It has been a great privilege for me to pursue my higher education under his supervision.

Also, the financial support provided by Dr. Amirnaser Yazdani and Western University is gratefully acknowledged.

# Contents

<b>Abstract</b>	<b>ii</b>
<b>Dedication</b>	<b>iii</b>
<b>Acknowledgements</b>	<b>iv</b>
<b>List of Figures</b>	<b>ix</b>
<b>List of Tables</b>	<b>xii</b>
<b>List of Appendices</b>	<b>xiii</b>
<b>List of Abbreviations</b>	<b>xiv</b>
<b>List of Nomenclature</b>	<b>xv</b>
<b>1 Introduction</b>	<b>1</b>
1.1 Introduction to Wind Energy Conversion Systems . . . . .	1
1.1.1 Wind Turbine Concepts . . . . .	2
Aerodynamic Drag and Lift . . . . .	2
Vertical-Axis and Horizontal-Axis Wind Turbines . . . . .	3
Number of Blades . . . . .	3
Betz Limit . . . . .	4
Upwind and Downwind Turbines . . . . .	4
1.1.2 Components of Wind Energy Conversion Systems . . . . .	5
1.1.3 Aerodynamic Torque Control . . . . .	5
1.1.4 Types of Wind Energy Conversion Systems . . . . .	6
1.1.5 Direct-Drive PMSG-Based WECSs . . . . .	8
1.1.6 Operating Regime . . . . .	9
1.1.7 Grid Integration Requirements of WECSs . . . . .	10

1.2	Statement of Problem and Thesis Objectives . . . . .	12
1.3	Background . . . . .	14
1.3.1	Real Power Control in WECSs . . . . .	14
	Power Generation Control and Curtailment of WECSs . . . . .	14
	Torsional Dynamics of Modern WECSs . . . . .	15
	Multi-Mass Modeling of a WECS Drive-Train . . . . .	18
1.3.2	Frequency Regulation in Power Systems . . . . .	20
	Power Balance Issue . . . . .	21
	Frequency Regulation with CPPs . . . . .	22
	Frequency Regulation with a High Penetration of Wind Power . . . . .	25
1.3.3	Generation Reserves in Power Systems . . . . .	28
	Generation Reserve and Wind Power . . . . .	28
	Capacity Factor . . . . .	29
1.4	Thesis Contributions . . . . .	30
1.5	Thesis Outline and Related Literature Review . . . . .	31
	Real-Power Control Strategies in WECSs . . . . .	32
	Damping Drive-Train Torsional Modes . . . . .	33
	Contribution of WECSs to Frequency Regulation . . . . .	34
1.6	Summary and Conclusion . . . . .	37
<b>2</b>	<b>Real Power Control of a Direct-Drive PMSG-Based WECS</b>	<b>39</b>
2.1	Introduction . . . . .	39
2.2	Structure of the Direct-Drive WECS . . . . .	40
2.3	Mathematical Model and Control Schemes . . . . .	41
	2.3.1 Aerodynamic Model of the Turbine . . . . .	41
	2.3.2 Drive-Train . . . . .	42
	2.3.3 Permanent-Magnet Synchronous Generator . . . . .	42
2.4	Control Strategy and Modes of Operation . . . . .	45
	2.4.1 MPPT Mode of Operation . . . . .	46
	2.4.2 Controlled-Power Mode of Operation . . . . .	47
2.5	Eigenvalue Analysis . . . . .	48
2.6	Damping Strategy . . . . .	52
	2.6.1 Structure . . . . .	52
	2.6.2 Design . . . . .	52
	2.6.3 Eigenvalue Analysis . . . . .	55

2.7	Case Studies . . . . .	59
2.7.1	Start-up Process and Operation in the MPPT Mode . . . . .	60
2.7.2	Response to Operation Mode and Wind Speed Changes . . . . .	62
2.8	Summary and Conclusion . . . . .	65
<b>3</b>	<b>An Alternative Control Structure and Damping Strategy</b>	<b>66</b>
3.1	Introduction . . . . .	66
3.2	Control Structure of the WECS . . . . .	67
3.3	Basic WECS Control . . . . .	68
3.3.1	Drive-Train Model . . . . .	68
3.3.2	Control for Fast dc-Link Voltage Regulation . . . . .	69
3.3.3	Control for Slow dc-Link Voltage Regulation . . . . .	70
3.4	Control Strategy to Damp the Drive-Train Torsional Modes . . . . .	73
3.4.1	Proposed Control Strategy . . . . .	73
3.4.2	Control Tuning Procedure . . . . .	75
	1) Initial Values of Compensator Parameters . . . . .	75
	2) Damping Gain . . . . .	75
	3) Final Compensator Zero . . . . .	76
	4) Final Compensator Gain . . . . .	77
3.4.3	Behavior of the WECS under Different Compensator Gains . . . . .	78
3.5	Simulation Results . . . . .	80
3.6	A Comparative Discussion on the Presented Control Strategies . . . . .	82
3.7	Summary and Conclusion . . . . .	84
<b>4</b>	<b>Enhanced Control of WECSs for Contribution to Frequency Response</b>	<b>85</b>
4.1	Introduction . . . . .	85
4.2	Control Strategy for Frequency Regulation . . . . .	86
4.2.1	Droop-Based Control . . . . .	87
4.2.2	Inertia-Emulating Control . . . . .	88
4.2.3	Pitch-Angle Control . . . . .	89
4.2.4	Description of the Proposed Control . . . . .	89
4.3	Case Studies . . . . .	91
4.3.1	Switched Model of the Example Wind Plant . . . . .	93
4.3.2	Power System with Only CPPs . . . . .	94
4.3.3	No Frequency Response from the Wind Plant . . . . .	95



4.3.4	Frequency Regulation at the Average Wind Speed . . . . .	96
4.3.5	Frequency Regulation at Different Wind Speeds . . . . .	99
4.3.6	Impact of Wind Speed Intermittency on Frequency Regulation . .	101
4.4	Summary and Conclusion . . . . .	105
<b>5</b>	<b>Summary, Conclusion, and Future Work</b>	<b>106</b>
5.1	Summary . . . . .	106
5.2	Conclusion . . . . .	107
5.3	Future Work . . . . .	108
<b>A</b>	<b>Parameters of the Example WECS in Chapters 2 and 3</b>	<b>110</b>
<b>B</b>	<b>Analytical Forms of Matrices</b>	<b>112</b>
<b>C</b>	<b>Parameters of the Example Wind Plant and CPPs in Chapter 4</b>	<b>115</b>
	<b>Bibliography</b>	<b>117</b>
	<b>Curriculum Vitae</b>	<b>125</b>

# List of Figures

1.1	Examples of wind turbine concepts [8]. . . . .	2
1.2	Main components of a wind energy conversion system. . . . .	5
1.3	Commercial configurations of wind energy conversion systems; a) type A, b) type B, c) type C, and d) type D. . . . .	7
1.4	Power curve of Vestas V90 3 MW wind turbine [18]. . . . .	10
1.5	The electrical frequency at the wind farm [25]; at $t = 0.4$ s the wind farm was disconnected from the transmission network. . . . .	16
1.6	Undamped oscillations of the rotor speed in a WECS without a damping mechanism. . . . .	18
1.7	A typical frequency response following a sudden loss of generation. . . . .	22
1.8	Tip-speed ratio control in a WECS. . . . .	32
1.9	Hill-climb search control in a WECS. . . . .	32
1.10	Power signal feedback control in a WECS. . . . .	33
2.1	Simplified schematic diagram of the direct-drive WECS. . . . .	40
2.2	Block diagram of the PMSG torque control scheme. . . . .	43
2.3	Block diagram of the basic power control scheme. . . . .	45
2.4	Characteristic curves of a wind turbine for a wind speed and two different values of pitch angle. . . . .	47
2.5	Block diagram illustrating the generation of the power setpoint. . . . .	48
2.6	Absolute value of the real part of $\mathbf{A}_1$ dominant eigenvalue as a function of $k_{p3}$ and $k_{i3}$ . . . . .	50
2.7	Block diagram illustrating the implementation of the damping scheme. . . . .	52
2.8	Control block diagram of the damping scheme. . . . .	52
2.9	Variations of the frequency of unstable mode as a function of the normalized power command in the CP mode of operation. . . . .	53
2.10	Nyquist plot of the open-loop frequency response of Figure 2.8, when $C(s) = k_d = 10^7$ . . . . .	55

2.11	Migration plot of the (initially) unstable eigenvalues in the CP mode for different values of $k_d$ . . . . .	57
2.12	Migration plot of the eigenvalues for different operating points. . . . .	59
2.13	Response to operation mode change from MPPT to CP. . . . .	60
2.14	Start-up process and subsequent operation of the WECS in the MPPT mode. . . . .	61
2.15	Response to changes in the operation mode and wind speed. . . . .	63
2.16	Response to changes in the operation mode and wind speed (cont.). . . . .	64
3.1	Schematic diagram of the alternative control strategy for the direct-drive PMSG-based WECS. . . . .	67
3.2	Block diagram of the dc-link voltage control scheme. . . . .	68
3.3	Control block diagram of the energy capture subsystem. . . . .	70
3.4	Migration plot of the closed-loop poles without damping mechanism; arrows illustrate increase in $k_c$ . . . . .	72
3.5	Migration plot of the closed-loop poles without damping mechanism; $z = 3$ ( $\square$ trace), $z = 4$ ( $\times$ trace), $z = 5$ ( $\nabla$ trace), and $z = 6$ ( $+$ trace); arrows illustrate increase in $k_c$ . . . . .	73
3.6	Block diagram illustrating the implementation of proposed control scheme. . . . .	74
3.7	Control block diagram of energy capture subsystem with proposed control scheme. . . . .	74
3.8	Migration plot of the closed-loop poles with the proposed control scheme; arrows illustrate increase in $k_d$ . . . . .	76
3.9	Migration plot of the closed-loop poles with the proposed control scheme; $z = 3$ ( $\square$ trace), $z = 4$ ( $\times$ trace), $z = 5$ ( $\nabla$ trace), and $z = 6$ ( $+$ trace); arrows illustrate increase in $k_d$ . . . . .	76
3.10	Migration plot of the closed-loop poles with the proposed control scheme; arrows illustrate increase in $k_c$ . . . . .	77
3.11	Response to a change from the MPPT mode to the CP mode. . . . .	78
3.12	Response to a switch from the proposed control to the basic control. . . . .	79
3.13	Migration plot of the closed-loop poles for different operating points. . . . .	80
3.14	Response to changes in operation mode and wind speed. . . . .	81
3.15	Responses to changes in power command under turbulent wind speed; (a) with the control strategy presented in Chapter 2, (b) with the control strategy presented in this chapter. . . . .	83

4.1	Block diagram illustrating the generation of the WECS output power set-point. . . . .	86
4.2	Droop characteristic of the WECS. . . . .	87
4.3	Characteristic curves of a wind turbine for two wind speeds. . . . .	89
4.4	The example power systems. . . . .	92
4.5	Response of the example power system, with only CPPs. . . . .	94
4.6	Response of the example power system, without frequency response from the wind plant. . . . .	95
4.7	Response of the example power system, when the wind plant provides frequency response. . . . .	97
4.8	Frequency responses of the example power systems to the loss of CPP2. . . . .	98
4.9	Proposed droop characteristic for the example wind plant. . . . .	99
4.10	Responses of the example power system to a sudden loss of CPP2, at different wind speeds. . . . .	101
4.11	Responses of the example power system to the wind speed intermittency. . . . .	103
4.12	Response of the example power system with different values of the inertia-emulating control parameters. . . . .	104
4.13	Frequency response of the system at different wind speeds. . . . .	105

# List of Tables

1.1	Typical Inertia Constants of Different Power Plants . . . . .	26
2.1	Eigenvalues of the Energy Capture Subsystem. . . . .	51
2.2	Eigenvalues of the Energy Capture Subsystem with the Damping Scheme. . . . .	58
A.1	Wind Turbine Parameters . . . . .	110
A.2	PMSG Parameters . . . . .	111
A.3	Compensators and Other Parameters . . . . .	111
C.1	Conventional Power Plants Parameters . . . . .	115
C.2	Wind Plant Model - Turbine Parameters . . . . .	116
C.3	Wind Plant Model - Generator Parameters . . . . .	116

# List of Appendices

Appendix A Parameters of the Example WECS in Chapters 2 and 3 . . . . .	110
Appendix B Analytical Forms of Matrices . . . . .	112
Appendix C Parameters of the Example Wind Plant and CPPs in Chapter 4 . . .	115

## Abbreviations and Symbols

AC	Alternating Current
CP	Controlled Power
CPP	Conventional Power Plant
DC	Direct Current
ERCOT	Electric Reliability Council of Texas
HCS	Hill-Climb Search
MPPT	Maximum Power-Point Tracking
ROCOF	Rate of Change of Frequency
TSR	Tip-Speed Ratio
PI	Proportional-Integral
PMSG	Permanent-Magnet Synchronous Generator
PSCAD	Power System Computer-Aided Design
PSF	Power Signal Feedback
PSS	Power System Stabilizer
PWM	Pulse-Width Modulation
VSC	voltage-sourced converter
WECS	Wind Energy Conversion System

# Nomenclature

$C_p$	Turbine power efficiency	unitless
$R$	Turbine radius	m
$\beta$	Turbine pitch angle	degree
$\lambda$	Turbine tip-speed ratio	rad
$\rho$	Air mass density	kg/m <sup>3</sup>
$v_w$	Wind speed	m/s
$T_{tur}$	Turbine mechanical torque	Nm
$P_{tur}$	Turbine mechanical power	W
$J_t$	Turbine moment of inertia	kgm <sup>2</sup>
$J_r$	PMSG moment of inertia	kgm <sup>2</sup>
$\omega_t$	Turbine angular speed	rad/s
$\omega_r$	PMSG angular speed	rad/s
$k_s$	Drive-train stiffness	Nm/rad
$\gamma$	Drive-train torsional displacement	rad
$p$	Number of PMSG pole pairs	unitless
$L_d$	Stator d-axis inductance	H
$L_q$	Stator q-axis inductance	H
$R_s$	Stator winding resistor	$\Omega$
$\theta_r$	PMSG rotor angle	rad
$v_{sd}$	Stator d-axis voltage	V
$v_{sq}$	Stator q-axis voltage	V
$i_{sd}$	Stator d-axis current	A
$i_{sq}$	Stator q-axis current	A
$\lambda_m$	PMSG maximum flux	Wb
$T_e$	PMSG electrical torque	Nm
$P_e$	PMSG electrical power	W
$m_d$	d-axis modulating signal	unitless
$m_q$	q-axis modulating signal	unitless
$P_W$	WECS output real power	W
$Q_W$	WECS output reactive power	Var
$v_{dc}$	dc-link voltage	V



$C$	dc-link capacitance	F
$L$	Inductance of the tie reactor	H
$\omega$	Power system angular frequency	rad/s
$f$	Power system frequency	Hz
$p_G$	Number of pole pairs of a CPP	unitless
$J_G$	Moment of inertia of a CPP	kgm <sup>2</sup>
$P_{mov}$	Prime mover power of a CPP	W
$P_G$	Output electrical power of a CPP	W
$P_L$	Load real power	W

# Chapter 1

## Introduction

This thesis focuses on the real power control and frequency regulation with direct-drive wind energy conversion systems (WECSs) that employ high-pole permanent-magnet synchronous generators (PMSGs). Section 1.1 presents an introduction to WECSs and their integration into the power system. The remaining sections of this chapter outline the statement of problem, thesis objectives, background, thesis contributions, and the related literature review.

### 1.1 Introduction to Wind Energy Conversion Systems

Wind power has been a fast-growing alternative power source in the world. It is renewable and widely distributed. It also reduces toxic gas emissions. In 2012, global wind energy capacity grew by 19 percent, with the wind industry installing a record level of 44,711 MW of new clean wind power, and over 150,000 wind turbines operating around the world in over 90 countries [1]. In 2013, the global capacity growth rate has been above 14 percent [2].

Windmills have been utilized for irrigation pumping and milling grain since the 7th century AD [3]. The traditional windmills had typically four blades that provided a lattice framework over which the canvas sails could spread. In light winds, the whole blade area would be covered. In strong winds, the power output could be limited by only covering part of the blades. With a diameter typically of about 25 m, the traditional windmill could deliver a shaft power output of about 30 kW in a wind speed of about 7 m/s [4]. In a well exposed location, it would give an average power output of about 10 kW.

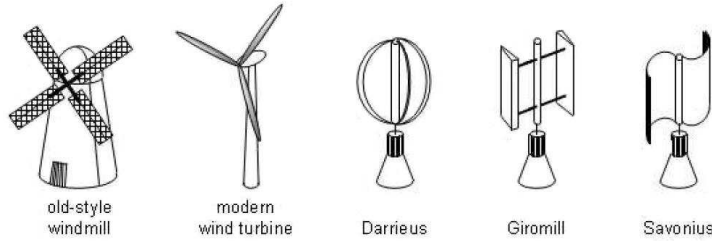


Figure 1.1: Examples of wind turbine concepts [8].

However, steam engines became progressively more efficient and more economic as the 19th century advanced. Because steam engines could also provide power on demand, the use of windmills went into decline. This decline was accelerated by the later development of internal combustion engines and by the trend in fossil fuels which became more readily available and less costly. Since 1973, the trend of decreasing fuel prices has been sharply reversed, and it is now accepted that the era of very cheap fuel has ended. This trend in addition to the global efforts in reducing greenhouse gas emissions mainly caused by fossil fuels has resulted in investing increasingly in renewable energy sources. Among the various types of renewable energy, wind energy is now emerged as one of the most promising of the renewable energy technologies. It is predicted that by 2020 up to 12% of the worlds electricity will be supplied from wind energy [5].

### 1.1.1 Wind Turbine Concepts

Wind turbines are mechanical devices specifically designed to convert part of the kinetic energy of wind into useful mechanical energy. Since the beginning of wind turbine development, various concepts and designs have been developed. In the following, a general overview of wind turbine concepts is presented.

#### Aerodynamic Drag and Lift

Wind turbines can be divided into those that depend on aerodynamic drag force and those that depend on aerodynamic lift force. In a design based on the drag force, wind pushes the blade out of the way and the turbine angular speed is typically slower. Because of their high torque capabilities, drag-driven turbines are suitable for pumping, sawing, or grinding [6]. The typical example of such design is the old-style Dutch windmill [Figure 1.1]. In a design based on the lift force, the blades cross section has an airfoil shape such that when the wind passes by a blade the pressure on the lower surface is higher

and, hence, lifts the blade. The same principle allows airplanes to fly. The turbines that achieve their driving power from the lift force have higher angular speeds as compared to the ones based on the drag force, and are well suited for electricity generation. In general, lift-driven turbines are more efficient than their drag-driven counterparts [7].

### **Vertical-Axis and Horizontal-Axis Wind Turbines**

Wind turbines can be further divided into vertical-axis and horizontal-axis turbines based on the orientation of their spin axis. In a vertical-axis turbine, the blades rotate about an axis perpendicular to the ground. The most common designs are the Darrieus (curved blades), Giromill (straight blades), and Savonius (scoop blades) [Figure 1.1]. Vertical-axis turbines have the advantage of operating independently of the direction of wind. Moreover, the gearbox and generating machinery can be placed at the ground level. However, their major disadvantages are high torque fluctuations with each revolution, no self-starting capability, and limited options for speed regulation in high wind speeds [6].

In a horizontal-axis turbine, the blades rotate about an axis parallel to the ground and wind flow. Common examples are the old-style Dutch windmill and modern wind turbines [Figure 1.1]. A horizontal-axis turbine consists of a tower and a nacelle that is mounted on top of the tower. The nacelle contains the generator, the gearbox and the rotor. Nowadays, nearly all modern commercial wind turbines connected to grid are horizontal-axis turbines. One reason is that they are more suitable for harnessing the higher and smoother wind at higher altitudes. Different mechanisms exist to point the nacelle towards the wind direction or to move the nacelle out of the wind in case of high wind speeds. In the small turbines, the rotor and the nacelle are oriented into the wind with a tail vane. In the large turbines, the nacelle with the rotor is electronically yawed into or out of the wind in response to a signal from a wind vane.

### **Number of Blades**

Horizontal-axis wind turbines can have different number of blades, depending on the purpose of the turbine. Two-bladed or three-bladed turbines are usually used for electric power generation due to their higher angular speeds. Turbines with 20 or more blades are used for mechanical water pumping due to their higher mechanical torque. To extract the maximum possible wind power, each blade should interact as much as possible with the wind passing through the swept area. Therefore, a fewer number of blades results in a higher angular speed of the turbine, because the blades have to move faster to fill up the

swept area. A wind turbine with a high number of blades has a low angular speed but a high mechanical torque. In contrast, a wind turbine with only two or three blades has a higher angular speed which allow the use of a smaller and lighter gearbox to achieve the required high speed at the driving shaft of the power generator. Currently, three-bladed turbines dominate the market for grid-connected horizontal-axis wind turbines.

### **Betz Limit**

An important operational characteristic of wind turbines is the Betz limit. It indicates the theoretical maximum possible energy that the turbine can extract from the wind. If turbines were 100% efficient, which is practically impossible, all the airflow energy would be extracted and the flow speed after passing through the turbine would be zero. In 1928, Betz showed that under ideal assumption of uniform rotor disk with infinite number of blades the maximum efficiency of a turbine is 59.3% [3]. In practice, this coefficient is less due to non-ideal conditions such as wind shade behind the rotor, finite number of blades, blade-tip losses, and frictional drag. Present wind turbines have an efficiency around 52%-55% [6].

### **Upwind and Downwind Turbines**

In the upwind configuration, the turbine faces into the wind with the blades in front of the nacelle, whereas a downwind turbine has its blades to the rear of the nacelle and faces away from the wind. An upwind turbine produces a higher power than that in the downwind configuration, because it eliminates the tower shadow on the blades. This results in lower noise, lower blade fatigue, and smoother power output. However, a drawback is that the turbine must constantly be turned into the direction of wind by the yaw mechanism. The heavier yaw mechanism of an upwind turbine requires a heavy-duty and stiffer rotor compared to a downwind configuration. In contrast, the downwind turbine has the wind shade of the tower in the front and loses some power from the slight wind drop. However, it allows the use of a free yaw system. It also allows the blades to deflect away from the tower when loaded. Its drawback is that the turbine may yaw in the same direction for a long period of time, which can twist the cables that carry current from the nacelle. Both types have been used in the past. Although, the upwind turbine configuration has become more common [9].

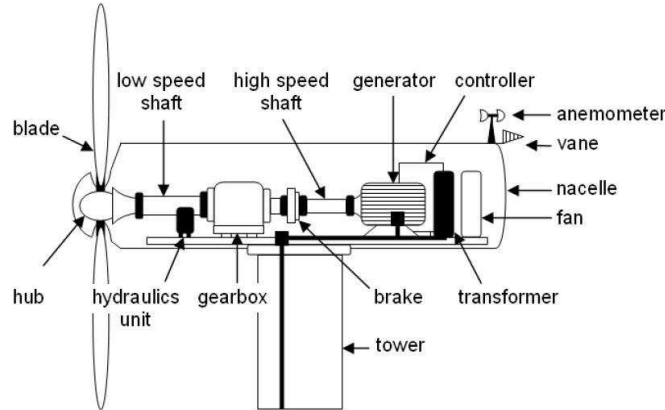


Figure 1.2: Main components of a wind energy conversion system.

### 1.1.2 Components of Wind Energy Conversion Systems

The main components of a WECS is shown in Figure 1.2. The turbine consists of the blades, the hub, and the connecting components including bearings and pitching actuators. The turbine transforms the kinetic energy of wind into mechanical energy. In multi-megawatt turbines, the blades can be over 60 meters in length [6].

The drive train is formed by the turbine rotating mass, low-speed shaft, gearbox, high-speed shaft, and generator rotating mass. It transfers the turbine mechanical energy to the generator shaft where it can be converted to electrical energy. A gearbox is required between the turbine and the generator, because the angular speed of the turbine is much lower than that of the generator. However, a gearless configuration can also be developed by increasing the number of generator pole pairs. For multi-megawatt turbines the gearbox ratio is about 50-100, because the typical speed range of the turbine is 10-20 rpm, whereas for the generator it is about 1000-2000 rpm [3]. For smaller WECSs, the turbine speed is higher and, therefore, the gearbox ratio may be less than 50. The low-speed shaft contains pipes for the hydraulics system that operate the aerodynamic brake. The high-speed shaft is equipped with an emergency mechanical brake that is used in case of failure of the aerodynamic brake. Other components include the anemometer and vane which respectively measure the speed and direction of wind. Devices such as electric fans and oil coolers are used to cool the gearbox and generator.

### 1.1.3 Aerodynamic Torque Control

The tower yaw angle and blade pitch angle can be actively controlled to regulate the aerodynamic torque. The yaw angle is usually controlled to make sure that the turbine

is facing the wind to extract the maximum possible energy. This is performed by rotating the nacelle about the tower axis. Reduction of input aerodynamic torque is usually obtained by the blades. In stall-controlled turbines, the blade cross section is designed such that above a certain angular speed the blades enter a stalling mode. The counterpart of stall-controlled turbines are pitch-controlled turbines. In this configuration, the aerodynamic torque is regulated by pitching the blades to feather, i.e., by reducing the angle of attack. Pitch-regulated turbines can be active or passive pitch controlled. In the former case, a controllable pitching mechanism (usually a hydraulics system) is in place. In the latter case, the blades are mounted on the hub such that the thrust force pitches the blades, i.e. the blades are self-pitched [7].

The advantage of stall regulation is that a complex control for blade pitching is not required. The aerodynamic and structural design of the turbine are, however, more complex. Nowadays the trend is to use pitch-controlled turbines due to their enhanced performance and less mechanical loads. The pitch angle in large modern turbines cannot change immediately but only at a finite rate, which might be low due to the size of turbine blades. The rate of change of the blade pitch angle is in the range of 3-10 degrees per second, depending on the size of the wind turbine [6].

#### 1.1.4 Types of Wind Energy Conversion Systems

There are mainly four types of WECSs [Figure 1.3] which has been used commercially at the utility level and are introduced in the following [10]:

- **Type A: Fixed-Speed WECS**

This configuration consists of an asynchronous squirrel cage induction generator which is directly connected to the grid via its stator terminals and, therefore, the angular speed of the generator is fixed at the grid angular frequency. However, the slip of the generator allows very small speed variations and softens its torque-speed characteristic. Because the squirrel cage induction generator always draws reactive power during operation, this configuration uses a capacitor bank at the generator terminals for power factor correction. This type is usually used in combination with stall regulation, although turbines with pitch angle control have also been built. This type uses the simplest WECS configuration which makes up the biggest share of the smaller WECSs already installed and scattered on the network. For small WECSs in a strong grid, this is arguably the most economical solution as the grid

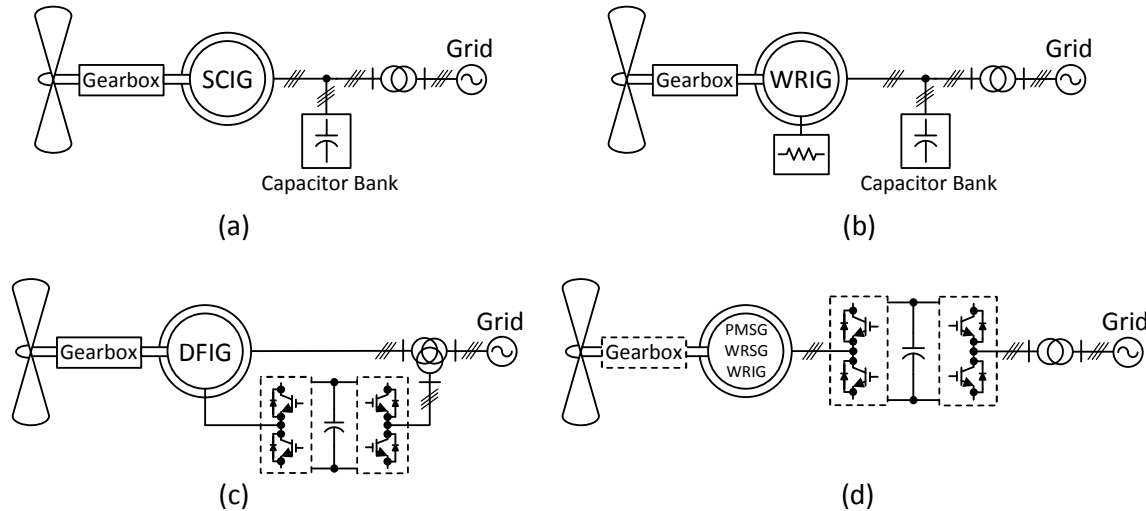


Figure 1.3: Commercial configurations of wind energy conversion systems; a) type A, b) type B, c) type C, and d) type D.

is able to provide reactive power and maintain a satisfactory voltage profile. The disadvantages of this type are the requirement for reactive power compensation and soft-starters and that the voltage quality is easily deteriorated in weak networks.

- **Type B: Variable-Speed WECS with Variable Rotor Resistance**

This configuration is in principle the same as the one in type A; however, a wound rotor induction generator with external rotor resistance is utilized in this configuration. This type allows variable-speed operation in a limited range of up to 10% above the grid angular frequency. A capacitor bank is also used in this type for power factor correction. The advantage of this type is its larger slip range compared to type A and a simpler control structure compared to the following two other types. It has, however, the same problems as type A. Moreover, compared to type A it has increased losses due to the larger rotor resistance.

- **Type C: Variable-Speed WECS with Doubly-Fed Induction Generator**

In this configuration, the pitch-controlled turbine is coupled via gearbox to a doubly-fed induction generator. The generator provides variable-speed operation by means of a partial-scale power-electronic ac-dc-ac converter in the rotor circuit. Depending on the converter size, this configuration allows a wider range of the variable-speed WECS operation of approximately  $\pm 30\%$  around the grid angular frequency. The advantages of this type are the speed variability (which reduces the mechanical stress), the possibility to optimize the power capture by regulating



the electrical torque, and the ability to control reactive power independently. The smaller power-electronic converter makes this type attractive from an economic point of view compared to a WECS with a full-scale converter, which is explained next.

- **Type D: Variable-Speed WECS with a Full-Scale Converter**

This configuration provides a pitch-controlled variable-speed operation over the entire speed range of the generator. Moreover, the full-scale converter ensures reactive power compensation and smooth grid connection. The generator can optionally be an asynchronous or synchronous generator. The generator can be excited electrically (wound rotor synchronous generator or wound rotor induction generator) or by a permanent magnet (permanent-magnet synchronous generator). Typically, a direct-drive high-pole synchronous generator is employed which eliminates the use of the gearbox due to the low-speed operation of the generator. Synchronous generators are suitable for higher power applications as they operate at unity power factor. The main advantage of this type is the complete decoupling of the generator from the grid which can facilitate the control of the WECS under disturbances from wind or the grid. The main disadvantage is the higher cost of the large converter.

Before 2001, types A and B were the dominant technologies of the grid-connected WECSs. However, type B is not offered any more and type A is being phased out of the market, in particular in the area of multi-megawatt WECSs [10]. The present trend in the industry is to use variable-speed WECSs due to their superior annual power production, which exceeds by 5 to 10 percent from those of fixed-speed WECSs [11]. This improvement in efficiency is, however, obtained at the cost of greater complexity in the construction of the unit and also some additional losses in the power-electronic converters (which enable the variable-speed operation). Moreover, the advances in semiconductors technology make utilizing power-electronic converters in WECSs economically justifiable. Thus, the most recent installed WECSs are dominated by types C and D.

### 1.1.5 Direct-Drive PMSG-Based WECSs

Traditionally, step-up gearboxes have been utilized in WECSs to provide high angular speeds for the generators. However, the gearbox brings weight and cost penalties, is subject to mechanical degradation and wear, demands regular maintenance, generates noise, and incurs loss [12]. Therefore, the idea of gearless, i.e., direct-drive, WECSs has gained

interest in the recent years, especially for offshore applications where a low maintenance solution is an attractive option. Moreover, the higher efficiency of a WECS with gearless drive-train results in achieving about 3 to 5 percent higher energy production compared to a similar WECS with gearbox [13]. To provide high torque at low angular speeds, the direct-drive configuration requires the generator to have a large number of poles and, thus, a large diameter. Permanent magnet excitation for synchronous generators allows for small pole pitch and can yield cost-effective designs [14]. Other advantages of a PMSG compared to an electrically-excited synchronous generator are: lighter weight, no additional power supply for the field excitation (which results in a higher reliability due to the lack of slip rings), improvement in the efficiency, higher energy yield, and higher power to weight ratio [15]. The disadvantages of a PMSG are that its excitation cannot be controlled and it is more expensive.

In this thesis, a direct-drive WECS is utilized which employs a high-pole PMSG. The choice is based on the expectation that this class of WECSs will be widely deployed in the future, due to its simple and low-loss generator, and gearless, maintenance free, light, and quiet drive-train (specially for offshore applications in which the maintenance is extremely expensive and complex) [16].

### 1.1.6 Operating Regime

The main turbine specifications are determined following from the choice of the turbine rotor diameter. The turbine tip speed is restricted to meet the acceptable noise level emitted from the turbine. From the maximum allowed tip speed and the desired power capacity, the rated angular speed of the turbine is determined. However, in offshore applications the noise emission (which is dominated by the rotor and increases with the square of the rotor speed) is not a design driver and the turbine could operate at higher rotor speeds that result in higher energy extraction capabilities (with the same rotor diameter) [17].

The operating regime of a wind turbine can be illustrated by its power curve, which plots its estimated output power as a function of wind speed. An example of a wind turbine power curve is shown in Figure 1.4. The power curve gives three important values [3]:

- Cut-in wind speed: minimum wind speed at which power generation is reasonable.
- Rated wind speed: wind speed at which the turbine generates its rated power

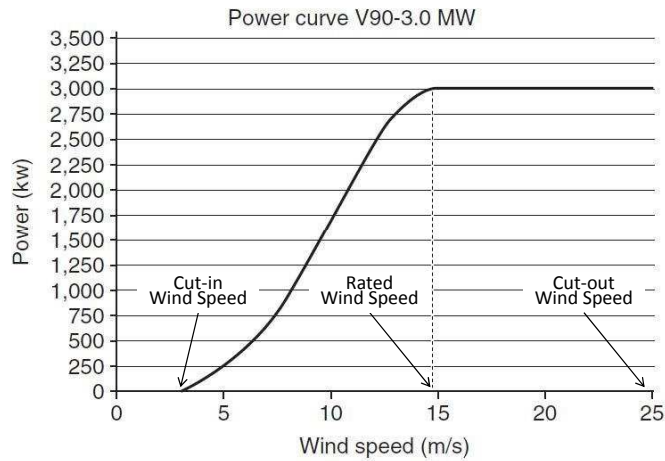


Figure 1.4: Power curve of Vestas V90 3 MW wind turbine [18].

(which is often but not always the maximum power).

- Cut-out wind speed: wind speed at which the turbine is shut down (with automatic brakes and/or blade pitching) to protect the turbine from mechanical damage.

Below rated wind speed, the WECS is operating in partial-load regime. Above rated wind speed, the WECS is operating in full-load regime. In each operating regime the WECS can be controlled in various ways to achieve specific objectives. The primary goals are to maximize the captured energy in the partial-load regime and to limit the captured energy to its rated value in the full-load regime. The pitch angle is usually maintained at its minimum in the partial-load regime to allow maximum energy extraction from wind and to limit the mechanical wear of the pitching mechanism. At a certain wind speed, the WECS controller must limit the output power by changing the pitch angle.

### 1.1.7 Grid Integration Requirements of WECSs

In the early days, small fixed-speed WECSs were scattered over the distribution network and the integration issues were mainly related to voltage and power quality problems such as [19]:

- Steady-state voltage change,
- Voltage flicker,
- Harmonics.

The shift towards the variable-speed WECSs has alleviated some of the above integration issues because variable-speed WECSs have smoother output power, use modern power electronics, and are able to control their power factor. However, new integration issues emerged because of the increasing size and geographic concentration of modern WECSs. The difficulties of wind power integration depend mainly on the grid strength. In a weak network, the penetration of wind power is limited, typically because the security and reliability of the grid cannot be maintained economically.

In the recent years, the grid codes established for most countries require the larger WECSs to behave similar to conventional power plants. The major requirements of typical grid codes for operation and grid connection of WECSs are summarized as follows [20]:

- Voltage operating range: WECSs are required to operate within typical grid voltage variations.
- Frequency operating range: WECSs are required to operate within typical grid frequency variations.
- Real-power control: WECSs are required to provide real-power control to improve the system stability and to prevent overloading of lines; WECSs are also required to respond with a ramp rate in the desired range.
- Frequency control: WECSs are required to provide frequency response capability to help maintain the desired network frequency.
- Reactive-power control: WECSs are required to provide dynamic reactive-power control capability to maintain the reactive power balance and the power factor in the desired range.
- Voltage control: individual WECSs are required to control their own terminal voltage to a constant value by means of an automatic voltage regulator.
- Low-voltage ride through: in the event of a voltage sag, WECSs are required to remain connected to the grid for a given time period before being allowed to disconnect; moreover, some utilities require that the WECSs help support grid voltage during faults by supplying reactive power.
- High-voltage ride through: in the event that the voltage goes beyond its upper limit, the WECSs should be able to stay connected for a given period of time.

- Power and voltage qualities: WECSs are required to provide the electric power with desired power and voltage qualities, e.g., maintaining voltage fluctuations and current harmonics in the desired range.
- WECS modeling and verification: some grid codes require wind farms owners to provide models and system data, to enable the system operator to investigate the interaction between a wind farm and the power system, by running simulations; they also require installation of monitoring equipment to verify the actual behavior of a wind farm during faults and to check the model.
- Communications and external control: wind farms operators are required to provide signals corresponding to a number of parameters which are important for the system operator, to enable proper operation of the power system; moreover, it must be possible to connect and disconnect the wind farm remotely.

The aim of these grid codes is to ensure that the continued growth of wind power does not compromise the power and voltage qualities of the electric power system, nor its security and reliability. Grid code requirements and regulations vary considerably from region to region. The differences in the requirements are due to the different wind power penetration levels and different degrees of power network robustness.

In this thesis, the technologies and solutions for operation and grid integration of direct-drive PMSG-based WECSs are studied to meet the grid codes related to output real-power control and frequency regulation requirements.

## 1.2 Statement of Problem and Thesis Objectives

Among the various types of renewable energy sources, wind power has now emerged as one of the most promising of the renewable energy technologies. Nowadays, there is a tendency to increase the size and capacity of WECSs. Wind power, similar to most of the renewable energy sources, is naturally fluctuating. Consequently, it possesses a different role in the power system compared to the conventional power plants (CPPs), such as thermal power plants. If only single and small WECSs are installed in the power system, wind power does not significantly influence the operation of the power system and can easily be integrated. In contrast, as the integration of wind power into the power system increases and WECSs continue to complement the CPPs, the impact of wind power on the power system becomes noticeable and must be taken into consideration.

Operators of the power systems with high wind power penetration encounter new challenges to maintain the reliability and stability of the grid. Therefore, new grid connection requirements have been established for WECSs. Modern WECSs are requested to act as active components in the grid and to take over control tasks, which are traditionally performed by CPPs. System operators should be able to control the output power of modern WECSs, to more effectively take part in the control of the power system, such as the frequency regulation. WECSs with controllable output power capability can help to improve the power quality in the power system, and have potential applications in the situation of large wind power penetration. These requirements introduce new challenges to the control of WECSs. Extensive research and development efforts have been carried out to introduce new technologies and control strategies for modern WECSs to resolve the technical issues associated with the ever-increasing wind power incorporation. Moreover, direct-drive variable-speed WECSs that employ high-pole PMSGs are expected to be widely deployed in the future, due to their low-loss generators, low maintenance requirements, and quiet drive-trains, which calls for studying their capabilities in meeting the new requirements.

The objectives of the thesis are:

- To develop a mathematical model for a direct-drive PMSG-based WECS and to introduce a strategy to control its output real power, which augments the maximum power-point tracking (MPPT) feature of modern WECSs.
- To enhance the aforementioned power control strategy by supplementing a damping mechanism, which enables rapid control of the WECS output power while the drive-train torsional modes are well damped, and to tune the parameters of the control scheme based on the eigenvalue analysis of the WECS.
- To introduce an alternative control strategy for the direct-drive PMSG-based WECS which mitigates the sensitivity of the WECS output power to power fluctuations caused by wind speed variations and drive-train oscillatory modes, while enables the WECS to damp its drive-train oscillations and maintain internal stability, even if its output real power is regulated, and to ensure a stable performance of the WECS over the operating range.
- To develop an enhanced control mechanism that enables a WECS to contribute to frequency regulation process by effectively using its available generation reserve and

the kinetic energy of its rotor, such that the stability of the WECS is maintained, under different wind speed regimes.

- To introduce a procedure to ensure a reliable operation of a power system with large integration of wind power by taking into account the intermittency of wind and its impact on the power system frequency regulation.

## 1.3 Background

### 1.3.1 Real Power Control in WECSs

The pervasive penetration of wind power into the electric grid indicates that WECSs should also be able to take part in the power-flow control process which, presently, is exclusively undertaken by the CPPs; the feature should retain the MPPT capability that modern WECSs currently possess. WECSs with controllable output power can help to improve the power quality in the grid and have potential applications in the situation of large wind power penetration [21].

#### Power Generation Control and Curtailment of WECSs

Renewable energy sources like wind power have priority access to the grid due to their marginal price of almost zero, i.e., other generation sources must restrict their production [22]. However, curtailment of the wind power production may be required at certain conditions and can reduce the overall system integration costs. Curtailment of wind power could mainly arise because of network limitations or system aspects [23].

Examples of wind power curtailment because of network limitations are:

- Local limitations could give rise to a need to constrain the output of a group of WECSs. The connection of WECSs is normally planned so that constraints are not required under the conditions covered by the planning criteria. However, conditions not covered by the criteria may arise from time to time.
- The time frame from application to connection of a wind farm can be down to a year, whereas the time frame from planning to commissioning of new transmission lines might be a decade.

Examples of wind power curtailment because of system aspects are:

- At times of low power demand in the power system, a minimum level of CPPs must be kept connected to ensure the stability and reliability of the power system. Therefore, the surplus wind power production may be curtailed.
- Due to the risk of reduction in the available wind power production at the same time as the power demand rises, wind power may have to be constrained to ensure that the load gradient that must be met by the remaining power plants is within their dynamic capacities.
- In case the wind power production exceeds power demand plus interconnection capacity or cannot be accommodated by the transmission or distribution system, the generation surplus must be removed.
- Modern WECSs are capable of going from partial load to full power within a very short time, given the necessary wind conditions. This makes wind power a valuable asset for fast regulation.

### **Torsional Dynamics of Modern WECSs**

The torsional dynamics of the modern WECSs differ from the conventional turbine generators. WECSs are the only generation units in the utility network where the mechanical stiffness is lower than the electrical stiffness [24]. The electrical stiffness represents the torsional dynamics of a generation unit drive-train as a whole, against the synchronous power system, whereas the mechanical stiffness represents the interactions among the different components of the drive-train in the generation unit. The lower mechanical stiffness of modern WECSs is due to the large diameter of their turbines that is required to capture more energy from the wind.

One of the first experiments that indicated the soft coupling between the turbine and the generator in fixed-speed WECSs was the islanding experiment carried out at the Rejsby Hede wind farm [25]. During the experiment, the wind farm was disconnected from the transmission network. This islanded operation continued for less than one second before the WECSs were tripped and the turbines were stopped. During the islanded operation, the electrical frequency showed an oscillatory behavior [Figure 1.5]. The natural frequency of these oscillations was 1.7 Hz which corresponded to the drive-train torsional modes of the WECSs [26].

As the modern WECSs are built with larger turbine diameters to extract more energy from the wind, the flexibility associated with their rotor structure increases which may



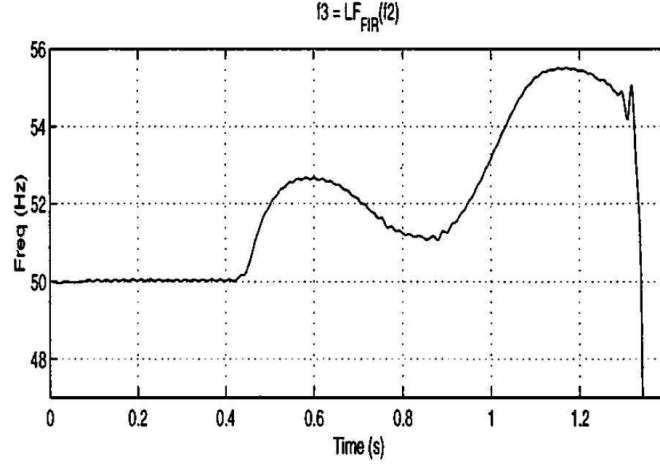


Figure 1.5: The electrical frequency at the wind farm [25]; at  $t = 0.4$  s the wind farm was disconnected from the transmission network.

affect the dynamic performance of the WECS [27]. A larger diameter of the turbine results in drive-train torsional modes with lower frequencies, which may lead to instability of the WECS or its interaction with the low-frequency modes of the electrical power system. Therefore, it is important to take the torsional modes of the drive-train in modern WECSs into consideration. In fixed-speed induction generator based WECSs, the induction generator acts as an effective damper, which helps to reduce the magnitude of the drive-train oscillations. However, it has been reported that these oscillations are still significant and must be taken into account when analyzing the dynamic performance of fixed-speed WECSs in transient stability studies [28]. In case of the variable-speed WECSs which operate at a controlled torque, the damping contribution of the generator is low because the torque no longer varies as a function of the rotor speed. Therefore, damping techniques are required to be incorporated in the control system of variable-speed WECSs.

Reference [29] reports that the equivalent stiffness of a WECS drive-train is inversely proportional to the square of the number of the generator pole pairs and, therefore, is low in a WECS with a high-pole PMSG. In other words, a larger number of generator pole pairs results in a softer driven-train, according to

$$k_{eq} = \frac{\kappa}{p^2}, \quad (1.1)$$

where  $k_{eq}$  is the equivalent shaft stiffness (in Nm/rad), and  $\kappa$  is the shaft stiffness (in

Nm/rad) calculated as [30]

$$\kappa = \frac{G\pi D_{sh}^4}{32L}, \quad (1.2)$$

where  $D_{sh}$  is the shaft diameter,  $L$  is the shaft length and  $G$  is the shear modulus.

Equation (1.1) implies that any twist of the mechanical shaft results in a larger dynamic change of the electrical rotor angle for generators with a larger number of pole pairs. However, in a direct-drive WECS, the shorter length of the mechanical shaft between the turbine and the generator due to the elimination of the gearbox increases the stiffness to some extent. In conclusion, the drive-train torsional modes in a direct-drive WECS that utilizes a high-pole PMSG may significantly affect the operation of the whole WECS. Due to the torsional characteristic of the drive-train, the rotor speed is prone to oscillation whenever the system gets excited by mechanical or electrical load changes [31]. The torsional modes may lead to fluctuations in the dynamic performance of the WECS and may increase the mechanical fatigue of the drive-train. These oscillations are typically in the range of 0.1 Hz-10 Hz [32]. Consequently, a single-mass or lumped model of the drive-train is insufficient to analyze the transient behavior of a WECS, as reported in reference [33], and may result in significant errors. Therefore, a multi-mass model should be considered for the drive-train of modern WECSs.

The variable-speed generator in a direct-drive PMSG-based WECS is connected to the grid via a full-scale converter. Therefore, the generator is decoupled from the electric grid and, thus, the strong torsional damping characteristics which are inherent to ac-connected generators are lost [34]. Moreover, the frequency at the terminals of the PMSG in such a configuration is changing freely with the rotor speed. Hence, even in case of transient load changes there is no relative movement between the rotor field and the stator field that could induce a current into the damper windings. As a result, no damping torque is provided to counteract the rotor speed oscillations. Figure 1.6 shows how the rotor speed of a WECS oscillates with gradually increasing oscillation amplitude, causing the WECS to break down eventually.

The absence of any damping mechanism might lead to self-excitation and even instability of the WECS. Moreover, as the tendency to build larger WECSs at competitive costs encourages lighter and, consequently, more flexible drive-trains, the aspect of developing control strategies with damping capabilities as an explicit objective of a modern WECS control algorithm becomes increasingly important [35].

The mechanical torque of a wind turbine can only be varied by pitching the blades.

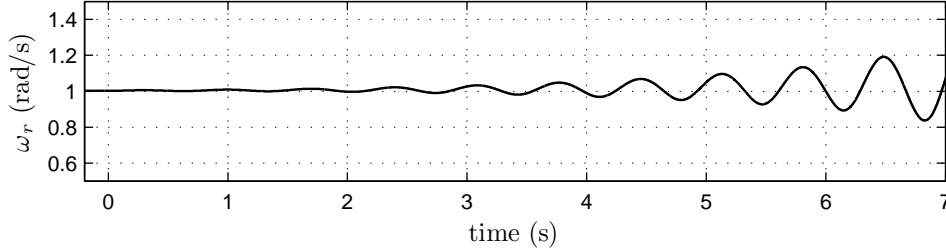


Figure 1.6: Undamped oscillations of the rotor speed in a WECS without a damping mechanism.

However, damping by means of blade pitching, as suggested in reference [36], is a very inefficient way of influencing the drive-train torsional modes. It may also be possible to provide some damping using extra hardware mounted on the drive-train [37], which is costly and needs extra devices. Another solution is to modify the control scheme of a WECS in order to provide sufficient damping [34]. The main idea is to suppress the rotor speed oscillations by supplementing the control system with a damping scheme.

### Multi-Mass Modeling of a WECS Drive-Train

The two-mass model of the power producing WECSs was first suggested in [24] to study the drive-train torsional modes of grid-connected WECSs. Reference [28] discusses that a two-mass representation of the drive-train is necessary for the stability analysis of a WECS to accurately capture the effects of the electromechanical interactions. Higher-order representations of the drive-train dynamics have also been considered in the literature. However, because a high-order drive-train model may not be suitable for investigating the transient stability of the WECSs in large power system studies, different representations of the drive-train dynamics are studied in literature to evaluate how they affect the performance of the WECSs during electrical transients and to assess the accuracy of representing the drive-train dynamics with a reduced-order two-mass model in transient stability studies.

As wind is intermittent and stochastic in nature, the mechanical torques acting on the three blades of a wind turbine are not always equal. Reference [38] reports that this unequal blade torque sharing can only be analyzed with a six-mass model of the drive-train, in which the six masses include the three individual blades, the hub, the gearbox, and the generator. Although, in the study performed by reference [39], it is ensured that the unequal torque distribution on the blades has no effect on the transient stability of a WECS. Therefore, it can be assumed that a three-blade turbine has a uniform weight

distribution, for simplicity. Hence, the weight of the three blades is combined to make a single mass and the turbine torque is considered to be equal to the aggregate of the torques acting on the three blades. Detailed transformation from the six-mass model to a three-mass model is presented in reference [39]. The model is further reduced to a two-mass drive-train model. In the two-mass model, one mass represents the turbine inertia which can be calculated from the combined weights of the three blades and the hub, and the second mass represents the inertia of the gearbox and the generator. The gearbox divides the drive-train into low-speed and high-speed shafts. The stiffness of the low-speed shaft is considered as the drive-train stiffness in the reduced-order two-mass model. The behavior of the WECS in response to an electrical disturbance is compared when using a six-mass, a three-mass and a reduced-order two-mass model of the drive-train. The study concludes that a reduced-order two-mass model of the drive-train is sufficient, with reasonable accuracy, for the transient stability analysis of a WECS.

Reference [27] introduces a three-mass model for a WECS drive-train which takes into account both torsional flexibilities of the shaft and bending flexibilities of the blades. The parameters of the three-mass model are derived by matching the mathematical equations of the three-mass model with the frequency spectrum result (which is achieved by running an experimental test on the WECS). Based on the derived three-mass model, it is concluded that the effective flexibility of the blades is 0.4 times larger than the flexibility of the shaft, i.e., the blade flexibility is more important than that of the shaft. However, representation of both shaft and blade flexibilities increases the order of the model, which may not be desirable for stability studies of WECSs in a large power system. Moreover, for the dynamic studies of a WECS, the torsional mode that has less damping and is likely to be the most significant is the one with the lowest frequency. Therefore, instead of neglecting the effect of the blade or shaft flexibilities, an effective two-mass model is obtained in [27], which takes into account both shaft and blade flexibilities but only represents the dominant low-frequency torsional mode of the drive-train.

In conclusion, regardless of various approaches in calculating the parameters of the drive-train model, there is a major consensus that a two-mass model is adequate for capturing the dynamics that affect stability; higher-order models are commonly employed for studying the mechanical fatigue of the turbine drive-train.

A two-mass representation of the drive-train have an unstable oscillatory mode with

the frequency described as

$$f_{osc} = \frac{1}{2\pi} \sqrt{\frac{k_s}{J_{eq}}}, \quad (1.3)$$

where  $J_{eq}$  is the equivalent drive-train moment of inertia which is determined by

$$J_{eq} = \frac{J_t J_r}{J_t + J_r}, \quad (1.4)$$

parameters  $J_t$  and  $J_r$  respectively signify the turbine and generator moments of inertia (in  $\text{kgm}^2$ ). The torsional mode of (1.3) could be excited by a rapid torque change on either end of the drive-train system.

In the mechanical system of a WECS, the damping factors include [40]:

1. The mass damping factor, which is the damping element of the individual masses. This damping factor is mostly attributed to the friction of bearings. The bearing system in a WECS mechanical drive-train is usually oiled. Therefore, the friction is small and, consequently, this damping is neglected in this thesis.
2. The shaft damping factor, which is the mutual damping between adjacent masses. This damping factor is attributed to the shaft material and is negligible and, thus, the damping effect due to this factor is also not taken into consideration in this thesis.

### 1.3.2 Frequency Regulation in Power Systems

Frequency regulation plays an essential role to operate a power system in a secure and stable manner. The present trend of increasing wind power integration may reduce the power system frequency regulation capabilities and create difficulties with frequency control [41]. Conventional power plants supply the major portion of the real power consumed in the grid and are responsible for maintaining the overall system frequency within the acceptable range. Lowering the share of the CPPs in a power system by replacing them with WECSs, which lack an inherent frequency response, means a decline in the number of synchronous generators connected to the grid and, thus, results in a reduction in the system rotating mass. This significantly impacts the overall frequency regulation capabilities and reduces the system robustness to disturbances. This problem is particularly important in weak power systems and requires further attention regarding

the potential of WECSs to participate in frequency regulation process. Modern WECSs should not degrade the stability of the existing power system, but should, if possible, contribute to increase the stability by actively providing frequency response upon request. Consequently, the output real power of the WECSs should be controllable such that a wind generation reserve could be maintained for frequency response.

The power balance issue in a power system is discussed next. Then, the mechanism of frequency control in power systems with and without wind power penetration is presented.

### **Power Balance Issue**

The function of an electrical power system is to produce electricity from its available sources and transport it to the points of consumption. Electricity has the advantage of being transported and controlled with relative ease and a high degree of efficiency and reliability. A properly designed power system should at least meet some fundamental requirements. One of these fundamental requirements is the ability to control frequency. The variations in power system frequency indicates the mismatch between the supply from the generating power plants and the consumers power demand. If demand equals supply, then the frequency remains constant.

Conventionally, the frequency of a power system is maintained within a narrow range because [42]

- It ensures that electric motors operate at virtually constant speed. Many consumer applications require a fixed speed at which an ac electric motor is operated to drive a device.
- Transformers are sensitive to frequency variations and may be overloaded if the frequency drifts substantially from its rated value.
- In electronic applications the rated frequency can be used as a basis for the timing of various processes.
- Most importantly, in conventional power stations the performance of the generators is dependent on the performance of all the auxiliary electric motor drives that deliver fuel and air to the boiler, oil to bearings, and cooling services to several systems. If these auxiliaries fail to function properly due to a low speed caused by a low frequency, power station output could be reduced. This phenomenon

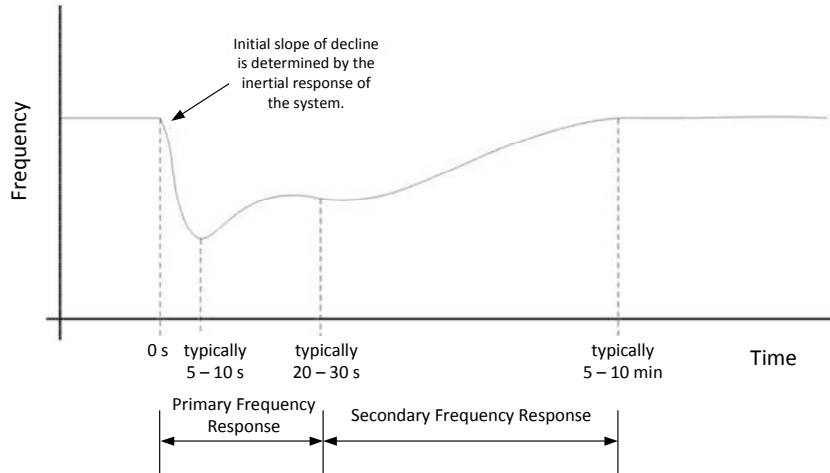


Figure 1.7: A typical frequency response following a sudden loss of generation.

may lead to a runaway situation with cascaded shutdown of power stations and blackouts.

### Frequency Regulation with CPPs

Because the power demand is constantly varying in a power system, CPPs regularly adjust the mechanical power that is supplied to their synchronous generators through the governor action, to closely track the power demand [43]. However, this process does not happen instantaneously due to the system inertia, i.e., system rotating mass. The system rotating mass absorbs or releases kinetic energy to compensate for the difference between the power being consumed in the system and that being supplied by the prime movers of the CPPs. When there is a significant disturbance in the power system, such as a sudden loss of generation, the power system provides frequency response to maintain the stability of the system by releasing the inertia of its rotating mass and using its generation reserve through the governor actions of its generating power plants. The frequency response of a power system is categorized into inertial, primary and secondary frequency responses. Figure 1.7 shows a typical frequency response in a large power system following a sudden loss of generation, and the time that each response takes [44].

**Inertial Frequency Response:** All of the synchronous generators that are connected to a power system spin with the same angular speed equal to the power system angular frequency. The angular speeds of all the generators vary as the power demand changes, such that the power balance is constantly met. If a power system has a high

inertia (and, thus, a high amount of kinetic energy stored in its rotating mass), then only a minor adjustment in the angular frequency of the grid is necessary to compensate for a change in power demand. However, in a power system with a lower inertia, a higher frequency variation occurs for the same power demand alteration. The inertia of a power system is, therefore, an important factor and acts as an initial arrestor to a falling (or rising) system frequency. It determines the sensitivity of the power system frequency and impacts the shape of the frequency response following an imbalance of supply and demand.

Right after a significant supply-demand imbalance in a power system, the principle of power balance requires that

$$\frac{dKE}{dt} = P_{G-sys} - P_{L-sys}, \quad (1.5)$$

where  $P_{G-sys}$  and  $P_{L-sys}$  respectively signify the overall power generation and demand (in MW), and  $KE$  is the overall stored kinetic energy in the power system and is described as

$$KE = \sum_{i=1}^n \frac{1}{2} \frac{J_{G-i}}{p_{G-i}^2} \omega^2, \quad (1.6)$$

in which  $\omega$  is the power system angular frequency (in rad/s),  $n$  is the number of synchronous generators connected to the power system,  $p_{G-i}$  is the number of pole pairs of the  $i$ th generator, and  $J_{G-i}$  is the moment of inertia of the  $i$ th turbine-generator (in  $\text{kgm}^2$ ) which is determined based on the physical constructions of the turbine and generator.

The kinetic energy stored in the rotor of each turbine-generator is often expressed in proportion to its rated power as

$$H_{G-i} = \frac{J_{G-i} \omega_0^2}{2 p_{G-i}^2 S_{G-i}}, \quad (1.7)$$

where  $H_{G-i}$  is defined as the inertia constant (in s),  $\omega_0$  is the rated angular frequency, and  $S_{G-i}$  is the rated apparent power of the  $i$ th power plant (in MVA). The inertia constant of a power plant indicates the duration of time that the power plant can provide its rated power in the output, by extracting from the stored kinetic energy in its rotating mass that was initially spinning at the rated angular frequency. This parameter falls typically in the range of 2-9 s for large power plants [45].



Substituting for  $KE$  from (1.6) to (1.5), one deduces

$$\sum_{i=1}^n \frac{1}{2} \frac{J_{G-i}}{p_{G-i}^2} \frac{d(\omega^2)}{dt} = P_{G-sys} - P_{L-sys}. \quad (1.8)$$

Expressing (1.8) in the per unit form, and multiplying  $S_{G-i}$  to the numerator and denominator of the left-hand side of the resulting equation yields

$$\sum_{i=1}^n \left( \frac{1}{2} \frac{J_{G-i}}{p_{G-i}^2} \frac{\omega_b^2}{S_{b-sys}} \frac{S_{G-i}}{S_{G-i}} \right) \frac{d\underline{\omega^2}}{dt} = \underline{P}_{G-sys} - \underline{P}_{L-sys}, \quad (1.9)$$

where  $\omega_b$  is the base value of the system angular frequency,  $S_{b-sys}$  is the base value of the system overall power, and the underline signs denote the variables in per unit.

Assuming  $\omega_b = \omega_0$ , from (1.7) and (1.9), one concludes

$$H_{sys} \frac{d\underline{\omega^2}}{dt} = \underline{P}_{G-sys} - \underline{P}_{L-sys}, \quad (1.10)$$

where  $H_{sys}$  is the inertia constant of the overall power system which is described as

$$H_{sys} = \sum_{i=1}^n \frac{H_{G-i} S_{G-i}}{S_{b-sys}}. \quad (1.11)$$

Equation (1.10) indicates that the rate of change of frequency (ROCOF) is mainly determined by the magnitude of the power imbalance and the system inertia constant. The system inertia constant depends on two factors including the number of operating generators and the inertia constant of each of these generators. A larger  $H_{sys}$  is more preferable as it signifies a higher amount of stored kinetic energy. The frequency of a power system with a large amount of stored kinetic energy tends to be less sensitive to power imbalances than the frequency of a system with a lower amount of stored energy. When a power system experiences a large disturbance, such as a sudden loss of generation, the system frequency begins to fall. As the frequency declines, the power system releases some of its stored kinetic energy. This is known as the inertial frequency response and is determined by the type of power plants in the system. For a synchronous generator, the angular speed is tightly coupled to the system frequency. Therefore, when the system frequency drops, the generator angular speed tracks the falling frequency and, thus, the stored kinetic energy of the power plant is released. This acts as an initial arresting mechanism to the falling system frequency. Nonetheless, it should be noted

that regardless of the inertial response of the power plants, the mechanical power of the prime movers must be increased in order to stabilize and return the frequency to its rated value.

**Primary and Secondary Frequency Responses:** Following the inertial frequency response of the power system, which reduces the ROCOF, the primary frequency response stabilizes the frequency at a new value by increasing (or decreasing) the power generation in proportion to the frequency variations. Then, the secondary frequency response, which is slower than the two aforementioned responses, regulates the frequency at its rated value. Primary and secondary responses are provided by power plants that are equipped with appropriate governing systems [43]. In a typical large power system, the power plants allocated to accomplish primary frequency response should be capable of increasing their output real-power within about 10 seconds of the pre-defined frequency variation and be capable of maintaining this response for a further 20 seconds. Secondary reserves require a slower initial response but are maintained for longer periods of time. This requires the capability of increasing the output real-power within about 30 seconds and maintaining the response for a further 30 minutes [42]. Beyond the primary and secondary reserves, power systems have standing reserves which are unsynchronized standby power plants and are not taken into consideration in this thesis.

A fundamental feature of the power plants that provide primary and secondary frequency responses, collectively known as the operating reserve, is their requirement to have generation reserves. Power plants providing such services are, therefore, partly loaded. In addition to hydro and pumped storage power plants (if available), the main providers of such services are flexible large coal fired power plants [42]. The amount of the required generation reserve is determined upon a statistical basis that takes into account the margin of error in demand prediction, the maximum deficit that may suddenly take place in a power system due to a loss of generation, and the probability of system failures.

### **Frequency Regulation with a High Penetration of Wind Power**

As the wind power penetration into a power system increases and WECSs continue to complement the CPPs, difficulties may arise in regards to regulating the power system frequency, if a large disturbance occurs in the system. Variable-speed WECSs based on doubly-fed induction generators or synchronous generators are generally equipped with power-electronic converters which decouple the angular speed of the turbine from the

Table 1.1: Typical Inertia Constants of Different Power Plants

Type of power plant	Inertia constant (H)
Thermal power plants	
(a) 3600 rpm (2-pole)	2.5 s to 6 s
(b) 1800 rpm (4-pole)	4 s to 10 s
Hydro power plants	2 s to 4 s
Modern WECSs	2 s to 5 s

angular frequency of the grid. Therefore, no inertial response is provided for frequency regulation, although there is a considerable amount of stored kinetic energy in the turbine blades and the rotor of a WECS [46]. Moreover, WECSs have been generally exempt from providing primary or secondary frequency responses [47]. Consequently, a large-scale integration of wind power will highly influence the frequency regulation process.

The reduction of the overall inertia in highly wind penetrated power systems impacts the ROCOF such that the remaining synchronous generators have less time to react to system disturbances. Moreover, a reduction in the number of generators that deliver primary response results in a lower minimum (or a higher maximum) frequency, when a significant disturbance takes place in the power system. Further decline in minimum frequency can initiate load shedding or may even cause a black-out. In weak power systems which already have a lower inertia with respect to large interconnected systems, the frequency response will be highly deteriorated when CPPs are replaced by WECSs. Hence, it is important to develop mechanisms that allow WECSs to more effectively contribute to frequency regulation process, to enable more integration of wind power into the grid [48],[49]. In addition, the amount of kinetic energy stored in WECSs should be evaluated to assess their available potential for inertial response contribution.

Table 1.1 lists the typical inertia constants of thermal and hydro power plants [43] and modern WECSs [50]. The table indicates that the inertia constants (and, thus, the stored kinetic energy) of modern WECSs are comparable to those of CPPs. The differences in inertia constants are due to the differences in mechanical construction, and also the lower angular speed of the rotor in WECSs compared to the those in CPPs [51],[52].

When comparing the stored kinetic energies in different power plants and their use in the frequency regulation process, it should be noted that

- The kinetic energy stored in a WECS varies with the turbine operating conditions. For instance, when the wind speed increases, the rotor angular speed also rises to

operate at maximum efficiency. A higher angular speed of the turbine results in a higher amount of stored kinetic energy. However, in a CPP the stored kinetic energy is virtually constant, because the generator angular speed is coupled with the grid angular frequency.

- The strong coupling between the generator angular speed and the grid angular frequency in a CPP has another consequence. When the frequency declines, the release of kinetic energy in a CPP is proportional to the ROCOF. However, the release of kinetic energy from a variable-speed WECS can be controlled independently from the ROCOF, due to the decoupling provided by the power-electronic converter.

The change in the kinetic energy of a power plant can be calculated as

$$\Delta KE = \frac{1}{2} J (\omega_2^2 - \omega_1^2) . \quad (1.12)$$

Expressing (1.12) in the per unit form, one finally deduces

$$\Delta KE = H S_b (\underline{\omega}_2^2 - \underline{\omega}_1^2) . \quad (1.13)$$

In a CPP, the generator angular speed is coupled to the grid and, thus, varies typically in the range of 0.95 pu to 1.0 pu. In contrast, in a WECS, the turbine angular speed is allowed to drop from 1.0 pu down to about 0.7 pu. Therefore, the following calculation can be performed to compare the potential kinetic energy release in a CPP with the one in a WECS which has the same power rating,  $S_b$ , and inertia constant,  $H$ , as the CPP.

$$\frac{\Delta KE_W}{\Delta KE_{CPP}} = \frac{1^2 - 0.7^2}{1^2 - 0.95^2} = 5.25 , \quad (1.14)$$

where  $\Delta KE_W$  and  $\Delta KE_{CPP}$  signify the variations in the kinetic energies of the WECS and the CPP, respectively.

Therefore, a WECS can extract 51% of its stored kinetic energy which is 5.25 times larger than the 9.75% kinetic energy release of a CPP. This makes the available kinetic energy in a WECS comparable to the one in a CPP and the technology also exists to harness it [53]. Moreover, due to the decoupling of the turbine angular speed from the grid, a WECS can provide a controllable kinetic energy release to improve the power system frequency response right after a significant disturbance in the system, in contrast

to the inertial frequency response of a CPP which is solely dependant on its physical rotating mass and the structure of its synchronous generator.

Currently, most of the WECSs are operating at their maximum available power to achieve the maximum economic benefit. This type of operation does not allow for a wind generation reserve required for primary frequency response. However, in a power system with high wind power penetration, maintaining a generation reserve in WECSs to contribute to the frequency regulation process can become more valuable to a power system than maximizing wind generation [54]. In addition, when wind power penetration is relatively high during the off-peak hours, CPPs may need to be forced offline due to the excessive wind power. This situation results in a lower generation reserve in the CPPs (and, thus, less effective frequency response of the power system) and calls for the contribution of WECSs to frequency regulation process. To realize a frequency response from a WECS the controllability of its output real power is a necessity.

### 1.3.3 Generation Reserves in Power Systems

Reliability of a power system is maintained by ensuring that the power generation meets the demand at all times. If the conditions of a power system could be easily predicted and were constant over all time frames, maintaining the reliability would be relatively straightforward. However, many of the properties of a power system, including its power generation, power demand, and transmission equipment availability, are both variable and unpredictable. Therefore, additional generation reserves, either online or on standby, should be made available in the power system. These generation reserves supplement the amount of power required to meet the actual demand and can be called upon to assist power system control if demand increases significantly or a generation capacity is suddenly lost.

#### Generation Reserve and Wind Power

Wind is an intermittent motive source which differs from the motive sources applied to the CPPs. The increased variability and uncertainty that wind power brings to the power system can impact the power system reliability and costs. One of the main operating impacts of integrating more wind power is the increased amount of generation reserve that the power system must hold to maintain the reliability of the system equal to a system without wind power [55]. An important factor in understanding the impact that wind power has on generation reserve requirements is the wind power diversity. For in-

stance, the output power of a WECS could vary on a minute-to-minute basis, due to the changes in the prevailing wind speed. However, because the minute-to-minute variability of individual WECSs in a wind farm are not correlated, the normalized aggregated output power of the constituting WECSs is much less variable in this time frame [56]. When looking at the overall power system, a large number of wind farms that are not geographically close to one another achieve even further decline in wind power variability.

Scheduling and distribution of the primary and secondary generation reserves among the power plants are, therefore, influenced by the amount of wind power penetration and whether the WECSs are contributing to the power system frequency response. Currently, some power system operators require WECSs to contribute, to some extent, to frequency regulation process. Electric Reliability Council of Texas (ERCOT) protocols guide its minimum frequency response and require the combined frequency response of all power plants in the ERCOT system to be at least 420 MW/0.1 Hz [57]. The protocols discuss the required primary frequency response from the WECSs with standard generation interconnection agreements signed after January 1, 2010. The wind power plants should have adjustable dead bands to match those of other conventional power plants and a similar droop to the other resources equal to 5%. Hydro Quebec has passed standards that apply specifically to wind power plants [58]. The requirement is for all the wind power plants larger than 10 MW to be equipped with a frequency regulation equipment to provide emulated inertial response. The requirement does not apply to the steady-state frequency regulation, i.e., primary response. The requirement demands a wind power plant to express an inertia constant similar to that of a conventional synchronous generator, equal to 3.5 s. The original requirement also stated that the wind power plants must give an increase of power equal to 5% above their current output, during a significant under-frequency, for a duration of 10 seconds [59].

### Capacity Factor

The capacity factor of a generation unit is usually defined as the ratio of its yearly energy output to the output it would have produced if it has been operating continuously at its nameplate rating. WECSs achieve capacity factors in the range of 20-40% depending on the windiness of the site (in comparison to the capacity factor of 40-90% for CPPs such as thermal plants) [60]. The capacity factor measures the productivity of a WECS and is a matter of an economical design. A turbine with a large rotor diameter combined with a small generator has a capacity factor of 60-80%, however produces very little

electricity. The most electricity is gained by using a large generator and, consequently, the capacity factor will be lower. WECSs are claimed to require back-up for 70% of the time. In fact, WECSs provide some power between cut-in and cut-out wind speeds for 80% of the time [42]. The capacity factor does not determine back-up requirements, which must be assessed statistically. On this basis, intermittent sources such as wind power are incapable of providing the same level of reliable or firm power as conventional generators during demand peaks, but they are still capable of providing a contribution to this.

## 1.4 Thesis Contributions

The main contributions of the thesis can be listed as follows:

- The thesis proposes a strategy for real power control of a direct-drive WECS that employs a high-pole PMSG, which augments the MPPT feature of modern WECSs. The proposed strategy is based on rapid torque control, rather than the (slow) pitch-angle control. Therefore, the pitch-angle control is not exercised for output real-power control, but it is employed, exclusively and, as per the common practice, for limiting the mechanical power if the turbine overspeeds. Moreover, a supplementary damping scheme is presented and tuned for the proposed power control strategy, based on a detailed mathematical model and eigenvalue analysis of the WECS. The proposed control strategy and its supplementary damping scheme enable the control of the WECS output real power, from a low value up to the maximum power corresponding to the prevailing wind speed.
- The thesis further presents an alternative control scheme for the direct-drive PMSG-based WECS whose advantage over the more common scheme is that it mitigates the sensitivity of the WECS output power to power fluctuations caused by wind speed variations and drive-train oscillatory modes. Moreover, capitalizing on the property of the conventional MPPT strategy employed by modern WECSs, which provides additional damping of drive-train torsional modes, the thesis proposes an enhanced control strategy that enables the WECS to damp oscillations and maintain internal stability, even if its output power is regulated. A procedure is presented for tuning of the proposed control, based on the mathematical model of the WECS, such that a stable performance of the WECS over the operating range is ensured.

- Finally, the thesis proposes an enhanced control strategy that enables a WECS to contribute to frequency regulation process by effectively using its available generation reserve and the kinetic energy of its rotor, such that the stability of the WECS is maintained, under different wind speed regimes. The proposed strategy allows for a smooth mode transition of the WECS to the MPPT mode of operation, at steady state, if the WECS reaches its maximum available power after its initial response to a significant frequency change in the power system. A procedure is also presented in the thesis to adjust the parameters of the proposed control for the WECS to ensure a reliable operation of a power system with large integration of wind power, by taking into account the intermittency of wind and its impact on the power system frequency regulation.

## 1.5 Thesis Outline and Related Literature Review

This thesis has been organized in five chapters as follows:

In the first chapter, an introduction to the thesis topic along with its importance to the area of Power Systems Engineering is presented. Research objectives and the contribution of the thesis are also outlined in Chapter 1. Chapters 2 and 3 of this thesis focus on the output real-power control of a direct-drive WECS that employs a high-pole PMSG. The real-power control strategies augment the MPPT feature of the WECS. A supplementary control scheme is presented for each control strategy, which enables the WECS to damp drive-train oscillatory modes over the operating range. The parameters of the damping schemes are tuned based on detailed mathematical models of the WECS.

Chapter 4 of this thesis concentrates on the contribution of WECSs to power system frequency regulation process. A control strategy is proposed for a WECS to provide inertial and primary frequency responses similar to the ones in a CPP, by effectively using its available generation reserve and the kinetic energy of its rotor. Moreover, the impact of wind speed intermittency on the frequency response of a power system with large wind power penetration is studied in Chapter 4, and the control parameters of WECSs are adjusted to ensure a reliable operation of the power system, under different wind speed regimes. Finally, the thesis is summarized and concluded in Chapter 5; chapter-wise summary of the thesis, the conclusions of the conducted research, and the future areas of research are also included in this chapter.



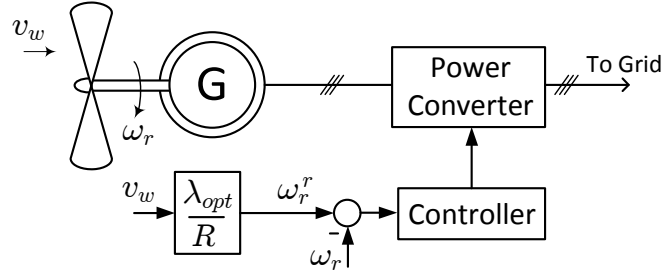


Figure 1.8: Tip-speed ratio control in a WECS.

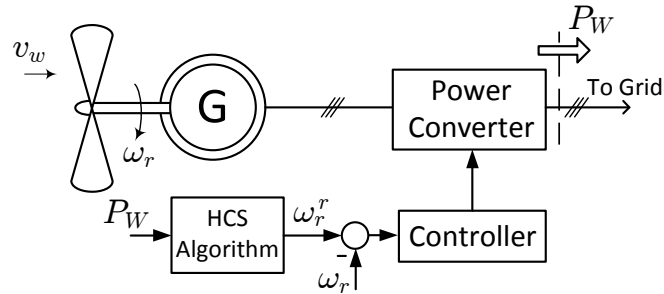


Figure 1.9: Hill-climb search control in a WECS.

### Real-Power Control Strategies in WECSs

In a variable-speed WECS, the power-electronic converter controls the real power that is extracted from the wind, which can be either the maximum available power for the MPPT operation or a constant power. The MPPT algorithms presented in the literature can be classified into three main control methods including the tip-speed ratio (TSR) control, hill-climb search (HCS) control, and power signal feedback (PSF) control [61].

In the TSR control method, the turbine angular speed is regulated such that the ratio between the turbine angular speed and the wind speed is maintained equal to an optimum value at which the power extraction is maximum [62]. This method requires both the wind speed and the turbine angular speed to be measured or estimated. The knowledge of the optimum ratio between the turbine angular speed and the wind speed is also needed for maximum power extraction. Figure 1.8 shows the block diagram of a WECS with TSR control.

The HCS control algorithm continuously searches for the maximum power point of the WECS [63],[64]. The tracking algorithm computes the desired optimum signal to drive the WECS to the point of maximum power based on the location of the current operating point and the relation between the changes in the rotor angular speed and the output power. Figure 1.9 shows the block diagram of a WECS with HCS control. This

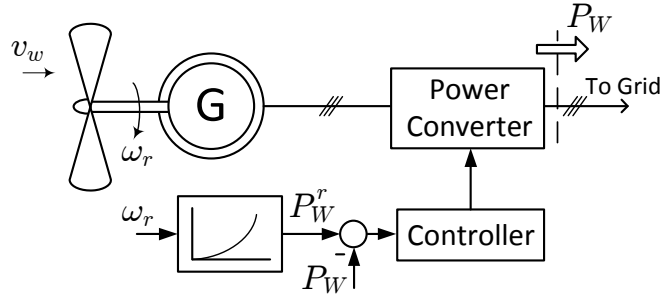


Figure 1.10: Power signal feedback control in a WECS.

method could be ineffective for large WECSs, because it is difficult to rapidly adjust the rotor speed in a large turbine.

In the PSF control method, the power-electronic converter adjusts the WECS output power at its setpoint, which is generated by using either a recorded maximum power curve or the characteristic curve of the turbine [65]. The rotor angular speed (or the wind speed) is fed as the input signal to the control system. In this method, the knowledge of the turbine maximum power curve is required. The maximum power curve is obtained via simulations or offline experiments on individual wind turbines. Figure 1.10 shows the block diagram of a WECS with PSF control for maximum power extraction. The PSF control method is widely used in the commercial WECSs because it is independent of the wind speed and can produce smoother output power compared to the other strategies [61]. Moreover, PSF can be utilized to satisfy different power requirements, such as smoothed or constant output power, by simply applying different power setpoint designs. Therefore, in this thesis, the PSF control method is used for the MPPT operation.

### Damping Drive-Train Torsional Modes

As discussed in Section 1.3.1, a supplementary damping scheme can provide an effective and flexible way to suppress the drive-train torsional modes in a WECS, which results in an active solution rather than passive methods. The solution to damp the drive-train oscillations is known from the large synchronous generators in power systems, where a power system stabilizer (PSS) provides damping for rotor speed oscillations by controlling the excitation of the synchronous generator. The PSS feeds a measure of the rotor speed oscillations into the generator excitation control. Therefore, the terminal voltage of the generator is influenced such that the generator output power and, consequently, the electrical torque of the generator is affected. To counteract the rotor speed oscillations, the PSS produces a damping electrical torque in phase with the rotor speed oscillations.

In the work presented in reference [66], a similar method is applied to a variable-speed WECS that employs an electronically-excited synchronous generator. The generator is connected to the host utility grid through a power-electronic ac-dc-ac converter which uses a diode rectifier to interface the terminals of the synchronous generator to the capacitor of the dc link. Hence, the dc-link voltage in this configuration is proportional to the generator terminal voltage. It is suggested in [66] that the excitation of the synchronous generator be controlled, based on a measure of the rotor speed oscillations, to transiently affect the generator terminal voltage and, consequently, the voltage across the dc-link capacitor. By periodic short-term charging and discharging of the dc-link capacitor as a result of changing the generator excitation voltage, energy is respectively stored in and released from the capacitor, and the generator electrical power varies. This, in turn, can influence the generator torque such that it counteracts the drive-train oscillations and provides damping.

References [31], [67], and [68] adopt the damping method of [66] for a PMSG-based WECS. The interface ac-dc-ac converter consists of two back-to-back voltage-sourced converters (VSCs). Because the PMSG has a fixed excitation, the damping scheme is supplemented into the controller of the ac-dc-ac converter, where instead of the generator excitation in the configuration presented in [66] the generator electrical torque or the dc-link voltage is directly regulated to provide damping for the rotor speed oscillations. In the method presented in reference [31] the dc-link voltage setpoint is augmented by a damping signal which is, in turn, determined by passing the rotor angular speed through a bandpass filter and a phase compensator, whereas in the work published in reference [67] the damping signal is calculated based on the estimated dc-link capacitor current and is supplemented into the electrical torque setpoint of the generator. A correct identification of the frequency and phase angle of the rotor speed oscillations with respect to the supplementary damping signal is important in these strategies. Compared with [31], the proposed strategy in [67] requires no additional sensors and can be applied to the WECSs with different output power requirements. Alternatively, reference [68] generates the damping signal from a state feedback, utilizing a Kalman filter for estimating the states, and augments the aforementioned signal into the generator electrical torque.

### **Contribution of WECSs to Frequency Regulation**

In a CPP, the inertial frequency response is naturally provided by the energy that is released from (or absorbed into) the rotating mass of the synchronous generator subsequent

to a significant frequency disturbance; this reduces the ROCOF, before the governor reacts after some delay. The action of the governor increases (or decreases) the output real power of the CPP and restores the power balance in the power system. In general, large inertia of the power system is desirable for frequency stability and makes up for the deficient power in the few seconds when the governors are too slow to respond. In a variable-speed WECS, however, the turbine angular speed is not related to the grid frequency. Therefore, an additional control is required to provide the aforementioned missing link, to artificially create an inertial frequency response [69]. The significant amount of kinetic energy of a large turbine (in the per-unit sense) renders the inertia of the host WECS potentially comparable to that of a CPP. However, care should be taken in terms of the extent by which the turbine is allowed to decelerate, to ensure the recovery of the turbine angular speed to its pre-contingency value [70],[71]. The over-frequency events in a power system could also be stressful to power components. Temporary high frequency swings can present a reliability concern [72]. Because variable-speed WECSs are connected to the grid via power-electronic converters, their output power can be rapidly reduced for the duration of the over-frequency event. This behavior is similar to that of the governor control in a CPP, except that it is faster and allows larger power change than is typical of a CPP.

Different methods have been proposed in the literature to utilize the stored kinetic energy of a WECS. In these methods, the WECS is delivering the maximum available power to the grid during the normal operation. In case of a significant frequency drop, the WECS provides extra power in its output by extracting the kinetic energy of its rotor. Hence, this inertial response is essentially energy neutral, meaning that the period of increased output power is followed by a period of decreased output power. Reference [53] suggests that the inertial frequency response be provided by assigning a constant power (e.g., equal to 1 pu) to be delivered by the constituting WECSs in a wind farm to the grid for a preset period of time, subsequent to a significant frequency drop. The method is thus based on the assumption that a centralized intelligence switches the control mode of the WECSs, from the normal control mode (i.e., extracting maximum energy from the wind) to a contingency control mode, when a significant frequency drop is detected. The raise of the output power is performed simultaneously in all the constituting WECSs to concentrate the kinetic energy discharge for the duration of the preset discharge time. To avoid a large aggregate wind power reduction, the constituting WECSs in the wind farm are switched back to their normal modes at different times; this ensures that the overall

wind farm output power does not decline sharply. Consequently, each constituting WECS will experience a different recovery time. Moreover, the angular speed of the turbines is not allowed to fall below 0.7 pu. Simulations performed in reference [53] indicates that when the angular speed of the turbine becomes too low, it takes too long for the rotor to accelerate back to the normal operation mode. The results show that a wind farm can be arranged to yield improved performance over individual control of the constituting WECSs.

In the work presented in reference [73], an extra power command is added on top of the power setpoint that is delivered to the grid during the normal operation, if a significant frequency drop is detected. The extra power injection continues until the angular speed of the turbine reaches a minimum value which is assigned as 0.7 pu. Then, the output power of the WECS is switched to a pre-defined value below its mechanical power and the rotor accelerates back towards the pre-contingency operating point and recovers the kinetic energy that was delivered to the grid during the over-production period. Reference [73] also investigates the inertial response contribution of a WECS at different operating points, and with different amounts of over-production. It concludes that the inertial response contribution from a WECS is highly dependant on the turbine operational condition and the prevailing wind speed. It is suggested in reference [74] that a temporary increase be made in the output power of a WECS in the range of 5% to 10% of the its rated power, in case of a significant frequency drop. The duration of the power increase is in the order of several seconds. The design is performed to create a sufficient margin over the WECS operating range to meet the equivalent energy contribution of a synchronous generator with an inertia constant equal to 3.5 s, for the initial 10 seconds. Reference [75] presents an algorithm to estimate and control the quantity of extractable kinetic energy stored in a wind farm during a frequency drop, in order to manage the release of kinetic energy within a given time span. However, it requires several parameters as inputs to the proposed algorithm.

References [76] and [77] propose an auxiliary inertia-emulating control whose quality of response can be tuned by two parameters. It is suggested in [76] that the parameters be selected such that the inertial frequency response of a WECS emulates that of a CPP with a pre-specified inertia constant. Alternatively, the work published in [77] characterizes the impact of the two parameters for the best overall performance of the WECS within the host power system. The additional energy provided by the inertial response of a WECS is restricted by the actual amount of kinetic energy stored in its rotor, the acceptable range

of the rotor speed variations, and the post-contingency effect of re-establishing the rotor speed (and, thus, the kinetic energy) to the pre-contingency value. It should be noted that because the wind power is stochastic and cannot be depended on to compensate for the generation losses, generation reserves from other power plants should be planned as standby. The function of the inertial response of the WECSs is to solely provide extra power for a few seconds during which the governors of the CPPs with generation reserves are too slow to provide power, in order to decrease the rate of the frequency decline [78].

The ability of a WECS to contribute to the primary frequency response depends on the amount of its wind generation reserve [79], which is deployed by a droop-based mechanism similar to the one employed in CPPs [80]. Consequently, the WECS may operate at a reduced output power rather than at its maximum available power; this is the expense to be incurred for an increased integration of wind energy with the power system, especially in weak power systems where maintaining a generation reserve in the WECS can be more valuable to the power system than maximizing the wind generation [81]. References [74] and [77] report that a wind generation reserve of up to 10% should represent a suitable balance between an effective primary frequency response and the lost energy capture. The wind generation reserve can be established through either balance or delta power control. The objective of the delta power control is to maintain a constant generation reserve at all times, whereas the balance power control imposes a constant setpoint for the WECS output real power. Therefore, in the balance power control the amount of generation reserve depends on the maximum available wind power at the prevailing wind speed and, thus, is not constant. Limits on the maximum rates at which the WECS output power is allowed to change may also be imposed.

Due to the intermittent nature of wind, control of a WECS output power is a challenging task [82]. Demanding a WECS to supply an output power more than its maximum available power may arise stability problems. Therefore, an appropriate coordination between the stability and the controllability of the system should be considered in modern WECSs.

## 1.6 Summary and Conclusion

A brief introduction to the concept of the wind energy conversion systems and the importance of wind power for future power systems was provided in this chapter. Challenges associated with large integration of wind power and the motivations behind the con-

ducted research were also discussed. Further, the research objectives and contributions, and a literature survey pertinent to thesis contributions were presented in the chapter.

# Chapter 2

## Real Power Control of a Direct-Drive PMSG-Based WECS

### 2.1 Introduction

As discussed in Chapter 1, the anticipated large-scale integration of WECSs into the electric power system indicates that the system operators should be able to control the output real and reactive powers of WECSs, to more effectively control the power system and operate through grid contingencies. While the reactive power controllability of electronically-interfaced WECSs is widely recognized, their real power controllability has received insignificant attention and, thus far, been merely utilized for MPPT.

In this chapter, a strategy is proposed for output real-power control of a direct-drive WECS that employs a high-pole PMSG; the choice is based on the expectation that PMSG-based WECSs will be widely deployed in the future, due to their low-loss generators, low maintenance requirements, and quiet drive-trains [16]. The proposed real-power control strategy is based on rapid torque control, rather than the (slow) pitch-angle control presented in [53], [83], and [84]. Therefore, the pitch-angle control is not exercised for output real-power control, but it is employed, exclusively and, as per the common practice, for limiting the mechanical power if the turbine overspeeds.

Rapid torque control, however, can excite drive-train torsional modes, especially because the drive-train stiffness is, in general, inversely proportional to the number of generator poles and is therefore low in a WECS with a high-pole PMSG. Moreover, a high-pole PMSG possesses no inherent damping. Drive-train oscillations, if not damped, impact the operation and may even lead to instabilities. Thus, a supplementary damping



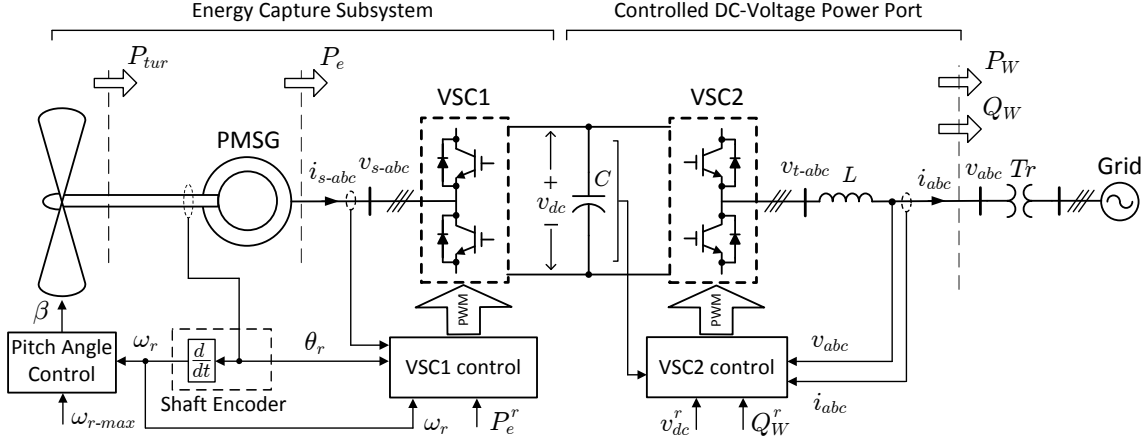


Figure 2.1: Simplified schematic diagram of the direct-drive WECS.

scheme is presented and tuned for the proposed power control strategy, based on a detailed mathematical model and eigenvalue analysis of the WECS. The proposed control strategy and its supplementary damping scheme enable the control of the WECS output real power, from a low value up to the maximum power corresponding to the prevailing wind speed. The damping strategy, however, is not unique and may be achieved through other reported techniques [31], [67], and [68].

## 2.2 Structure of the Direct-Drive WECS

Figure 2.1 illustrates a simplified schematic diagram of a direct-drive PMSG-based WECS. The WECS is composed of a wind turbine, which is directly coupled to a high-pole PMSG, and a power-electronic ac-dc-ac converter, which interfaces the PMSG to the host utility grid. The ac-dc-ac converter, in turn, consists of two back-to-back voltage-sourced converters, VSC1 and VSC2, which are switched based on the pulsewidth modulation (PWM) strategy; these converters are connected from their dc sides in parallel with a dc-link capacitor. The converter VSC1 controls the PMSG electrical torque and, thus, the power that the PMSG extracts from the turbine, whereas VSC2 regulates the dc-link voltage by controlling the real power that is exchanged with the grid. The converter VSC2 can also exchange reactive power with the grid, to support the grid or enhance voltage stability [86]. In Figure 2.1, the composition of the wind turbine, PMSG, VSC1, and the scheme that controls VSC1 is labeled as the *energy capture subsystem*, whereas the composition of the dc-link capacitor, VSC2 and its tie reactor,  $L$ , and the control scheme for dc-link voltage regulation and reactive-power control is identified as the *con-*

trolled dc-voltage power port [87]. In this chapter, the dynamics of the energy capture subsystem are exclusively studied; this is possible because the arrangement shown in Figure 2.1 effectively decouples the utility grid dynamics from those of the wind turbine, drive-train, and PMSG.

## 2.3 Mathematical Model and Control Schemes

This section presents a mathematical model for the energy capture subsystem of the WECS in Figure 2.1. For the sake of compactness, hereafter, the same notation will be adopted for a variable and its Laplace transform. In addition, the superscript  $r$  signifies the reference value (setpoint) for a variable.

### 2.3.1 Aerodynamic Model of the Turbine

The mechanical torque of a wind turbine is given by [3]:

$$T_{tur} = \frac{P_{tur}}{\omega_t} = \frac{0.5 \pi R^2 \rho C_p(\lambda, \beta) v_w^3}{\omega_t}, \quad (2.1)$$

where  $T_{tur}$  is the turbine torque (in Nm),  $P_{tur}$  is the turbine power (in watts),  $\omega_t$  is the turbine angular speed (in rad/s),  $R$  is the turbine radius (in m),  $\rho$  is the air mass density (in kg/m<sup>3</sup>),  $v_w$  is the wind speed (in m/s), and  $C_p$  (unitless) is the turbine so-called power efficiency which depends on the aerodynamic characteristics of blades and is formulated as [3]

$$C_p = \alpha_1 \left( \frac{\alpha_2}{\lambda_i} - \alpha_3 \beta - \alpha_4 \beta^{\alpha_5} - \alpha_6 \right) e^{-\frac{\alpha_7}{\lambda_i}}, \quad (2.2)$$

where

$$\lambda_i = \left( \frac{1}{\lambda + \alpha_8 \beta} - \frac{\alpha_9}{\beta^3 + 1} \right)^{-1}, \quad (2.3)$$

and

$$\lambda = \frac{R\omega_t}{v_w}, \quad (2.4)$$

$\alpha_1, \dots, \alpha_9$  are constant parameters whose typical values are given in Table A.1 (see Appendix A),  $\beta$  is the pitch angle (in degrees), and the variable  $\lambda$  (unitless) is known as

the turbine tip-speed ratio.

The highest values of  $C_P$  are typically obtained for the values of  $\lambda$  in the range of 8 to 9, i.e., when the tip of the blades move 8 to 9 times faster than the incoming wind [6]. It should be noted that the one main advantage of using the variables  $C_P$ ,  $\lambda$ , and  $\beta$  is that regardless of the size of the wind turbine these quantities are normalized values and thus comparable.

### 2.3.2 Drive-Train

As discussed in Section 1.3.1, a two-mass model of the drive-train is sufficient, with reasonable accuracy, for capturing the dynamics that affect the stability of a WECS. Therefore, to more accurately characterize the drive-train dynamics, a two-mass model is adopted in which one mass represents the turbine inertia, and the other mass models the generator inertia. Ignoring the mechanical losses, the drive-train is represented by the following two-mass model:

$$J_t \frac{d\omega_t}{dt} = T_{tur} - k_s \gamma, \quad (2.5)$$

$$J_r \frac{d\omega_r}{dt} = k_s \gamma - T_e, \quad (2.6)$$

$$\frac{d\gamma}{dt} = \omega_t - \omega_r, \quad (2.7)$$

where  $\omega_r$  is the PMSG rotor speed (in rad/s); parameters  $J_t$  and  $J_r$  respectively signify the turbine and PMSG moments of inertia (in  $\text{kgm}^2$ ), and  $k_s$  is the drive-train stiffness (in  $\text{Nm/rad}$ ); the variable  $\gamma$  represents the torsional displacement of the drive-train (in radians); and the variable  $T_e$  denotes the PMSG torque (in  $\text{Nm}$ ). Equations (2.1) through (2.7) constitute a state-space drive-train model for the energy capture subsystem.

### 2.3.3 Permanent-Magnet Synchronous Generator

The objective of VSC1 is to control the PMSG current and, thus, the electrical torque. In turn, the control of the PMSG torque enables the control of the PMSG power, which is used for either MPPT or controlled-power operation of the WECS, as will be discussed in Section 2.4.

The PMSG current/torque control is performed in a rotating  $dq$  frame whose direct axis is aligned with the PMSG rotor flux vector [87], and is implemented through the

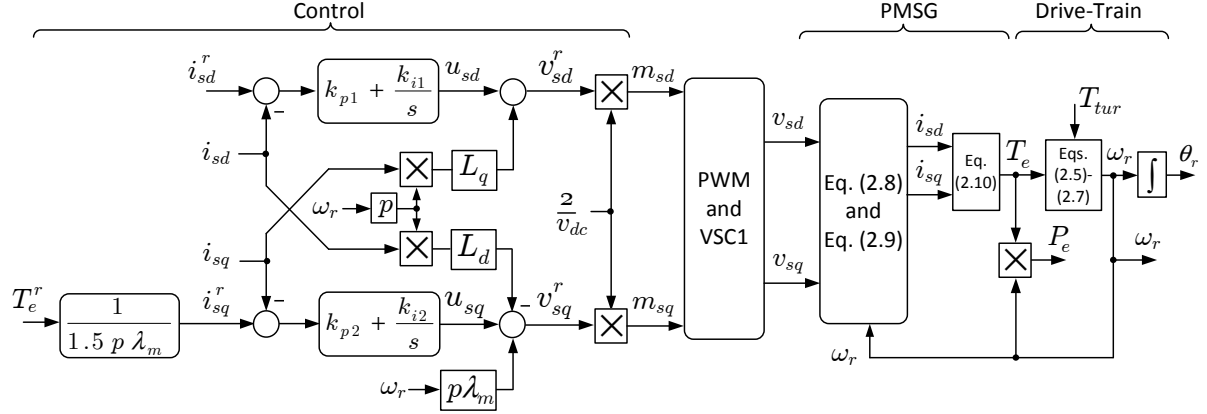


Figure 2.2: Block diagram of the PMSG torque control scheme.

scheme illustrated in Figure 2.2, based on the equations:

$$L_d \frac{di_{sd}}{dt} = -R_s i_{sd} + \underbrace{p\omega_r L_q i_{sq}}_{u_{sd}} - v_{sd}, \quad (2.8)$$

$$L_q \frac{di_{sq}}{dt} = -R_s i_{sq} - \underbrace{p\omega_r L_d i_{sd} + p\omega_r \lambda_m}_{u_{sq}} - v_{sq}, \quad (2.9)$$

$$T_e = 1.5p [\lambda_m i_{sq} + (L_d - L_q) i_{sd} i_{sq}], \quad (2.10)$$

in which  $L_d$  and  $L_q$  (in H) are two constant parameters of inductance dimension; the parameter  $R_s$  (in  $\Omega$ ) is the per-phase resistance of the PMSG stator windings ; the variables  $v_{sd}$  and  $v_{sq}$  (in V) are  $d$ - and  $q$ - axis components of the PMSG stator voltage; the variables  $i_{sd}$  and  $i_{sq}$  (in A) signify the  $d$ - and  $q$ - axis components of the PMSG three-phase stator current; the parameter  $\lambda_m$  (in Wb) represents the maximum flux produced by the PMSG rotor magnets and linked by the stator windings; and  $p$  is the PMSG number of pole pairs.

To control the PMSG torque, the current components  $i_{sd}$  and  $i_{sq}$  must first be controlled. In turn, these two current components are controlled by the stator voltage components  $v_{sd}$  and  $v_{sq}$ , respectively. Thus, as Figure 2.2 illustrates, two corresponding proportional-integral (PI) compensators process the error signals  $i_{sd}^r - i_{sd}$  and  $i_{sq}^r - i_{sq}$ , and generate the desired voltage components  $v_{sd}^r$  and  $v_{sq}^r$ , respectively. Figure 2.2 also indicates that the compensator outputs are augmented with appropriate feed-forward signals, based on (2.8) and (2.9), such that the control of  $i_{sd}$  and  $i_{sq}$  are independent. The signals  $v_{sd}^r$  and  $v_{sq}^r$  are then normalized to the converter gain,  $v_{dc}/2$ , to generate  $m_{sd}$  and  $m_{sq}$ , that is, the  $d$ - and  $q$ -axis components of the PWM modulating signals

of VSC1. Finally, the PWM modulating signals,  $m_{s-abc}(t)$ , are generated by  $dq$ -to- $abc$  frame transformation of  $m_{sd}$  and  $m_{sq}$  (not shown in Figure 2.2), using the angle  $p\theta_r$  ( $\theta_r$  is the PMSG rotor angle). It should also be pointed out that the current components  $i_{sd}$  and  $i_{sq}$  are obtained through  $abc$ -to- $dq$  frame transformation of the stator current  $i_{s-abc}(t)$  (not shown in Figure 2.2), using the angle  $p\theta_r$ .

As discussed in [87], if the PI compensators are tuned such that

$$k_{p1} = \frac{L_d}{\tau_i}, \quad (2.11)$$

$$k_{p2} = \frac{L_q}{\tau_i}, \quad (2.12)$$

$$k_{i1} = k_{i2} = \frac{R_s}{\tau_i}, \quad (2.13)$$

where  $\tau_i$  is a design parameter of time dimension, then the closed-loop responses of  $i_{sd}$  and  $i_{sq}$  to their respective setpoints are described by the following first-order transfer functions

$$i_{sd} = \frac{1}{\tau_i s + 1} i_{sd}^r, \quad (2.14)$$

$$i_{sq} = \frac{1}{\tau_i s + 1} i_{sq}^r, \quad (2.15)$$

for which  $\tau_i$  turns out as the time constant.

In a high-pole PMSG, the values of  $L_d$  and  $L_q$  are fairly close and can be assumed to be equal [88]. Hence, as (2.10) indicates,  $T_e$  is predominantly dependant on  $i_{sq}$ . By contrast,  $i_{sd}$  does not contribute much to the torque development and, therefore, can be regulated at zero to minimize the PMSG current for a given torque. Assuming that  $i_{sd} = 0$  and multiplying (2.15) by  $1.5p\lambda_m$ , one deduces

$$T_e = \frac{1}{\tau_i s + 1} T_e^r, \quad (2.16)$$

where

$$T_e^r = 1.5 \lambda_m i_{sq}^r. \quad (2.17)$$

As Figure 2.2 shows, the current setpoint  $i_{sq}^r$  is calculated from the torque setpoint  $T_e^r$ , based on (2.17).

Once the PMSG torque can be controlled, the PMSG power can be regulated. Figure

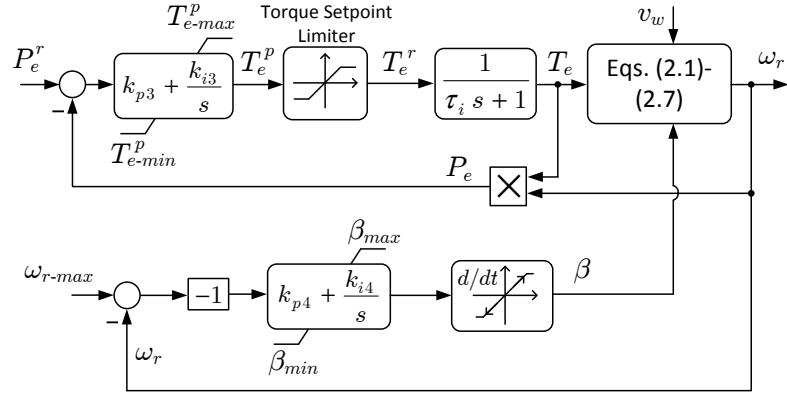


Figure 2.3: Block diagram of the basic power control scheme.

2.3 shows the block diagram of a basic control scheme whose prime function is to force the PMSG power,  $P_e$ , to track the power setpoint  $P_e^r$ . The objective is fulfilled by processing the error  $P_e^r - P_e$  by a compensator which, for simplicity, is selected to be of the PI type. The compensator output,  $T_e^p$ , is then passed through a limiter and determines the PMSG torque setpoint  $T_e^r$  for the torque control scheme of Figure 2.3; the limiter is to protect VSC1 and PMSG from overcurrent. The feedback signal  $P_e$  can be calculated by multiplying  $T_e$  and  $\omega_r$ , as shown in Figure 2.3; for this process,  $T_e$  can be obtained from  $T_e^r$ , based on (2.16). The setpoint  $P_e^r$  is determined based on the mode of operation, as will be explained in the next section.

Figure 2.3 also illustrates the pitch-angle control process whose function is to ensure that the turbine and PMSG speeds do not exceed the maximum permissible value,  $\omega_{r-max}$ . Therefore, if  $\omega_r$  exceeds  $\omega_{r-max}$ , a PI compensator increases  $\beta$  to decrease the turbine power and regulate  $\omega_r$  at  $\omega_{r-max}$ ; if  $\omega_r$  is smaller than  $\omega_{r-max}$ , the compensator output is saturated at its lower value,  $\beta_{min}$ , to maximize the turbine power. Figure 2.3 further shows that the PI compensator output passes through a rate limiter which represents the limited speed at which the pitch angle can be changed in practice.

## 2.4 Control Strategy and Modes of Operation

The pervasive penetration of wind power into the electric power system indicates that WECSs should also be able to take part in the power-flow control process which, presently, is exclusively undertaken by the conventional power plants; the feature should supplement the MPPT capability that modern WECSs currently possess. As such, two modes of operation are defined for the WECS of Figure 2.1: (1) the MPPT mode, and (2) the

controlled-power (CP) mode. The operating mode is determined by the way that the setpoint  $P_e^r$  is stipulated, as explained next.

### 2.4.1 MPPT Mode of Operation

In the MPPT mode, the objective is to maximize the power that the turbine extracts from wind. Based on (2.1), this can be achieved if  $C_p$  is maximized. To maximize  $C_p$ , the turbine tip-speed ratio must be kept constant at its optimum value,  $\lambda_{opt}$ , regardless of the wind speed;  $\lambda_{opt}$  is the tip-speed ratio at which  $C_p$  peaks, for the minimum pitch angle. The objective is fulfilled if the PMSG power setpoint is determined based on the following law [89]:

$$P_e^r = k_{opt} \omega_r^3, \quad (2.18)$$

in which the constant  $k_{opt}$  (in  $\text{Nms}^2/\text{rad}^2$ ) is a parameter (that depends on the turbine construction and characteristic), and can be obtained by evaluating  $C_p$  for  $\lambda = \lambda_{opt}$  and  $\beta = \beta_{min}$ , and is given by [89]:

$$k_{opt} = \frac{0.5 \pi R^5 \rho}{\lambda_{opt}^3} C_p(\lambda_{opt}, \beta_{min}). \quad (2.19)$$

It then follows from assuming a fast control that  $P_e \approx P_e^r$ . Thus, (2.18) can be rewritten as

$$P_e = k_{opt} \omega_r^3. \quad (2.20)$$

Figure 2.4 illustrates the characteristic curves of a wind turbine, for a wind speed and two different values of pitch angle, that is,  $\beta_{min}$  (heavy solid line) and  $\beta > \beta_{min}$  (light solid line). The figure also plots the PMSG power versus rotor speed, based on (2.20) (dashed line). It is observed that if the WECS is in the MPPT mode and the rotor speed is smaller than  $\omega_{r-opt} = \lambda_{opt} v_w / R$ , then the turbine mechanical power,  $P_{tur}$ , is larger than the PMSG electrical power,  $P_e$ , and, therefore, the rotor speed increases towards the value  $\omega_{r-opt}$ . By contrast, if the rotor speed is larger than  $\omega_{r-opt}$ ,  $P_{tur}$  is smaller than  $P_e$ , and  $\omega_r$  decreases. In a steady state,  $P_{tur}$  equals  $P_e$ , and  $\omega_r$  settles at the value  $\omega_{r-opt}$ . Thus, point A on Figure 2.4 is a stable operating point corresponding to the maximum turbine power at the given wind speed. Based on (2.20), the maximum power,  $P_{opt}$ , can

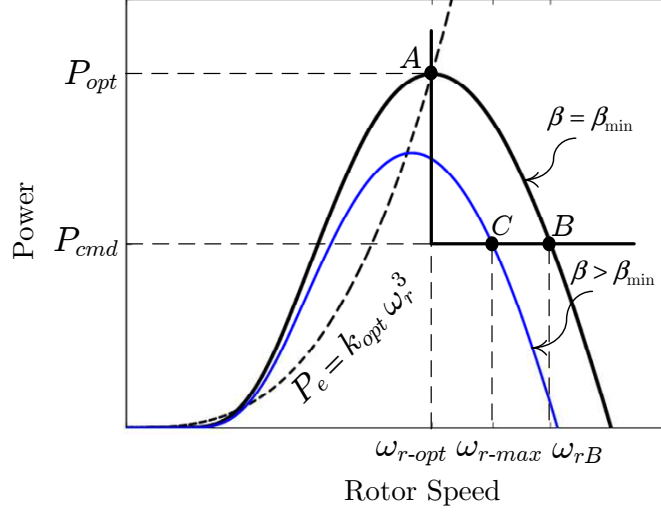


Figure 2.4: Characteristic curves of a wind turbine for a wind speed and two different values of pitch angle.

be formulated as

$$P_{opt} = k_{opt} \omega_{r-opt}^3 \quad (2.21)$$

It should also be noted that using  $k_{opt} \omega_r^3$  as the power setpoint in the MPPT mode of operation generates a smooth output power. This is because the changes in the rotor speed caused by the wind speed variations is slow due to the high inertia of the WECS rotor.

### 2.4.2 Controlled-Power Mode of Operation

In the CP mode, the objective is to regulate the WECS output power at the command value  $P_{cmd}$ , regardless of the wind speed. Therefore,  $P_e^r$  is given the value of  $P_{cmd}$ . Let us assume that, initially, the WECS is in the MPPT mode,  $\beta = \beta_{min}$ ,  $P_e = P_{tur} = P_{opt}$ , and  $\omega_r = \omega_{r-opt}$ ; then the value of  $P_e^r$  (and therefore  $P_e$ ) is rapidly changed from  $P_{opt}$  to  $P_{cmd}$ , i.e., subsequent to a switching from the MPPT mode to the CP mode. As Figure 2.4 indicates, this causes the PMSG power to drop below the turbine power and results in an increase in  $\omega_r$  towards the value  $\omega_{rB}$ . Depending on the wind speed,  $\omega_{rB}$  can be larger than the maximum permissible rotor speed,  $\omega_{r-max}$ , as for the example illustrated in Figure 2.4. The situation is circumvented by the pitch-angle control mechanism; thus, once  $\omega_r$  exceeds  $\omega_{r-max}$ , the pitch-angle control scheme increases  $\beta$  and consequently alters the power-speed characteristic of the wind turbine, to the one shown by light solid



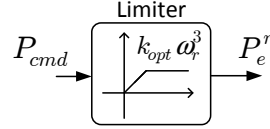


Figure 2.5: Block diagram illustrating the generation of the power setpoint.

line in Figure 2.4, such that  $P_{tur}$  drops to  $P_{cmd}$  and the rotor speed settles at  $\omega_{r-max}$  (corresponding to the point C in Figure 2.4). To ensure that the PMSG and turbine power-speed curves have at least one crossing point [see Figure 2.4],  $P_e^r$  in the CP mode is limited to the value  $k_{opt} \omega_r^3$ . Therefore, if  $P_{cmd}$  is so large that the turbine power cannot overtake it at the given wind speed, then  $P_e^r$  will be limited to  $k_{opt} \omega_r^3$  and, effectively, the system continues to operate in the MPPT mode until either there will be a rise in the wind speed (thus increasing the corresponding  $P_{opt}$ ) or the system operator steps down the command  $P_{cmd}$ .

Figure 2.5 illustrates the proposed mechanism for selecting between the MPPT and CP modes of operation. As Figure 2.5 shows, the setpoint  $P_e^r$  is obtained from the output of a hard limiter whose input and upper saturation limit are  $P_{cmd}$  and  $k_{opt} \omega_r^3$ , respectively (the lower saturation limit is zero). Thus,  $P_e^r$  is equal to  $P_{cmd}$ , and the CP mode is exercised, as long as  $P_{cmd}$  is smaller than  $k_{opt} \omega_r^3$ ; otherwise,  $P_e^r$  is equal to  $k_{opt} \omega_r^3$  and the energy capture subsystem operates in the MPPT mode. Therefore, to permanently leave the system in the MPPT mode, it is sufficient to assign  $P_{cmd}$  an adequately large value (e.g., larger than the value of  $P_{opt}$  that corresponds to the rated wind speed).

## 2.5 Eigenvalue Analysis

An eigenvalue analysis is performed to reveal the dynamic properties of the energy capture subsystem and to tune the parameters of the proposed power control strategy. To that end, the subsystem equations are first linearized about an operating point, and then the linearized model is analyzed. The numerical examples presented in this chapter are based on an example WECS whose parameters are given in Appendix A. The same example WECS has also been simulated in time domain for producing the results reported in Section 2.7.

As Figure 2.3 indicates, the compensator of the power control scheme can be described

by

$$T_e^p = \left( k_{p3} + \frac{k_{i3}}{s} \right) (P_e^r - P_e). \quad (2.22)$$

Replacing  $P_e$  by  $T_e \omega_r$  in (2.22) and expanding the resultant in time domain, one finds

$$\begin{aligned} \frac{dT_e^p}{dt} = & -k_{p3} \omega_r \frac{dT_e}{dt} - k_{p3} T_e \frac{d\omega_r}{dt} - k_{i3} T_e \omega_r \\ & + k_{p3} \frac{dP_e^r}{dt} + k_{i3} P_e^r. \end{aligned} \quad (2.23)$$

It also follows from (2.16) that

$$\frac{dT_e}{dt} = -\frac{1}{\tau_i} T_e + \frac{1}{\tau_i} T_e^p. \quad (2.24)$$

As Figure 2.3 indicates, if saturation is ignored,  $T_e^r$  can be replaced by  $T_e^p$  and (2.24) is rewritten as

$$\frac{dT_e}{dt} = -\frac{1}{\tau_i} T_e + \frac{1}{\tau_i} T_e^p. \quad (2.25)$$

Eliminating  $d\omega_r/dt$  between (2.23) and (2.6), and then substituting for  $dT_e/dt$  from (2.25) in the resulting equation, one deduces

$$\begin{aligned} \frac{dT_e^p}{dt} = & -\frac{k_{p3}}{\tau_i} (T_e^p - T_e) \omega_r - k_{p3} T_e \left( \frac{k_s}{J_r} \gamma - \frac{1}{J_r} T_e \right) \\ & - k_{i3} T_e \omega_r + k_{p3} \frac{dP_e^r}{dt} + k_{i3} P_e^r. \end{aligned} \quad (2.26)$$

Equations (2.5) through (2.7), (2.25), and (2.26), along with the algebraic equations (2.1) through (2.3), constitute the following nonlinear state-space model for the energy capture subsystem:

$$\frac{d\mathbf{X}_n}{dt} = \mathbf{F}(\omega_t, \omega_r, \gamma, T_e, T_e^p, P_e^r, \frac{dP_e^r}{dt}, v_w), \quad (2.27)$$

for which  $\mathbf{X}_n = [\omega_t, \omega_r, \gamma, T_e, T_e^p]^T$  is the vector of state variables (Superscript  $T$  denotes matrix transposition),  $P_e^r$  and  $dP_e^r/dt$  are the (inter-related) control inputs, and  $v_w$  is the disturbance input.  $\mathbf{F}(\cdot)$  is a vector of nonlinear functions of the state variables and inputs. It should be noted that (2.27) assumes a constant pitch angle (i.e., it ignores the dynamics of the pitch-angle control mechanism) to keep the mathematical model

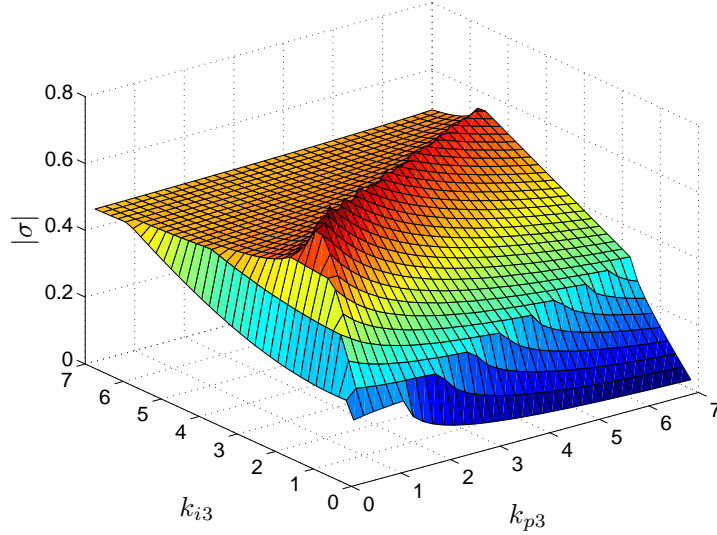


Figure 2.6: Absolute value of the real part of  $\mathbf{A}_1$  dominant eigenvalue as a function of  $k_{p3}$  and  $k_{i3}$ .

tractable. The approximation is plausible because the pitch-angle is normally settled at its minimum value, and varies only if the turbine speed exceeds its maximum value. Moreover, the ignored dynamics are, by design and by nature, remarkably slower than those of the state variables in  $\mathbf{X}_n$ . However, the simulation model used for the assessment of the proposed control strategy includes the pitch-angle control loop (Section 2.7).

In the MPPT mode,  $P_e^r$  is determined based on (2.18). Taking derivatives with respect to time from both sides of (2.18), and eliminating  $d\omega_r/dt$  between the resulting equation and (2.6), one finds

$$\frac{dP_e^r}{dt} = 3k_{opt}\omega_r^2 \left( \frac{k_s}{J_r}\gamma - \frac{1}{J_r}T_e \right). \quad (2.28)$$

Substituting in (2.27) for  $P_e^r$  and  $dP_e^r/dt$ , respectively from (2.18) and (2.28), and expressing the resulting set of equations in the small-signal time-domain form, one deduces

$$\frac{d\tilde{\mathbf{X}}_n}{dt} = \mathbf{A}_1 \tilde{\mathbf{X}}_n + \mathbf{B}_1 \tilde{v}_w, \quad (2.29)$$

where  $\mathbf{A}_1$  and  $\mathbf{B}_1$  are matrices whose elements are functions of the steady-state operating point of the system; and “ $\sim$ ” denotes the small-signal perturbation of a variable; the matrices are introduced in Appendix B.

For the example WECS, Figure 2.6 plots the absolute value of  $\sigma$ , that is, the real part of the dominant eigenvalue of  $\mathbf{A}_1$ , as a function of  $k_{p3}$  and  $k_{i3}$ ; the dominant eigenvalue is

Table 2.1: Eigenvalues of the Energy Capture Subsystem.

MPPT Mode	CP Mode
-97.92	-113.4
-0.97	-1.45
$-0.7 \pm 9.38j$	-0.19
-0.55	$+0.16 \pm 9.23j$

defined as the eigenvalue with the smallest real part (in absolute value), and is calculated for the operating point that corresponds to  $v_w = 9$  m/s. As Figure 2.6 shows,  $|\sigma|$  is maximized if  $k_{p3} = 1.0$  and  $k_{i3} = 2.4$ ; these values are adopted for the subsequent analyses.

In the CP mode,  $P_e^r = P_{cmd}$  and, thus, the linearized version of (2.27) takes the form

$$\frac{d\tilde{\mathbf{X}}_n}{dt} = \mathbf{A}_2 \tilde{\mathbf{X}}_n + \mathbf{B}_2 \begin{bmatrix} \tilde{v}_w \\ \tilde{P}_{cmd} \\ \frac{d\tilde{P}_{cmd}}{dt} \end{bmatrix}, \quad (2.30)$$

where  $\mathbf{A}_2$  and  $\mathbf{B}_2$  are matrices whose elements are functions of the system steady-state operating point; the matrices are introduced in Appendix B.

Table 2.1 reports the eigenvalues of  $\mathbf{A}_1$  and  $\mathbf{A}_2$ , that is, under the MPPT and CP modes of operation, respectively. The eigenvalues are calculated for the operating point that corresponds to  $v_w = 9$  m/s; for the CP mode  $P_e^r = P_{cmd} = 0.75P_{opt}$  (the value of  $P_{opt}$  at the given wind speed in about 2.1 MW). As the table indicates, in both MPPT and CP modes the energy capture subsystem has one negative real eigenvalue which is fairly far from the imaginary axis of the s-plane. This pole is resulted from the delay in the response of the PMSG torque,  $T_e$ , to its setpoint [see equation (2.16)]. Moreover, the system has two other negative real eigenvalues which are closer to the imaginary axis. The negative real eigenvalue with the shortest distance form the imaginary axis represents the slow dynamic of the whole WECS drive-train which is due to its large inertia. The other negative real eigenvalue represents the dynamic of the real-power controller [see Figure 2.3]. In the MPPT mode, the system has one pair of complex-conjugate eigenvalues which correspond to a stable but poorly damped eigenmode and represent the drive-train torsional mode. The situation for the CP mode is even worse; as Table 2.1 indicates, in the CP mode the energy capture subsystem has an unstable

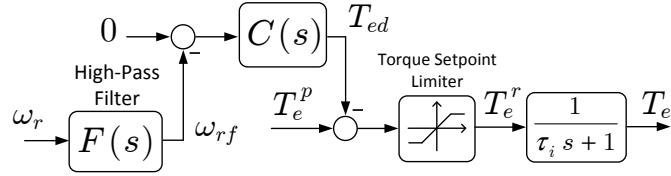


Figure 2.7: Block diagram illustrating the implementation of the damping scheme.

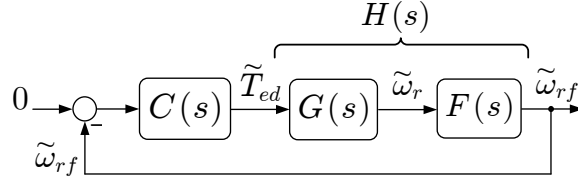


Figure 2.8: Control block diagram of the damping scheme.

oscillatory mode. Thus, both modes of operation call for a damping mechanism, which is described next.

## 2.6 Damping Strategy

### 2.6.1 Structure

The damping scheme presented in this section augments the PMSG torque setpoint with a high-pass filtered measure of the rotor speed, through the scheme illustrated in Figure 2.7. As Figure 2.7 shows, first the ac component of the rotor speed is extracted by passing  $\omega_r$  through a high-pass filter,  $F(s)$ . Then, a compensator,  $C(s)$ , processes the error between zero and the filter output  $\omega_{rf}$ , and determines the supplementary component  $T_{ed}$  for the PMSG torque setpoint  $T_e^r$ . Finally, the resulting torque setpoint is passed through a limiter that prevents  $T_e^r$  from exceeding its maximum permissible value. As illustrated in Figure 2.8, the damping scheme of Figure 2.7 results in a control loop whose objective is to (rapidly) force the ac component of  $\omega_{rf}$  to zero. The design criteria for  $F(s)$  and  $C(s)$  are explained next.

### 2.6.2 Design

The first design step is to decide on the form and parameters of the filter  $F(s)$  whose function is to pass the ac component of  $\omega_r$  with insignificant magnitude or phase shift, at least over the desired frequency spectrum, but to block the dc component of  $\omega_r$ . One

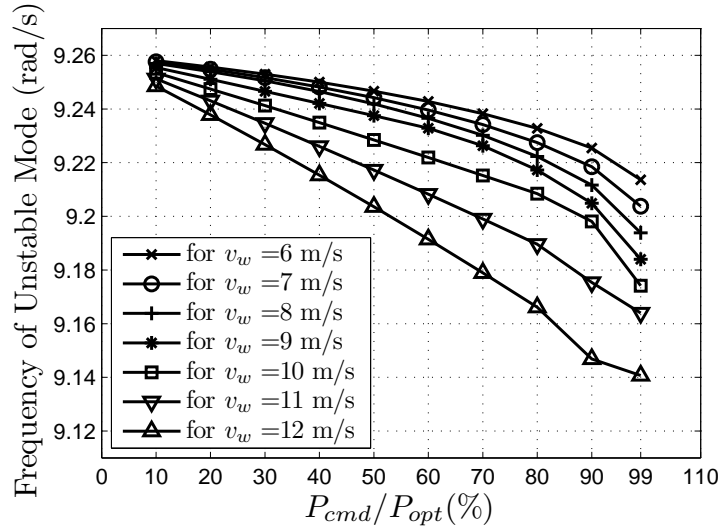


Figure 2.9: Variations of the frequency of unstable mode as a function of the normalized power command in the CP mode of operation.

candidate is a second-order high-pass filter of the form

$$F(s) = \frac{\omega_{rf}(s)}{\omega_r(s)} = \frac{s^2}{s^2 + \left(\frac{\omega_c}{Q}\right)s + \omega_c^2}, \quad (2.31)$$

for which  $\omega_c$  and  $Q$  are the corner frequency and quality factor, respectively. These two parameters determine the frequency response of  $F(s)$  and are selected based on the range of frequencies that need to be passed with fidelity.

For the example WECS, Figure 2.9 shows a family of curves that plot the imaginary part (frequency) of the unstable complex-conjugate eigenvalues in the CP mode (see Table 2.1), for a corresponding set of wind speeds, as a function of the ratio  $P_{cmd}/P_{opt}$ . The value of  $P_{opt}$  is different for each curve and equals the maximum turbine power for the corresponding wind speed [Figure 2.4]. As Figure 2.9 indicates, the frequency of the unstable mode varies over a fairly narrow range about 9.2 rad/s. Considering this frequency band, the choices of  $Q = 0.5$  and  $\omega_c = 0.7$  rad/s result in small difference between the ac components of  $\omega_{rf}$  and  $\omega_r$ , in terms of magnitude and phase angle.

The next design step is to determine the structure and parameters of  $C(s)$ , requiring the calculation of the transfer function from  $\tilde{T}_{ed}$  to  $\tilde{\omega}_r$  [ $G(s)$ , Figure 2.8] while the inputs  $v_w$  and  $P_e^r$  are set to zero. Thus, linearizing (2.5) and (2.7), expressing the resulting equations in the frequency domain, and eliminating  $\tilde{\omega}_t$  between the two frequency-domain

equations, one finds

$$\tilde{\gamma} = -\frac{s - \frac{k_1}{J_t}}{s^2 - \frac{k_1}{J_t}s + \frac{k_s}{J_t}}\tilde{\omega}_r, \quad (2.32)$$

where  $k_1 = \partial T_{tur}/\partial\omega_t$  whose expanded form is presented in Appendix B. On the other hand, expression of (2.6) in the small-signal frequency-domain form yields

$$s\tilde{\omega}_r = \frac{k_s}{J_r}\tilde{\gamma} - \frac{1}{J_r}\tilde{T}_e. \quad (2.33)$$

Eliminating  $\tilde{\gamma}$  between (2.32) and (2.33), one deduces

$$\left(s + \frac{k_s}{J_r} \frac{s - \frac{k_1}{J_t}}{s^2 - \frac{k_1}{J_t}s + \frac{k_s}{J_t}}\right)\tilde{\omega}_r = -\frac{1}{J_r}\tilde{T}_e. \quad (2.34)$$

It then follows from replacing  $T_e^r$  by  $T_e^p - T_{ed}$  in (2.16) [see Figure 2.7] and expressing the resultant equation in the small-signal frequency-domain form that

$$\tilde{T}_e^p = (\tau_i s + 1)\tilde{T}_e + \tilde{T}_{ed}. \quad (2.35)$$

Eliminating  $\tilde{T}_e^p$  between (2.35) and the small-signal frequency-domain form of (2.23), and solving for  $\tilde{T}_e$  based on the resulting equation and substituting it in (2.34), one obtains

$$G(s) = \frac{\tilde{\omega}_r(s)}{\tilde{T}_{ed}(s)} = \frac{n_1 s^3 + n_2 s^2 + n_3 s}{d_1 s^5 + d_2 s^4 + d_3 s^3 + d_4 s^2 + d_5 s + d_6}, \quad (2.36)$$

where

$$n_1 = -\frac{1}{J_r}, \quad (2.37)$$

$$n_2 = \frac{k_1}{J_r J_t}, \quad (2.38)$$

$$n_3 = -\frac{k_s}{J_r J_t}, \quad (2.39)$$

$$d_1 = \tau_i, \quad (2.40)$$

$$d_2 = -\frac{k_1 \tau_i}{J_t} + 1 + k_{p3} \bar{\omega}_r, \quad (2.41)$$

$$d_3 = \frac{\tau_i k_s}{J_t} + k_{i3} \bar{\omega}_r - \frac{k_1}{J_t} (1 + k_{p3} \bar{\omega}_r) + \frac{k_s \tau_i}{J_r} - \frac{k_{p3}}{J_r} \bar{T}_e, \quad (2.42)$$

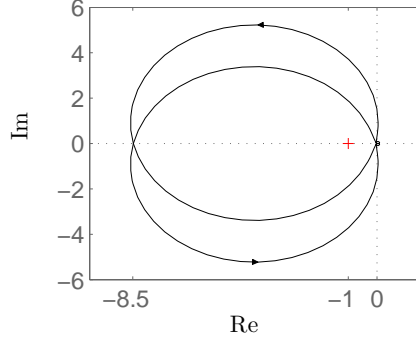


Figure 2.10: Nyquist plot of the open-loop frequency response of Figure 2.8, when  $C(s) = k_d = 10^7$ .

$$d_4 = \frac{k_s}{J_t}(1 + k_{p3}\bar{\omega}_r) - \frac{k_1 k_{i3}}{J_t} \bar{\omega}_r - \frac{k_1 \tau_i k_s}{J_r J_t} + \frac{k_s}{J_r}(1 + k_{p3}\bar{\omega}_r) - \frac{k_{i3} \bar{T}_e}{J_r} + \frac{k_{p3} k_1 \bar{T}_e}{J_r J_t}, \quad (2.43)$$

$$d_5 = \frac{k_s k_{i3}}{J_t} \bar{\omega}_r - \frac{k_s k_1}{J_r J_t} (1 + k_{p3}\bar{\omega}_r) + \frac{k_s k_{i3}}{J_r} \bar{\omega}_r - \frac{k_{p3} k_s \bar{T}_e}{J_r J_t} + \frac{k_{i3} k_1 \bar{T}_e}{J_r J_t}, \quad (2.44)$$

$$d_6 = -\frac{k_s k_1 k_{i3}}{J_r J_t} \bar{\omega}_r - \frac{k_{i3} k_s \bar{T}_e}{J_r J_t}, \quad (2.45)$$

and the overline denotes the steady-state value of a variable.

For the example WECS, Figure 2.10 shows the Nyquist plot of the open-loop gain  $C(j\omega) \times G(j\omega) \times F(j\omega)$  for which  $C(s)$  is a pure gain,  $k_d$ , equal to  $10^7$ . The Nyquist plot of Figure 2.10 is based on the system operating point that corresponds to  $v_w = 9$  m/s and  $P_e^r = P_{cmd} = 0.75P_{opt}$ . For this operating point, two of the loop-gain poles lie in the right-half plane. Therefore, the plot of Figure 2.10 represents a stable system for the choice of  $C(s) = k_d = 10^7$ , and further indicates that the system retains its stability for any value of  $k_d$  that is larger than  $1.18 \times 10^6$ . The optimum value of  $k_d$  is determined through an eigenvalue analysis, as explained next.

### 2.6.3 Eigenvalue Analysis

To assess the effectiveness of the presented damping scheme, and to find the optimum value for the gain  $C(s) = k_d$ , the state-space model of Section 2.5 is modified.

If  $C(s) = k_d$ , as Figure 2.7 indicates the supplementary component of the PMSG torque setpoint is

$$\tilde{T}_{ed} = k_d \tilde{\omega}_{rf}. \quad (2.46)$$



Substitution of  $\tilde{T}_{ed}$  from (2.46) in (2.35) yields

$$\tilde{T}_e = \frac{1}{\tau_i s + 1} \left( \tilde{T}_e^p + k_d \tilde{\omega}_{rf} \right), \quad (2.47)$$

which, in time domain, is equivalent to

$$\frac{d\tilde{T}_e}{dt} = -\frac{1}{\tau_i} \tilde{T}_e + \frac{1}{\tau_i} \tilde{T}_e^p + \frac{k_d}{\tau_i} \tilde{\omega}_{rf}. \quad (2.48)$$

Eliminating  $d\omega_r/dt$  between (2.23) and (2.6), and linearizing the result, one deduces

$$\begin{aligned} \frac{d\tilde{T}_e^p}{dt} = & -k_{p3} \bar{\omega}_r \frac{d\tilde{T}_e}{dt} - k_{p3} \bar{T}_e \left( \frac{k_s}{J_r} \tilde{\gamma} - \frac{1}{J_r} \tilde{T}_e \right) \\ & - k_{i3} \bar{T}_e \tilde{\omega}_r - k_{i3} \bar{\omega}_r \tilde{T}_e + k_{p3} \frac{d\tilde{P}_e^r}{dt} + k_{i3} \tilde{P}_e^r. \end{aligned} \quad (2.49)$$

Substituting for  $d\tilde{T}_e/dt$  from (2.48) in (2.49), one finds

$$\begin{aligned} \frac{d\tilde{T}_e^p}{dt} = & (-k_{i3} \bar{T}_e) \tilde{\omega}_r + \left( -\frac{k_{p3} k_s}{J_r} \bar{T}_e \right) \tilde{\gamma} + \left( \frac{k_{p3} \bar{T}_e}{J_r} + \frac{k_{p3} \bar{\omega}_r}{\tau_i} - k_{i3} \bar{\omega}_r \right) \tilde{T}_e \\ & + \left( -\frac{k_{p3}}{\tau_i} \bar{\omega}_r \right) \tilde{T}_e^p + \left( -\frac{k_{p3} k_d}{\tau_i} \bar{\omega}_r \right) \tilde{\omega}_{rf} + k_{p3} \frac{d\tilde{P}_e^r}{dt} + k_{i3} \tilde{P}_e^r. \end{aligned} \quad (2.50)$$

Expressing (2.31) in the small-signal frequency-domain form, one obtains

$$\frac{d^2 \tilde{\omega}_{rf}}{dt^2} = -\frac{\omega_c}{Q} \frac{d\tilde{\omega}_{rf}}{dt} - \omega_c^2 \tilde{\omega}_{rf} + \frac{d^2 \tilde{\omega}_r}{dt^2}. \quad (2.51)$$

Differentiating (2.6) with respect to time, eliminating  $d\gamma/dt$  between the result and (2.7), and expressing the result in the small-signal form, one deduces

$$\frac{d^2 \tilde{\omega}_r}{dt^2} = \frac{k_s}{J_r} (\tilde{\omega}_t - \tilde{\omega}_r) - \frac{1}{J_r} \frac{d\tilde{T}_e}{dt}. \quad (2.52)$$

Substituting for  $d\tilde{T}_e/dt$  from (2.48) in (2.52), one finds

$$\frac{d^2 \tilde{\omega}_r}{dt^2} = \frac{k_s}{J_r} (\tilde{\omega}_t - \tilde{\omega}_r) - \frac{1}{J_r} \left( \frac{1}{\tau_i} \tilde{T}_e^p - \frac{1}{\tau_i} \tilde{T}_e + \frac{k_d}{\tau_i} \tilde{\omega}_{rf} \right). \quad (2.53)$$

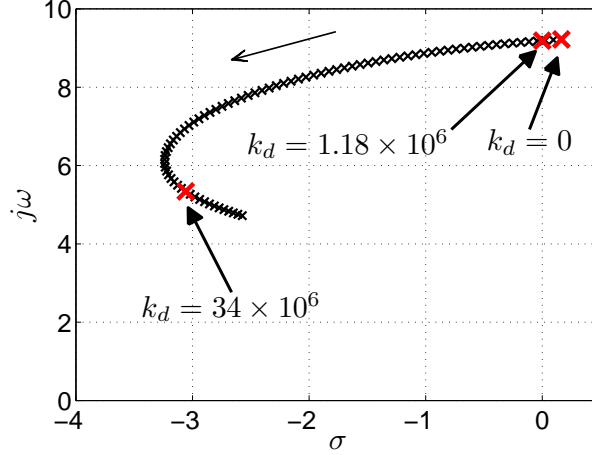


Figure 2.11: Migration plot of the (initially) unstable eigenvalues in the CP mode for different values of  $k_d$ .

Eliminating  $d^2 \tilde{\omega}_r / dt^2$  between (2.51) and (2.53), one concludes that

$$\begin{aligned} \frac{d^2 \tilde{\omega}_{rf}}{dt^2} &= \left( \frac{k_s}{J_r} \right) \tilde{\omega}_t - \left( \frac{k_s}{J_r} \right) \tilde{\omega}_r + \left( \frac{1}{J_r \tau_i} \right) \tilde{T}_e \\ &- \left( \frac{1}{J_r \tau_i} \right) \tilde{T}_e^p - \left( \omega_c^2 + \frac{k_d}{J_r \tau_i} \right) \tilde{\omega}_{rf} - \frac{\omega_c}{Q} \frac{d\tilde{\omega}_{rf}}{dt}. \end{aligned} \quad (2.54)$$

Equations (2.48), (2.50), (2.54), and the small-signal versions of (2.5) through (2.7) constitute a small-signal state-space model for the energy capture subsystem augmented with the presented damping scheme. Replacing  $\tilde{P}_e^r$  and  $d\tilde{P}_e^r/dt$  in the state-space model by their expressions corresponding to each mode of operation, i.e., based on  $P_e^r = k_{opt} \omega_r^3$  and  $P_e^r = P_{cmd}$  respectively for the MPPT and CP modes, the following linear state-space models are obtained:

$$\frac{d\tilde{\mathbf{X}}_d}{dt} = \mathbf{A}_3 \tilde{\mathbf{X}}_d + \mathbf{B}_3 \tilde{v}_w, \quad \text{for the MPPT mode} \quad (2.55)$$

$$\frac{d\tilde{\mathbf{X}}_d}{dt} = \mathbf{A}_4 \tilde{\mathbf{X}}_d + \mathbf{B}_4 \begin{bmatrix} \tilde{v}_w \\ \tilde{P}_{cmd} \\ \frac{d\tilde{P}_{cmd}}{dt} \end{bmatrix}, \quad \text{for the CP mode} \quad (2.56)$$

where  $\tilde{\mathbf{X}}_d = [\tilde{\omega}_t, \tilde{\omega}_r, \tilde{\gamma}, \tilde{T}_e, \tilde{T}_e^p, \tilde{\omega}_{rf}, d\tilde{\omega}_{rf}/dt]^T$ ; the matrices  $\mathbf{A}_3$ ,  $\mathbf{A}_4$ ,  $\mathbf{B}_3$ , and  $\mathbf{B}_4$  are introduced in Appendix B.

For the example WECS, Figure 2.11 plots the migration of the (initially) unstable complex-conjugate eigenvalues in the CP mode, when the damping mechanism is enabled

Table 2.2: Eigenvalues of the Energy Capture Subsystem with the Damping Scheme.

MPPT Mode	CP Mode
-96.78	-101
-12.57	-8.2
$-2.9 \pm 4.28j$	$-3.06 \pm 5.34j$
-0.36	$-0.32 \pm 0.36j$
$-0.35 \pm 0.53j$	-0.17

and  $k_d$  is varied from zero to  $40 \times 10^6$ . The migration plot is sketched for the operating point that corresponds to  $v_w = 9$  m/s and  $P_e^r = P_{cmd} = 0.75P_{opt}$ . It is observed that the eigenvalues, which are unstable for  $k_d = 0$ , migrate towards the left-half plane as  $k_d$  is increased, but move back towards the imaginary axis once  $k_d$  surpasses a certain value. This behavior indicates the existence of an optimum value for  $k_d$ . The optimum value is computed such that the complex-conjugate eigenvalues possess the maximum damping ratio. This, for the example WECS, corresponds to the choice of  $k_d = 34 \times 10^6$  which results in the smallest angle between the real axis and the tangent to the migration plot. Also are marked on Figure 2.11 the locations of the eigenvalues for the gain  $k_d = 1.18 \times 10^6$  which places the eigenvalues right on the imaginary axis of the s-plane.

Table 2.2 reports the eigenvalues of the energy capture subsystem under the MPPT and CP modes of operation, for  $k_d = 34 \times 10^6$  and the operating point corresponding to  $v_w = 9$  m/s; for the CP mode,  $P_e^r = P_{cmd} = 0.75P_{opt}$ . As the table indicates, in both modes of operation, the energy capture subsystem has one negative real eigenvalue relatively far from imaginary axis, two more negative real eigenvalues, and two pairs of complex-conjugate eigenvalues, where the pair of complex-conjugate eigenvalues with the lower imaginary part represents the dynamic effects of the augmented high-pass filter. A comparison to the results reported in Table 2.1 confirms the improved damping of the complex-conjugate eigenvalues with higher damped natural frequency, under the presented damping scheme. More important, the damping scheme has stabilized the system in the CP mode, as all the eigenvalues lie in the left-half plane.

For the example WECS, Figure 2.12 plots the migration of the two eigenvalues with the oscillatory modes, in the CP mode of operation, for  $k_d = 34 \times 10^6$  and different values of the ratio  $P_{cmd}/P_{opt}$  for every given wind speed (similar to Figure 2.9), when the wind speed is varied from 6 m/s to 12 m/s. It is observed that some eigenvalues approach the imaginary axis as the wind speed increases. Nonetheless, the system remains stable over

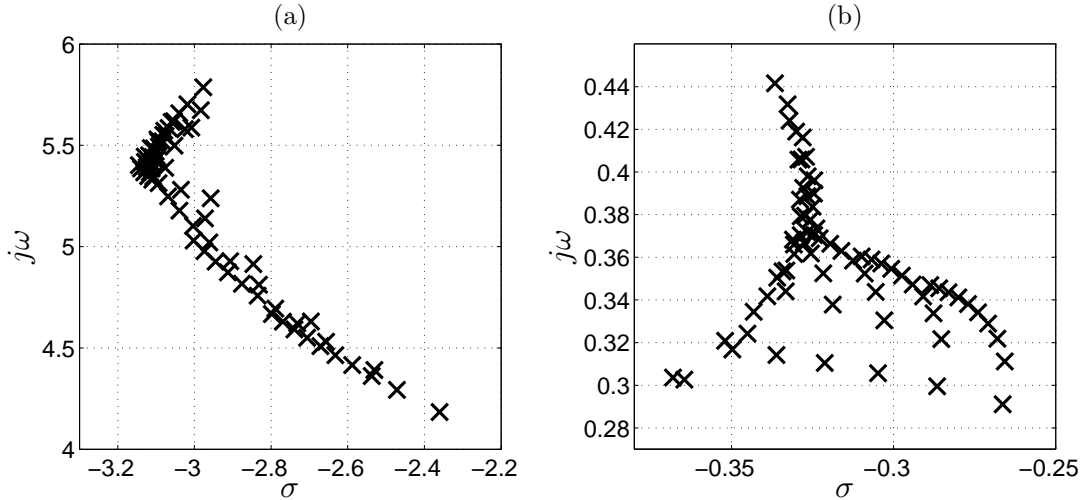


Figure 2.12: Migration plot of the eigenvalues for different operating points.

the entire wind speed range, and the eigenmodes are well damped.

To verify the accuracy of the developed mathematical model, the response of  $\omega_r$  to an abrupt switching from the MPPT mode to the CP mode, in which  $P_e^r = P_{cmd} = 0.75P_{opt}$ , is depicted in Figure 2.13. The response is obtained from a detailed switched model of the example WECS, developed in the PSCAD/EMTDC environment [90], for the gains  $k_d = 0$ ,  $k_d = 1.18 \times 10^6$ , and  $k_d = 34 \times 10^6$ . As Figure 2.13 shows, for  $k_d = 0$  the response is oscillatory and unstable, while  $k_d = 1.18 \times 10^6$  results in sustained oscillations. However, as expected,  $k_d = 34 \times 10^6$  results in a damped response. Figure 2.13 further indicates that the frequency of oscillations closely match those predicted by the eigenvalue analysis. For example, Figure 2.13(b) indicates that the period of oscillations for  $k_d = 1.18 \times 10^6$  is about 0.682 ( $=4.092/6$ ) s, which corresponds to an angular frequency of about 9.2 rad/s. This frequency is very close to that indicated by Figure 2.11 for  $k_d = 1.18 \times 10^6$ .

## 2.7 Case Studies

To further demonstrate the effectiveness of the proposed power control strategy, the detailed switched model of the example WECS has been subjected to various operating conditions based on the generally accepted criteria for the wind energy systems. In the graphs to follow, the angular velocities are expressed in rad/s, the torques are expressed in MNm, the powers are expressed in MW, the dc-link voltage is expressed in kV, and the pitch angle is expressed in degrees.

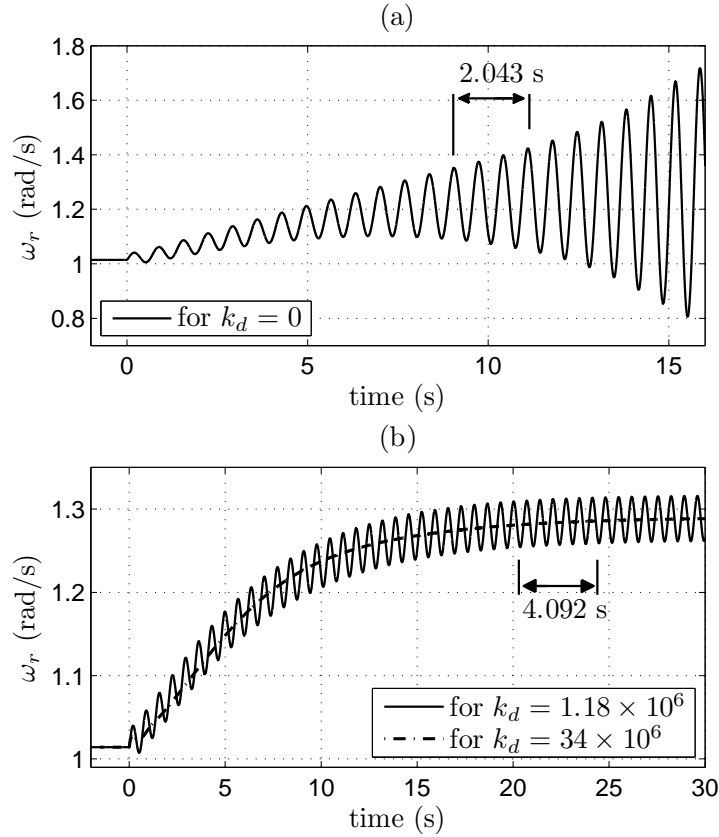


Figure 2.13: Response to operation mode change from MPPT to CP.

### 2.7.1 Start-up Process and Operation in the MPPT Mode

Figure 2.14 illustrates the performance of the example WECS in the MPPT mode of operation, subsequent to a start-up process. For this case,  $P_{cmd} = 6$  MW, and the wind speed is assumed to be 9 m/s from the start-up moment to  $t = 40$  s, 12 m/s from  $t = 40$  to 70 s, and 8 m/s from  $t = 70$  s onwards.

Initially, the turbine-generator set is in a standstill mode in which the mechanical brakes are engaged, the blade pitch angle is at the maximum value of  $90^\circ$  to reduce the aerodynamic torque of the turbine to almost zero, and the gating pulses of both VSC1 and VSC2 are blocked. Once it is recognized that the wind speed is sufficient for startup, that is,  $t = 0$  s in Figure 2.14, the WECS is connected to the grid via the start-up resistors and, therefore, the dc-link capacitor is charged by the antiparallel diodes of the VSC2 valves to a voltage of about 3.1 kV. At  $t = 3$  s, the startup resistors are bypassed and the gating pulses of the converter VSC2 are released and, thus, the controlled dc-voltage power port starts to function. The dc-link voltage,  $v_{dc}$ , is raised gradually towards its

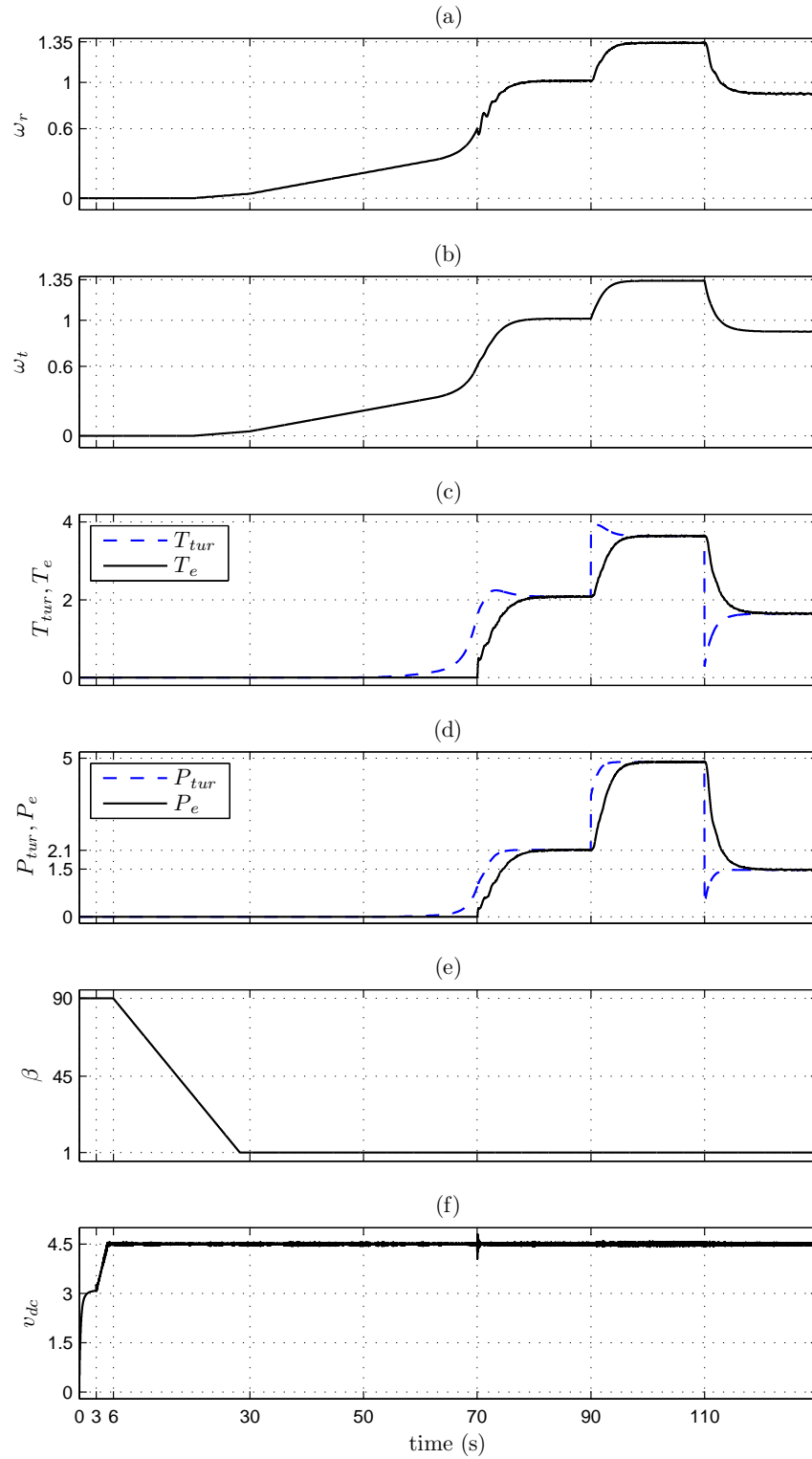


Figure 2.14: Start-up process and subsequent operation of the WECS in the MPPT mode.

final setpoint of 4.5 kV and is settled at  $t = 5$  s. At  $t = 6$  s, the mechanical brakes are released and the pitch angle of the blades is reduced from  $90^\circ$  to the minimum pitch of  $1^\circ$  to achieve sufficient aerodynamic torque of the turbine allowing the rotor to accelerate from rest. Once the rotor reaches an angular velocity of about 0.6 rad/s, the gating pulses of the converter VSC1 are also released and, thus, the energy capture subsystem starts to function. Therefore, the PMSG torque is permitted to rise to the value that is stipulated by the power control scheme [see Figures 2.3 and 2.7]. Thereafter, the WECS starts to generate power and its output settles at the maximum power for  $v_w = 9$  m/s, that is, about 2.1 MW.

Figure 2.14 also shows that, subsequent to each step change in the wind speed, the output power smoothly approaches the corresponding steady-state value. The steady-state value at each wind speed is equal to the maximum turbine power for that wind speed. For example, the wind speed of 12 m/s yields an output power of about 5 MW, at the rotor angular speed of about 1.35 rad/s; these values agree with the specifications mentioned in Appendix A, for the example WECS.

## 2.7.2 Response to Operation Mode and Wind Speed Changes

Figures 2.15 and 2.16 illustrate the WECS response to changes in the operating mode and wind speed. Before  $t = 0$  s,  $P_{cmd} = 6$  MW and the wind speed is assumed to be 9 m/s. In this case, the WECS is operating in the MPPT mode and the turbine yields the maximum power. The example WECS then experiences the following sequence of events: (1) at  $t = 0$  s,  $P_{cmd}$  is stepped from 6 MW down to 1.582 MW ( $0.75P_{opt}$ ) and, because the maximum power corresponding to  $v_w = 9$  m/s is about 2.1 MW, the operation mode is changed from the MPPT mode to the CP mode; (2) at  $t = 40$  s, the wind speed assumes a step change from 9 m/s to 12 m/s and thus the WECS remains in the CP mode; (3) at  $t = 80$  s,  $P_{cmd}$  is stepped further down to 0.5 MW and thus the WECS continues to operate in the CP mode; (4) at  $t = 110$  s, the wind speed changes stepwise from 12 m/s to 9 m/s. However, because the maximum power corresponding to  $v_w = 9$  m/s is larger than  $P_{cmd} = 0.5$  MW, the WECS retains its CP operating mode; (5) at  $t = 150$  s,  $P_{cmd}$  is stepped up to 3.5 MW. This command is larger than the maximum power for  $v_w = 9$  m/s, that is, 2.1 MW. Therefore, the WECS experiences a change from the CP mode to the MPPT mode and, as such, its output power settles at 2.1 MW; and (6) at  $t = 190$  s, the wind speed again rises stepwise from 9 m/s to 12 m/s and, because the maximum power corresponding to  $v_w = 12$  m/s (about 5 MW) is larger than  $P_{cmd} = 3.5$  MW, the

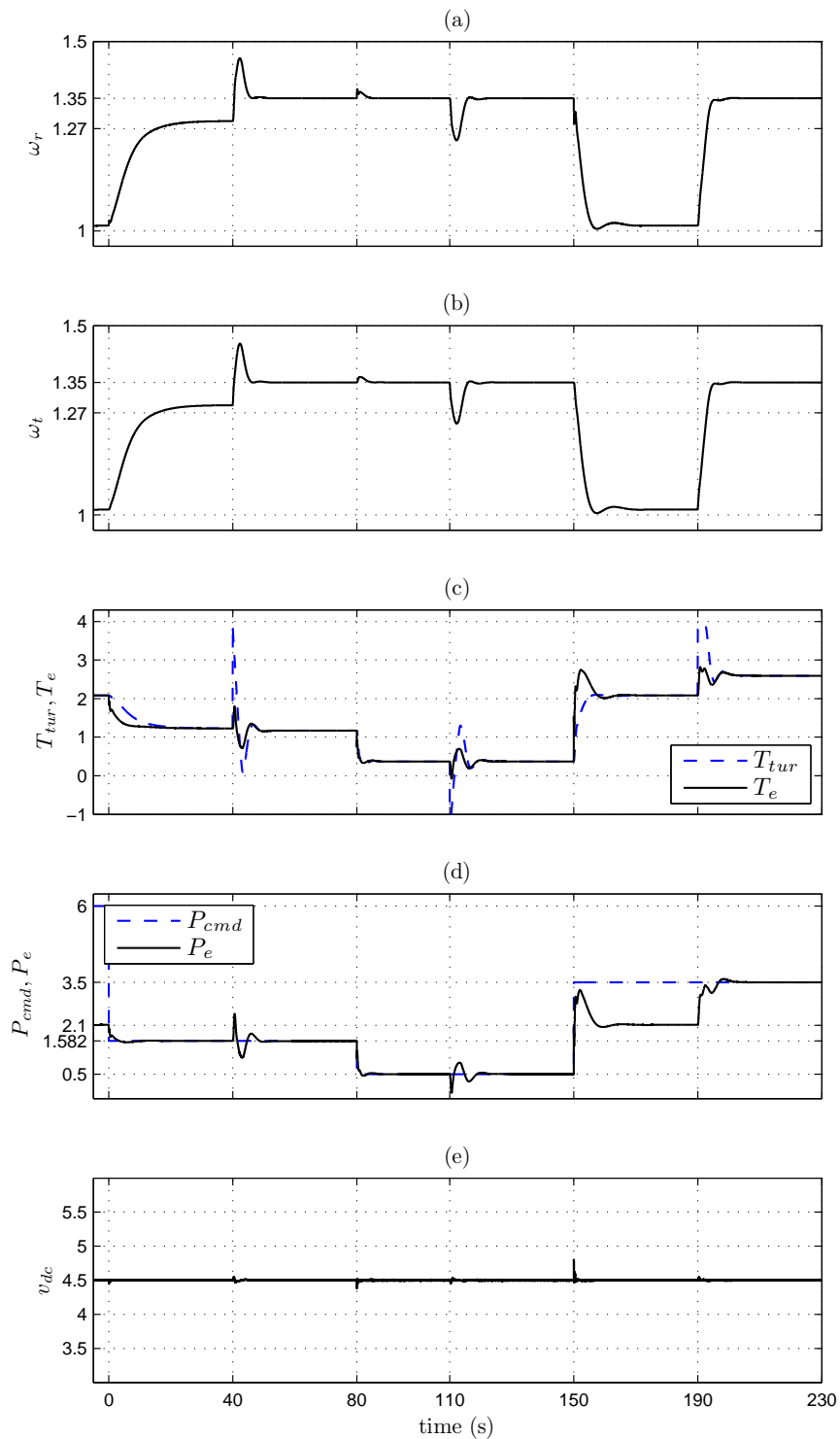


Figure 2.15: Response to changes in the operation mode and wind speed.

operating mode reverts back to the CP mode and the output power settles at 3.5 MW. It should be noted that real wind speed variations does not happen very fast and sharp



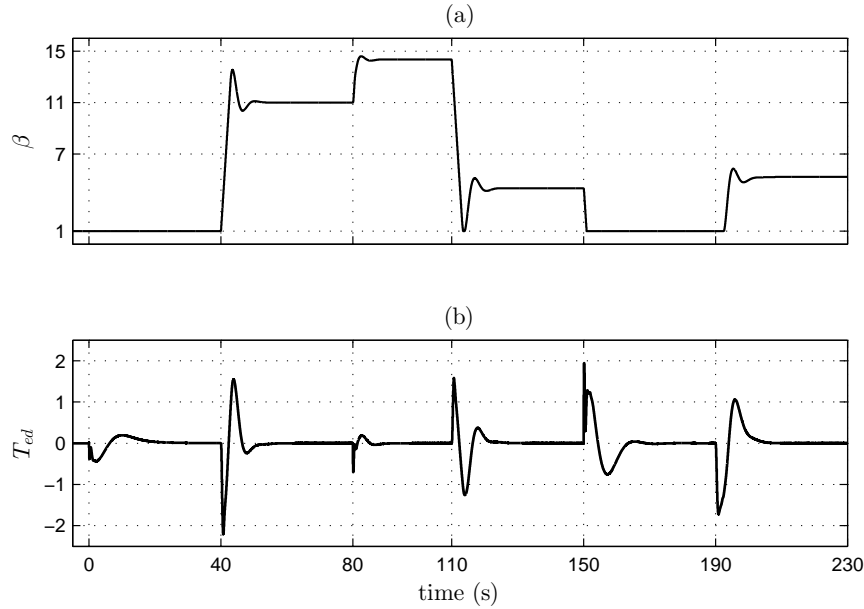


Figure 2.16: Response to changes in the operation mode and wind speed (cont.).

variations of the WECS output real power may not be required. However, in this section, the objective is to evaluate the performance of the example WECS in response to sharp wind speed and output real-power variations for the sake of analytical studies to assess the stability of the WECS.

Figure 2.15 shows that the output power rapidly tracks  $P_{cmd}$  during the periods when the WECS operates in the CP mode, that is, from  $t = 0$  to 150 s, and from  $t = 190$  s onwards. The figure also indicates that the rise and fall in the wind speed, respectively at  $t = 40$  s and 110 s, when the system is in the CP mode, result in transient excursions in the output power, but have no effects on the steady-state command following. It is interesting to note that at  $t = 150$  s when  $P_{cmd}$  is changed from 0.5 to 3.5 MW, the output power transiently overshoots, but reverts to its steady state value of 2.1 MW (that is, the maximum available power for the wind speed of 9 m/s). The reason for the overshoot is the stored kinetic energy of the rotor inertia, which is momentarily released.

Figure 2.16 shows the pitch angle waveform,  $\beta$  [Figure 2.16(a)], and the waveform of the supplementary component of PMSG torque setpoint,  $T_{ed}$  [Figure 2.16(b)]. It is observed that  $T_{ed}$  transiently responds to each disturbance, but settles down at zero. By contrast, the pitch angle only responds to those disturbances that cause the drive-train speed to exceed (and to be in need of regulation at) the maximum permissible value of 1.35 rad/s [see Figures 2.15(a) and (b)].

## 2.8 Summary and Conclusion

This chapter presented a simple real-power control strategy which is based on rapid control of the generator torque. The implementation of the proposed control was demonstrated for a direct-drive WECS that employs a PMSG. It was shown that the proposed strategy enables rapid control of the WECS output power, from small values up to the maximum power that corresponds to the prevailing wind conditions, but results in the instability of the drive-train torsional modes. Therefore, this chapter also presented a supplementary damping scheme and a procedure for tuning its parameters. The effectiveness of the proposed control strategy was demonstrated by mathematical analysis and time-domain simulation studies.

# Chapter 3

## An Alternative Control Structure and Damping Strategy

### 3.1 Introduction

The functions of the converters VSC1 and VSC2 in the direct-drive PMSG-based WECS introduced in Chapter 2 can be switched, as illustrated in Figure 3.1. Therefore, the converter VSC1 can be utilized to regulate the dc-link voltage by controlling the PMSG torque and, thus, by controlling the power that the PMSG extracts from the turbine,  $P_{tur}$ . By contrast, VSC2 controls the power that the WECS delivers to the grid,  $P_W$ . The advantage of this control scheme over the more common scheme described in Chapter 2 is that it mitigates the sensitivity of  $P_W$  to power fluctuations caused by wind speed variations and drive-train oscillatory modes. The pre-requisites, however, are that (1) the dc-link voltage remains to be large enough, such that VSC2 is not subjected to over-modulation, and (2) the current control of VSC2 is adequately fast, such that  $P_W$  does not respond to dc-link voltage fluctuations.

As mentioned in Chapter 1, a PMSG-based WECS inherently lacks the capability of damping drive-train torsional modes when its output real power is regulated and requires a supplementary damping mechanism. The damping strategies presented in [31], [67], [68], and Chapter 2 of this thesis utilize a filtering process to improve the damping of the modes corresponding to the soft drive-train, while they have a negligible impact on the other dynamic modes. Alternatively, reference [91] proposes to incorporate an unfiltered measure of the PMSG rotor speed into the control scheme of Figure 3.1, to eliminate the need for the filtering process. However, the proposed control impacts the other dynamic

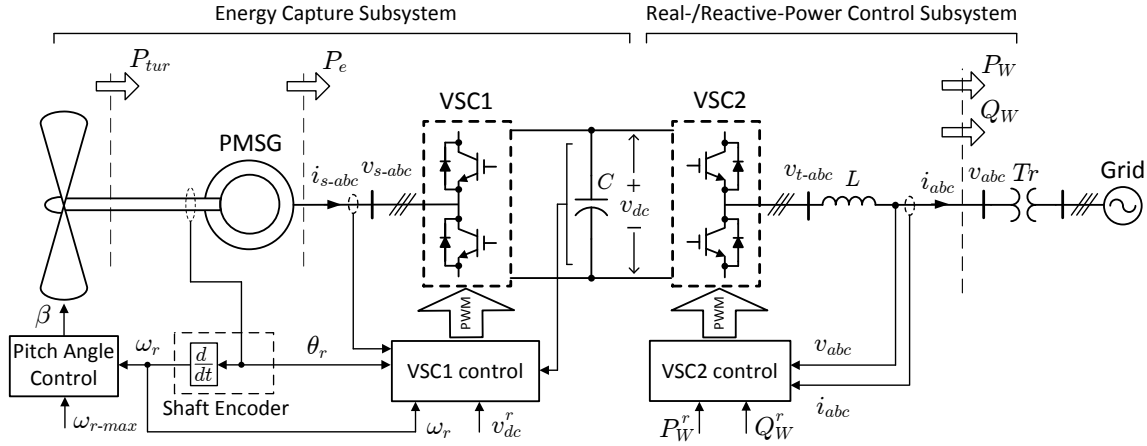


Figure 3.1: Schematic diagram of the alternative control strategy for the direct-drive PMSG-based WECS.

modes and can result in instabilities.

The conventional MPPT strategy employed by modern WECSs provides additional damping of drive-train torsional modes. Thus, capitalizing on this property, an enhanced control strategy is proposed in this chapter which enables a direct-drive PMSG-based WECS to damp oscillations and maintain internal stability, even if the output real power of the WECS is regulated. A procedure is also presented for tuning of the proposed control, based on the mathematical model of the WECS, such that a stable performance of the WECS over the operating range is ensured. In this chapter, the collection of the turbine, PMSG, VSC1 and its control, and dc-link capacitor  $C$  in Figure 3.1 is referred to as the *Energy Capture Subsystem*, whereas the composition of VSC2, the tie reactor, and the control scheme of the output real and reactive powers is identified as the *Real-/Reactive-Power Control Subsystem*.

## 3.2 Control Structure of the WECS

Figure 3.2 illustrates a control block diagram of the energy capture subsystem whose objective is to regulate the dc-link voltage,  $v_{dc}$ , at its setpoint  $v_{dc}^r$ , in spite of changes in the wind speed,  $v_w$ , and output power,  $P_W$  (which are considered as disturbances to the control system). The dc-link voltage compensator  $C_l(s)$  is assumed to be of the PI type. The details of the compensator tuning will be explained later in Sections 3.3.3 and 3.4. The PMSG is current-controlled by VSC1, such that the electrical torque,  $T_e$ , tracks its setpoint  $T_e^r$ , based on the first-order transfer function in (2.16), as explained in Section

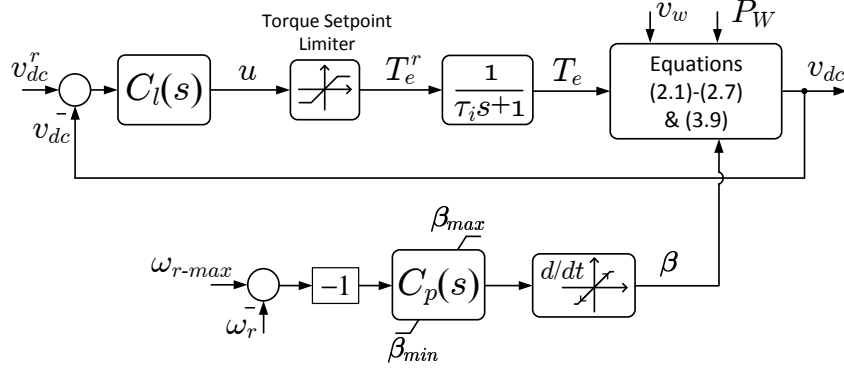


Figure 3.2: Block diagram of the dc-link voltage control scheme.

2.3.3. In turn,  $T_e^r$  is determined by passing the output of  $C_l(s)$  through a limiter. Figure 3.2 also illustrates the pitch-angle control process whose function is similar to the one described in Chapter 2, which is to ensure that the turbine and PMSG speeds do not exceed the maximum permissible value  $\omega_{r-max}$ . The pitch-angle compensator  $C_p(s)$  is also assumed to be of the PI type.

The WECS operates in either MPPT mode or CP mode, and the setpoint  $P_W^r$  in Figure 3.1 is stipulated by the same procedure as was shown in Figure 2.5. Hereafter, assuming a fast current control for VSC2, the output real power,  $P_W$ , and its setpoint  $P_W^r$  are used interchangeably. The numerical examples presented hereafter are based on an example WECS whose parameters are reported in Appendix A. The same example WECS is also simulated in time domain for producing the results reported in Section 3.5. Moreover, this chapter concentrates on the dynamics of the WECS drive-train in the CP mode of operation, due to the lack of a damping mechanism in this mode.

## 3.3 Basic WECS Control

### 3.3.1 Drive-Train Model

A two-mass model of the drive-train is adopted to capture the dynamics that affect stability and its representation is repeated in this chapter for convenience, as

$$J_t \frac{d\omega_t}{dt} = T_{tur} - k_s \gamma, \quad (3.1)$$

$$J_r \frac{d\omega_r}{dt} = k_s \gamma - T_e, \quad (3.2)$$

$$\frac{d\gamma}{dt} = \omega_t - \omega_r. \quad (3.3)$$

Linearizing (3.1) through (3.3), expressing the results in the frequency domain, and then eliminating  $\tilde{\omega}_t$  and  $\tilde{\gamma}$  from the equations, one finds

$$\tilde{\omega}_r = -\frac{J_t s^2 + k_1 s + k_s}{J_r J_t s^3 + J_r k_1 s^2 + J k_s s + k_1 k_s} \tilde{T}_e, \quad (3.4)$$

where “ $\sim$ ” denotes the small-signal perturbation of a variable,  $J = J_t + J_r$ , and  $k_1 \triangleq -\partial T_{tur}/\partial \omega_t$ , whose value depends on the operating point of the WECS and its expanded form is presented in Appendix B.

### 3.3.2 Control for Fast dc-Link Voltage Regulation

If compensator  $C_l(s)$  in Figure 3.2 is tuned for a fast dc-link regulation, then the PMSG electrical power,  $P_e$ , rapidly tracks the real power that is delivered to the grid,  $P_W$ . Thus, neglecting the power losses, and ignoring the electrical dynamics versus mechanical dynamics, the principle of power balance requires that

$$T_e \omega_r = P_W. \quad (3.5)$$

The small-signal form of (3.5) can be written as

$$\tilde{T}_e = -\frac{\overline{T}_e}{\overline{\omega}_r} \tilde{\omega}_r + \frac{1}{\overline{\omega}_r} \tilde{P}_W, \quad (3.6)$$

in which an overline denotes the steady-state value of a variable, and  $\overline{T}_e = \overline{P}_W/\overline{\omega}_r$ . Substituting for  $\tilde{T}_e$  from (3.6) into (3.4), and multiplying both sides of the resultant by  $\overline{\omega}_r$ , one finds

$$\tilde{\omega}_r = \frac{-(J_t s^2 + k_1 s + k_s)}{(J_r J_t \overline{\omega}_r) s^3 + (J_r k_1 \overline{\omega}_r - J_t \overline{T}_e) s^2 + (J k_s \overline{\omega}_r - k_1 \overline{T}_e) s + (k_s k_1 \overline{\omega}_r - k_s \overline{T}_e)} \tilde{P}_W. \quad (3.7)$$

Applying the Ruth-Hurwitz stability test to (3.7), one concludes that, assuming a fast dc-link voltage regulation, the WECS is stable if the constraint (3.8) is satisfied at all operating points.

$$(J_r k_1 \overline{\omega}_r - J_t \overline{T}_e) > 0. \quad (3.8)$$

For the example WECS, the poles of the transfer function from  $\tilde{P}_W$  to  $\tilde{\omega}_r$  have been calculated for an operating point that corresponds to  $v_w = 9$  m/s and  $P_W = 0.75 P_{opt}$ ,

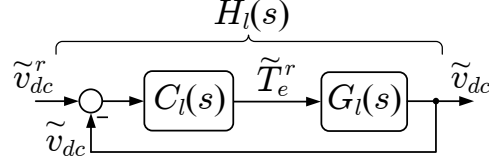


Figure 3.3: Control block diagram of the energy capture subsystem.

where  $P_{opt}$  is the maximum power that the WECS can generate at the prevailing wind speed. Hereafter, the same operating point is assumed for the example WECS in all the cases, unless otherwise noted. Thus, there exists a real pole at  $s = -0.19$  rad/s, which corresponds to the slow mechanical time constant of the WECS, due to the large overall inertia  $J_t + J_r$  of the drive-train. Moreover, an unstable pair of complex poles exist at  $s = 0.3 \pm 9.25j$  rad/s, due to the torsional modes of the drive-train. For this operating point, it can be verified that the constraint (3.8) is not satisfied and, consequently, the example WECS with a fast dc-link voltage regulation is unstable in the CP mode of operation; the instability is caused by the undamped torsional modes of the drive-train.

### 3.3.3 Control for Slow dc-Link Voltage Regulation

In contrast to the previous section, this section studies the stability of the WECS under the condition of a slow dc-link voltage regulation. Figure 3.3 shows the small-signal control block diagram of the energy capture subsystem, assuming an unsaturated control in Figure 3.2, and in which  $G_l(s)$  is the small-signal transfer function from the torque setpoint  $T_e^r$  to the dc-link voltage  $v_{dc}$ . Taking into account the dynamics of the dc-link voltage, the principle of power balance requires that

$$T_e \omega_r - P_W = \left( \frac{C}{2} \right) \frac{dv_{dc}^2}{dt}. \quad (3.9)$$

Linearizing (3.9) and expressing the result in frequency domain, one finds

$$\bar{T}_e \tilde{\omega}_r + \bar{\omega}_r \tilde{T}_e - \tilde{P}_W = C \bar{v}_{dc} s \tilde{v}_{dc}. \quad (3.10)$$

It is also understood from Figure 3.2 that

$$\tilde{T}_e = \frac{1}{\tau_i s + 1} \tilde{T}_e^r. \quad (3.11)$$

Substituting for  $\tilde{\omega}_r$  from (3.4) into (3.10), and then eliminating  $\tilde{T}_e$  between the resultant and (3.11), one finds the transfer function from  $\tilde{T}_e^r$  to  $\tilde{v}_{dc}$  [i.e.,  $G_l(s)$ ] as

$$G_l(s) = \frac{(J_t J_r \bar{\omega}_r) s^3 + (J_r k_1 \bar{\omega}_r - J_t \bar{T}_e) s^2 + (J k_s \bar{\omega}_r - k_1 \bar{T}_e) s + (k_s k_1 \bar{\omega}_r - k_s \bar{T}_e)}{C \bar{v}_{dc} s (J_r J_t s^3 + J_r k_1 s^2 + J k_s s + k_1 k_s) (\tau_i s + 1)}. \quad (3.12)$$

Finally, the small-signal closed-loop transfer function for the control loop of Figure 3.3 is

$$H_l(s) = \frac{C_l(s) G_l(s)}{1 + C_l(s) G_l(s)}, \quad (3.13)$$

where  $C_l(s)$  is a PI compensator and of the form

$$C_l(s) = k_c \frac{s + z}{s}, \quad (3.14)$$

in which  $k_c$  (in kNm/V) and  $z$  (in rad/s) are the compensator gain and zero, respectively.

Substituting for  $G_l(s)$  and  $C_l(s)$  from (3.12) and (3.14), respectively, into (3.13), one finds the expression for  $H_l(s)$  as

$$H_l(s) = \frac{\left( \begin{array}{l} (k_c J_t J_r \bar{\omega}_r) s^4 + (k_c z J_r J_t \bar{\omega}_r + k_c J_r k_1 \bar{\omega}_r - k_c J_t \bar{T}_e) s^3 \\ + (k_c z J_r k_1 \bar{\omega}_r - k_c z J_t \bar{T}_e + k_c J k_s \bar{\omega}_r - k_c k_1 \bar{T}_e) s^2 \\ + (k_c z J k_s \bar{\omega}_r - k_c z k_1 \bar{T}_e + k_c k_s k_1 \bar{\omega}_r - k_c k_s \bar{T}_e) s + (k_c z k_s k_1 \bar{\omega}_r - k_c z k_s \bar{T}_e) \end{array} \right)}{\left( \begin{array}{l} (C \bar{v}_{dc} J_r J_t \tau_i) s^6 + (C \bar{v}_{dc} J_r J_t + C \bar{v}_{dc} J_r k_1 \tau_i) s^5 + (C \bar{v}_{dc} J_r k_1 + C \bar{v}_{dc} J k_s \tau_i + k_c J_t J_r \bar{\omega}_r) s^4 \\ + (C \bar{v}_{dc} J k_s + C \bar{v}_{dc} k_1 k_s \tau_i + k_c z J_r J_t \bar{\omega}_r + k_c J_r k_1 \bar{\omega}_r - k_c J_t \bar{T}_e) s^3 \\ + (C \bar{v}_{dc} k_1 k_s + k_c z J_r k_1 \bar{\omega}_r - k_c z J_t \bar{T}_e + k_c J k_s \bar{\omega}_r - k_c k_1 \bar{T}_e) s^2 \\ + (k_c z J k_s \bar{\omega}_r - k_c z k_1 \bar{T}_e + k_c k_s k_1 \bar{\omega}_r - k_c k_s \bar{T}_e) s + (k_c z k_s k_1 \bar{\omega}_r - k_c z k_s \bar{T}_e) \end{array} \right)} \quad (3.15)$$

For the example WECS, the poles of (3.15) have been calculated for compensator parameters of  $z = 4$  and  $k_c = 1$ . Therefore, the energy capture subsystem has a negative real pole at  $s = -185$  rad/s, due to the time constant of the torque control loop [equation (3.11)], which can be ignored for its distance from the imaginary axis. The subsystem also has a negative real pole at  $s = -0.19$  rad/s, which is due to the large overall inertia of the drive-train. This pole, however, is fairly invariant to the compensator parameters and, therefore, is not considered in the following analysis either. By contrast, the subsystem has an unstable pair of complex poles at  $s = 0.25 \pm 9.06j$  rad/s, which are due to the torsional modes of the drive-train. Further, the subsystem has a pair of complex poles at  $s = -7.92 \pm 1.37j$  rad/s, which correspond to the electrical dynamics of the energy capture subsystem (these may alternatively appear as two negative real poles, depending



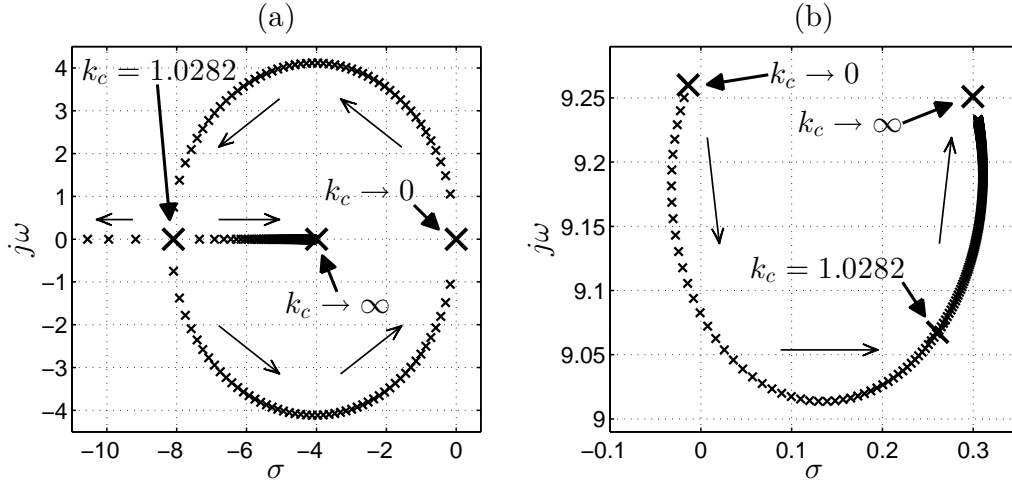


Figure 3.4: Migration plot of the closed-loop poles without damping mechanism; arrows illustrate increase in  $k_c$ .

on the compensator parameters and operating point of the WECS).

For the example WECS, Figure 3.4 plots the migration of the closed-loop poles of the energy capture subsystem, calculated from (3.15), for  $z = 4$ , if the compensator gain  $k_c$  is varied from 0.02 to 10, in steps of 0.02. Figure 3.4 also plots the closed-loop poles of the subsystem when  $k_c$  is decreased or increased respectively towards its lower or upper limit, i.e., zero and infinity. Figure 3.4(a) indicates the migration of the two poles that correspond to the electrical dynamics, whereas Figure 3.4(b) plots the migration of the pole that corresponds to the drive-train torsional mode (only the one with positive imaginary part out of the pair of complex poles has been mapped). Figure 3.4(a) shows that the poles migrate away from the imaginary axis as  $k_c$  is increased, but move back towards the imaginary axis once  $k_c$  surpasses a certain value,  $k_c = 1.0282$  for the example WECS. This value of  $k_c$  results in the maximum distance of the poles from the imaginary axis and, therefore, the fastest electrical dynamics of the subsystem. On the other hand, the pole in Figure 3.4(b) migrates towards the right-half plane as  $k_c$  is increased, thus, leading to a less stable drive-train torsional mode.

Figure 3.5 plots the migration of the closed-loop poles for four different values of the compensator parameter  $z$ . For each value of  $z$ ,  $k_c$  is varied from 0.02 to 10, in steps of 0.02. Figure 3.5(a) illustrates that as  $z$  is increased, the closed-loop poles in Figure 3.5(a) move further away from the imaginary axis and, therefore, the subsystem experiences faster electrical dynamics. Moreover, as Figure 3.5(b) indicates, a larger  $z$  results in better-damped torsional modes, if  $k_c$  is low; even though, the damping is

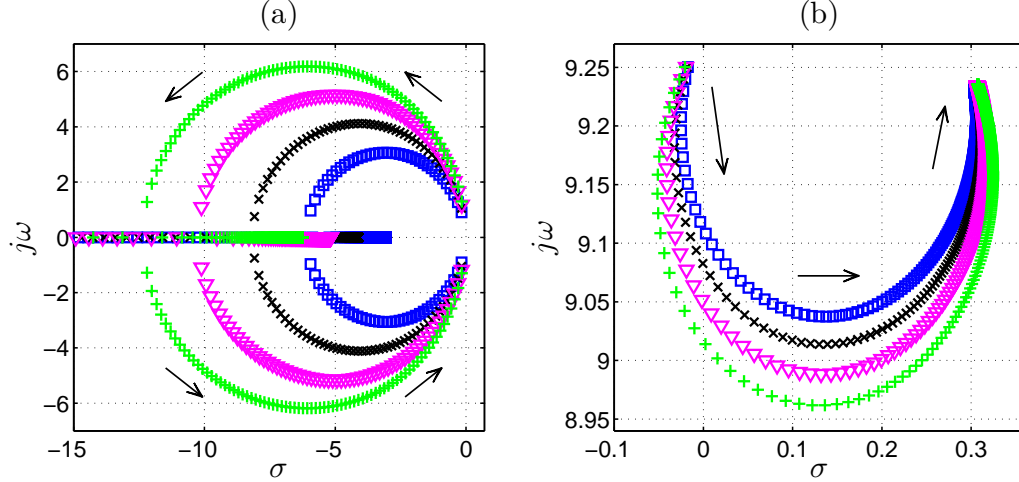


Figure 3.5: Migration plot of the closed-loop poles without damping mechanism;  $z = 3$  ( $\square$  trace),  $z = 4$  ( $\times$  trace),  $z = 5$  ( $\nabla$  trace), and  $z = 6$  ( $+$  trace); arrows illustrate increase in  $k_c$ .

poor. However, a lower  $k_c$  results in closed-loop poles that are closer to the imaginary axis, Figure 3.5(a), and, consequently, the electrical variables of the subsystem, e.g.,  $v_{dc}$ , experience larger overshoots (or undershoots) in their transient responses. Therefore, due to the aforementioned conflicting effects, the energy capture subsystem requires a damping mechanism.

## 3.4 Control Strategy to Damp the Drive-Train Torsional Modes

### 3.4.1 Proposed Control Strategy

To damp the drive-train torsional modes of the WECS in the CP mode of operation, the basic control of Section 3.3 is modified to the scheme of Figure 3.6 in which the PMSG torque setpoint is augmented by the following corrective signal:

$$T_{ed} = k_d k_{opt} \omega_r^2, \quad (3.16)$$

where  $k_d$  (unitless) is a constant parameter and referred in this chapter to as the *damping gain*; for  $k_d = 1$ ,  $T_{ed}$  is equal to the PMSG torque setpoint that results in the maximum power extraction from wind. It should be noted that, in the CP mode of operation, the steady-state PMSG torque is smaller than  $k_{opt} \omega_r^2$  and, thus, the output of the dc-link

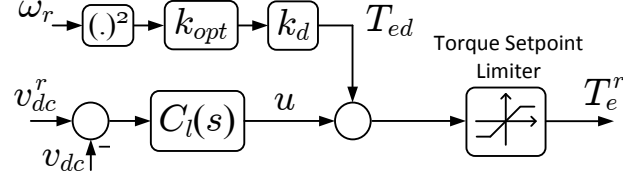


Figure 3.6: Block diagram illustrating the implementation of proposed control scheme.

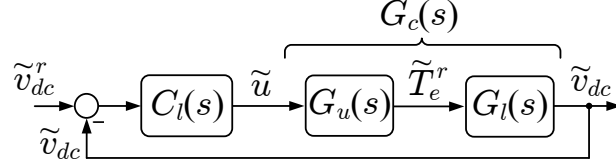


Figure 3.7: Control block diagram of energy capture subsystem with proposed control scheme.

voltage compensator,  $u$ , Figure 3.6, assumes a negative value.

Eliminating  $\tilde{T}_{ed}$  between the expression  $\tilde{T}_e^r = \tilde{u} + \tilde{T}_{ed}$  [see Figure 3.6] and the small-signal form of (3.16), one finds

$$\tilde{T}_e^r = \tilde{u} + k_d k_0 \tilde{\omega}_r, \quad (3.17)$$

where  $k_0 \triangleq 2k_{opt}\bar{\omega}_r$ . Substituting for  $\tilde{T}_e^r$  from (3.11) into (3.4), and then eliminating  $\tilde{\omega}_r$  between the resulting equation and (3.17), one deduces the transfer function from  $\tilde{u}$  to  $\tilde{T}_e^r$ , i.e.,  $G_u(s)$ , as

$$G_u(s) = \frac{(J_r J_t s^3 + J_r k_1 s^2 + J k_s s + k_1 k_s) (\tau_i s + 1)}{\left( (J_r J_t \tau_i) s^4 + (J_r J_t + J_r k_1 \tau_i) s^3 + (J_r k_1 + J k_s \tau_i + J_t k_d k_0) s^2 \right.} \quad (3.18)$$

$$\left. + (J k_s + k_1 k_s \tau_i + k_d k_0 k_1) s + (k_1 k_s + k_d k_0 k_s) \right)$$

Further, it follows from Figure 3.7 that the transfer function from  $\tilde{u}$  to  $\tilde{v}_{dc}$ , i.e.,  $G_c(s)$ , can be derived from the expression  $G_c(s) = G_u(s)G_l(s)$ , as

$$G_c(s) = \frac{J_t J_r \bar{\omega}_r s^3 + (J_r k_1 \bar{\omega}_r - J_t \bar{T}_e) s^2 + (J k_s \bar{\omega}_r - k_1 \bar{T}_e) s + (k_s k_1 \bar{\omega}_r - k_s \bar{T}_e)}{\left( C \bar{v}_{dc} s [(J_r J_t \tau_i) s^4 + (J_r J_t + J_r k_1 \tau_i) s^3 + (J_r k_1 + J k_s \tau_i + J_t k_d k_0) s^2] \right.} \quad (3.19)$$

$$\left. + (J k_s + k_1 k_s \tau_i + k_d k_0 k_1) s + (k_1 k_s + k_d k_0 k_s) \right)$$

In the following subsection, a procedure is presented for the tuning of the proposed control. The objective of the procedure is to tune the WECS control such that its stability is maintained, in the CP mode of operation, by damping the drive-train torsional modes,

while large transient dc-link voltage overshoots (or undershoots) are avoided.

### 3.4.2 Control Tuning Procedure

First, initial values are chosen for the compensator parameters of the energy capture subsystem with the basic control scheme. Then, the basic control of the subsystem is augmented by the proposed corrective signal and a value is selected for the damping gain. Further, final value of the compensator zero is chosen. Finally, a value is determined for the compensator gain in view of a trade-off between the damping of the torsional modes and speed of response of the subsystem electrical variables. In the following, the procedure is described in four steps.

#### 1) Initial Values of Compensator Parameters

Let us initially assume  $z = 4$ . Hence, as discussed in Section 3.3.3 for the energy capture subsystem with the basic control, one can find a value of  $k_c$  that results in the maximum distance of the closed-loop poles (corresponding to the electrical dynamics of the subsystem) from the imaginary axis. In the example WECS, for  $z = 4$ , the result is  $k_c = 1.0282$ , as shown in Figure 3.4(a).

#### 2) Damping Gain

In the example WECS, Figure 3.8 plots the migration of the closed-loop poles of the energy capture subsystem with the proposed control scheme for  $z = 4$ ,  $k_c = 1.0282$ , and the damping gain  $k_d$  varied from zero to 5, in steps of 0.02. Figure 3.8(a) indicates that one of the poles, that correspond to the electrical dynamics of the subsystem, moves towards the imaginary axis as  $k_d$  is increased. It is further observed that as  $k_d$  is increased, the closed-loop pole in Figure 3.8(b), that corresponds to the drive-train torsional mode, migrates towards the left-half plane but moves away from the imaginary axis once  $k_d$  surpasses a certain value,  $k_d = 1.1$  for the example WECS with given compensator parameters, as shown in Figure 3.8(b). This value of  $k_d$  results in the minimum distance of the pole (corresponding to the drive-train torsional mode) from the imaginary axis and, therefore, is chosen for the example WECS.

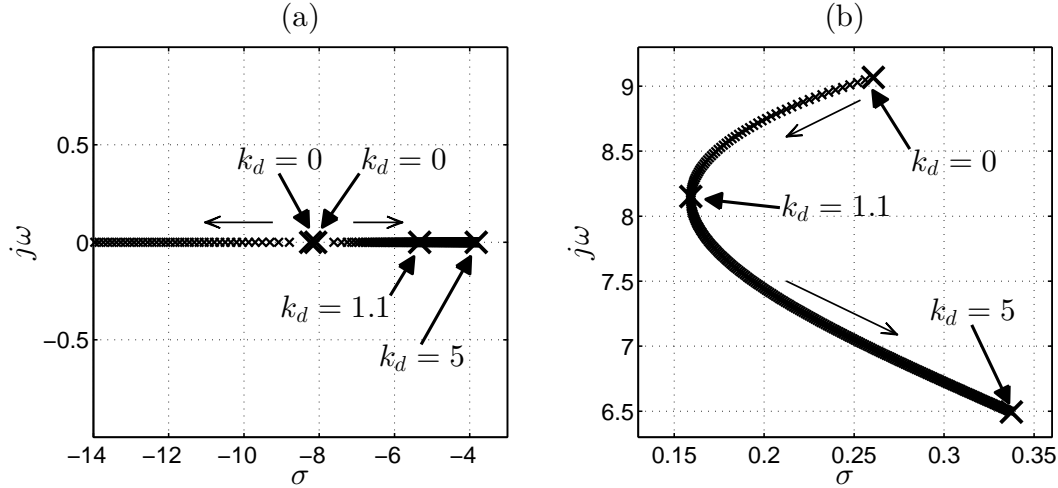


Figure 3.8: Migration plot of the closed-loop poles with the proposed control scheme; arrows illustrate increase in  $k_d$ .

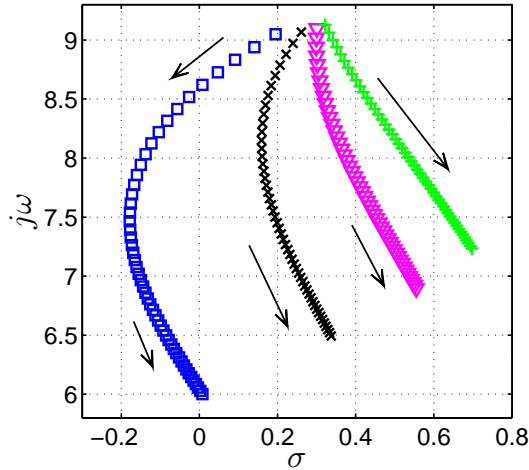


Figure 3.9: Migration plot of the closed-loop poles with the proposed control scheme;  $z = 3$  ( $\square$  trace),  $z = 4$  ( $\times$  trace),  $z = 5$  ( $\nabla$  trace), and  $z = 6$  ( $+$  trace); arrows illustrate increase in  $k_d$ .

### 3) Final Compensator Zero

Steps (1) and (2) are repeated for four different initial values of  $z$ , and Figure 3.9 plots the migration of the closed-loop pole (with positive imaginary part) that corresponds to the drive-train torsional mode, when  $k_d$  is increased from zero to 5, in steps of 0.1, for a given  $z$ . It is observed from the figure that for  $z = 3$ , the closed-loop pole considerably moves towards the left-half plane as  $k_d$  is increased. By contrast, for  $z = 5$  and  $z = 6$ , the closed-loop pole no longer moves towards the left-half plane. On the other hand,  $z = 3$  results in slow electrical dynamics of the subsystem, as discussed in Section 3.3.3, and,

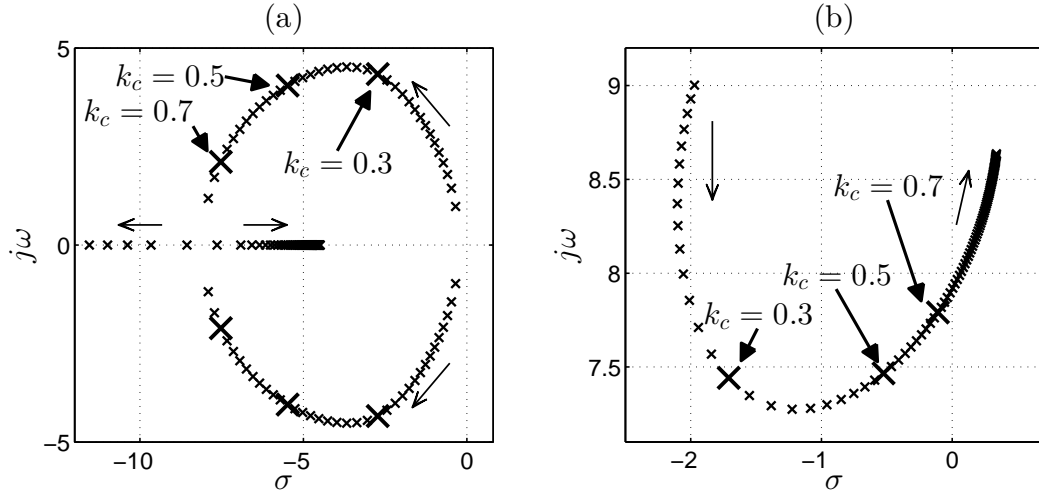


Figure 3.10: Migration plot of the closed-loop poles with the proposed control scheme; arrows illustrate increase in  $k_c$ .

consequently, larger transient dc-link voltage overshoots (or undershoots). Therefore, the compensator zero is finally chosen as  $z = 4$ , for the example WECS, to avoid a slow response of the dc-link voltage.

#### 4) Final Compensator Gain

For the example WECS, Figure 3.10 plots the migration of the closed-loop poles of the subsystem, for  $z = 4$ ,  $k_d = 1.1$ , and  $k_c$  varied from 0.02 to 2, in steps of 0.02. The figure also illustrates the closed-loop poles under three different compensator gains of  $k_c = 0.3$ ,  $k_c = 0.5$ , and  $k_c = 0.7$ . Figure 3.10 shows that as  $k_c$  is increased from 0.3 to 0.7, the closed-loop poles that correspond to the subsystem electrical dynamics migrate away from the imaginary axis [see Figure 3.10(a)], whereas the close-loop pole that corresponds to the drive-train torsional mode moves towards the imaginary axis [see Figure 3.10(b)]. Consequently,  $k_c = 0.3$  results in a subsystem with slower electrical dynamics, but better-damped torsional modes. By contrast, for  $k_c = 0.7$  the electrical variables of the subsystem experience faster transient responses with smaller overshoots (or undershoots), but the damping of the torsional modes is poor. Hence,  $k_c$  must be chosen in view of a trade-off between the damping of drive-train torsional modes and speed of response of the subsystem electrical variables.

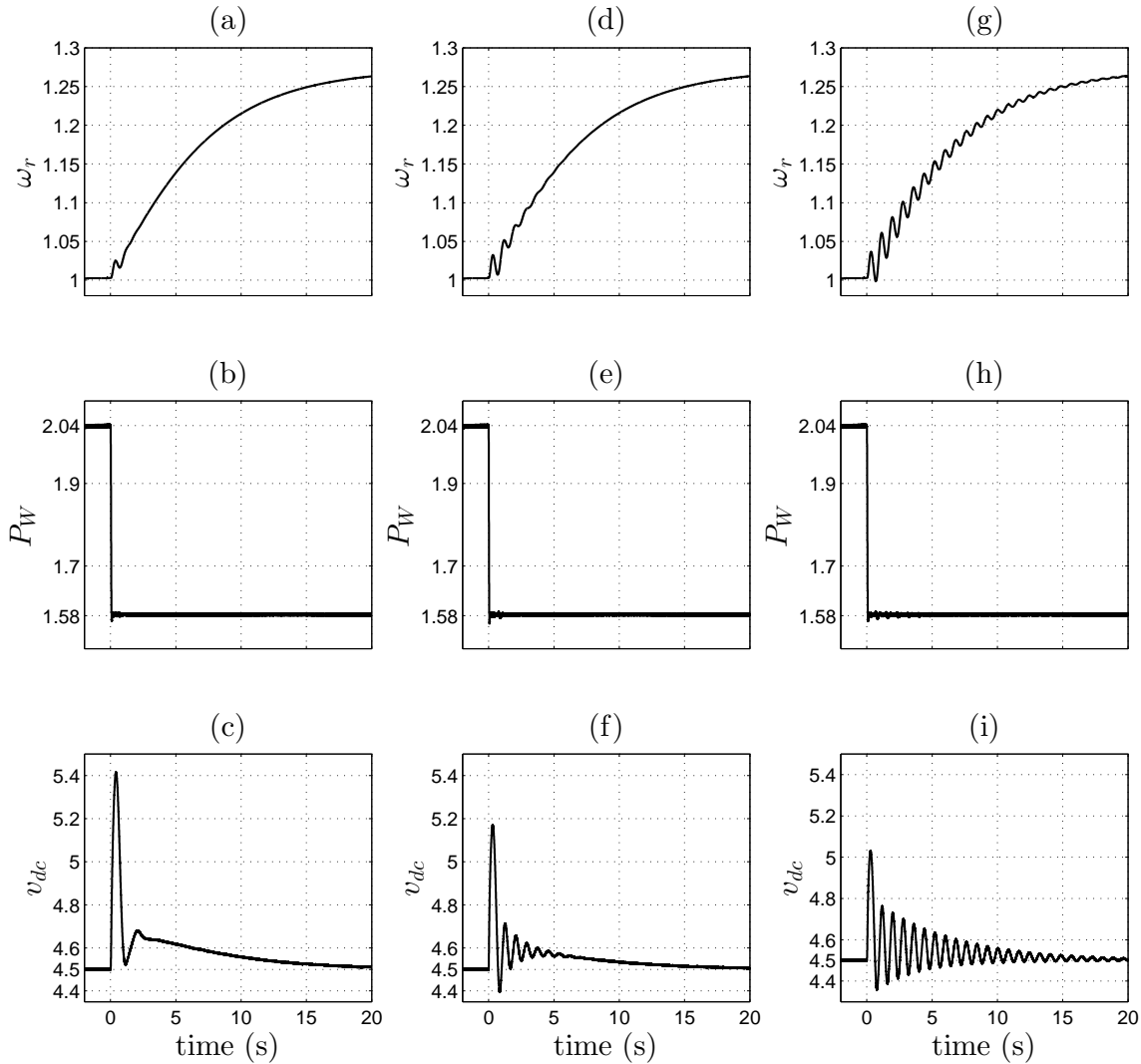


Figure 3.11: Response to a change from the MPPT mode to the CP mode.

### 3.4.3 Behavior of the WECS under Different Compensator Gains

Figure 3.11 depicts the responses of the example WECS to an abrupt switching from the MPPT mode to the CP mode of operation, when  $v_w = 9$  m/s and in the CP mode  $P_W^r = 0.75P_{opt}$ , for  $z = 4$ ,  $k_d = 1.1$ , and the three aforementioned compensator gains as:  $k_c = 0.3$  [Figures 3.11(a)-(c)],  $k_c = 0.5$  [Figures 3.11(d)-(f)], and  $k_c = 0.7$  [Figures 3.11(g)-(i)]. The responses are obtained from a detailed switched model of the example WECS in the PSCAD/EMTDC environment, whose parameters are reported in Appendix A. In the graphs, the angular velocities are expressed in rad/s, the powers are expressed in MW, and the dc-link voltages are expressed in kV. It is observed that, in all three cases, subsequent to the operation mode change to the CP mode, at  $t = 0$  s, the output power

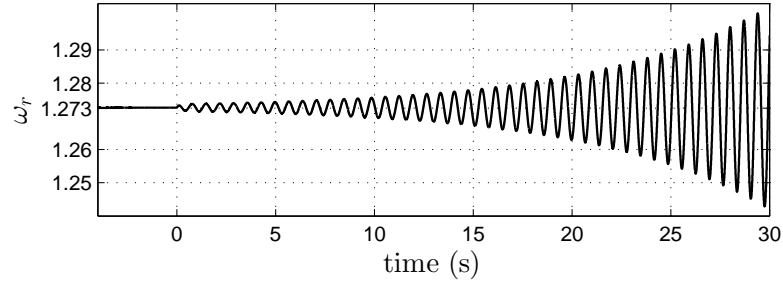


Figure 3.12: Response to a switch from the proposed control to the basic control.

rapidly tracks its setpoint, irrespective of the response of the energy capture subsystem. Further, the oscillations are damped in all three cases. As Figure 3.11(a) shows, the oscillations are rapidly damped for  $k_c = 0.3$ , while  $v_{dc}$  exhibits a large overshoot [see Figure 3.11(c)]. The overshoot of  $v_{dc}$  is significantly smaller for  $k_c = 0.7$  [see Figure 3.11(i)], but the damping is poor, and it takes several cycles until the oscillations are fully damped [see Figure 3.11(g)]. Therefore, a trade-off exists between the damping of drive-train oscillations and the overshoot of  $v_{dc}$ . For the example WECS,  $k_c = 0.5$  is chosen for the satisfactory damping and acceptably low overshoot of  $v_{dc}$ .

To demonstrate the instability of the WECS under the basic control in the CP mode of operation, a test is conducted and the response of  $\omega_r$  is illustrated in Figure 3.12. Thus, prior to  $t = 0$  s, the system is under the proposed control strategy and in a steady state corresponding to  $v_w = 9.0$  m/s,  $P_{out}^r = 0.75P_{opt}$ , and parameters  $z = 4.0$ ,  $k_c = 0.5$ , and  $k_d = 1.1$ . At  $t = 0$  s, the supplementary signal  $T_{ed}$  [Figure 3.6] is made frozen at its steady-state value. Thus, effectively, the control is switched from the proposed control of Figure 3.6 to the basic control of Figure 3.2. As Figure 3.12 shows,  $\omega_r$  starts to oscillate subsequent to the aforementioned change, and the oscillations grow to instability.

For the example WECS, Figure 3.13 plots the migration of the closed-loop poles of the energy capture subsystem that correspond to the electrical dynamic of the subsystem, Figure 3.13(a), and the drive-train torsional mode, Figure 3.13(b), for  $z = 4$ ,  $k_c = 0.5$ , and  $k_d = 1.1$ , and with the wind speed varied from 6 m/s to 12 m/s, in steps of 1 m/s. For each wind speed, four different output power setpoints  $P_W^r$  are applied:  $P_W^r = 0.99P_{opt}$ ,  $P_W^r = 0.75P_{opt}$ ,  $P_W^r = 0.50P_{opt}$ , and  $P_W^r = 0.25P_{opt}$ , where  $P_{opt}$  is the maximum available power at the given wind speed. It is observed that the closed-loop poles move towards the imaginary axis as the wind speed is increased. Nonetheless, the system remains stable over the entire wind speed range, and drive-train torsional modes are well damped.



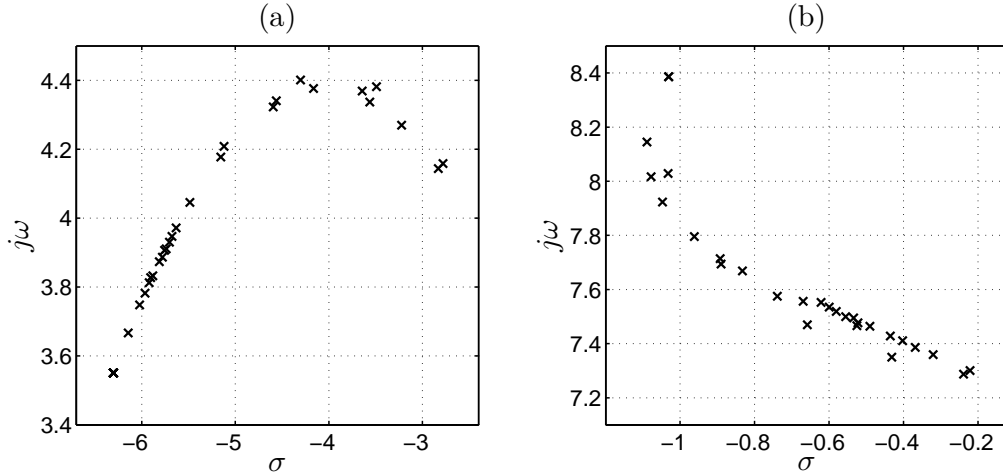


Figure 3.13: Migration plot of the closed-loop poles for different operating points.

### 3.5 Simulation Results

To further demonstrate the effectiveness of the proposed control strategy, the detailed switched model of the example WECS has been simulated and its response depicted in Figure 3.14. In the graphs, the torques are expressed in MNm, and the pitch angle is expressed in degrees. Initially, the example WECS operates in the MPPT mode, and is in a steady state, with a wind speed of 9 m/s. Then, it is subjected to following disturbances, similar to those in Section 2.7.2: (1) At  $t = 0$  s, the mode of operation is changed from the MPPT mode to the CP mode by reducing  $P_{cmd}$  from 6 MW down to 1.58 MW ( $0.75P_{opt}$ ); (2) at  $t = 40$  s, the wind speed assumes a step change from 9 m/s to 12 m/s and, thus, the WECS remains in the CP mode; (3) at  $t = 80$  s,  $P_{cmd}$  is stepped further down to 0.5 MW and, therefore, the WECS continues to operate in the CP mode; (4) at  $t = 110$  s, the wind speed changes stepwise from 12 m/s to 9 m/s. However, the maximum power available with  $v_w = 9$  m/s, i.e., about 2.1 MW, is larger than  $P_{cmd} = 0.5$  MW and, thus, the WECS retains its CP operating mode; (5) at  $t = 150$  s,  $P_{cmd}$  is stepped up to 3.5 MW. This power command is larger than the maximum power for  $v_w = 9$  m/s. Therefore, the WECS experiences a change from the CP mode to the MPPT mode and, as such, its output power settles at 2.1 MW; and (6) at  $t = 190$  s, the wind speed again rises stepwise from 9 m/s to 12 m/s. The maximum power corresponding to  $v_w = 12$  m/s (about 5.0 MW) is larger than the power command  $P_{cmd} = 3.5$  MW and, therefore, the operating mode reverts back to the CP mode and the output power settles at 3.5 MW.

Figure 3.14 shows that the output power rapidly tracks its setpoint when the WECS

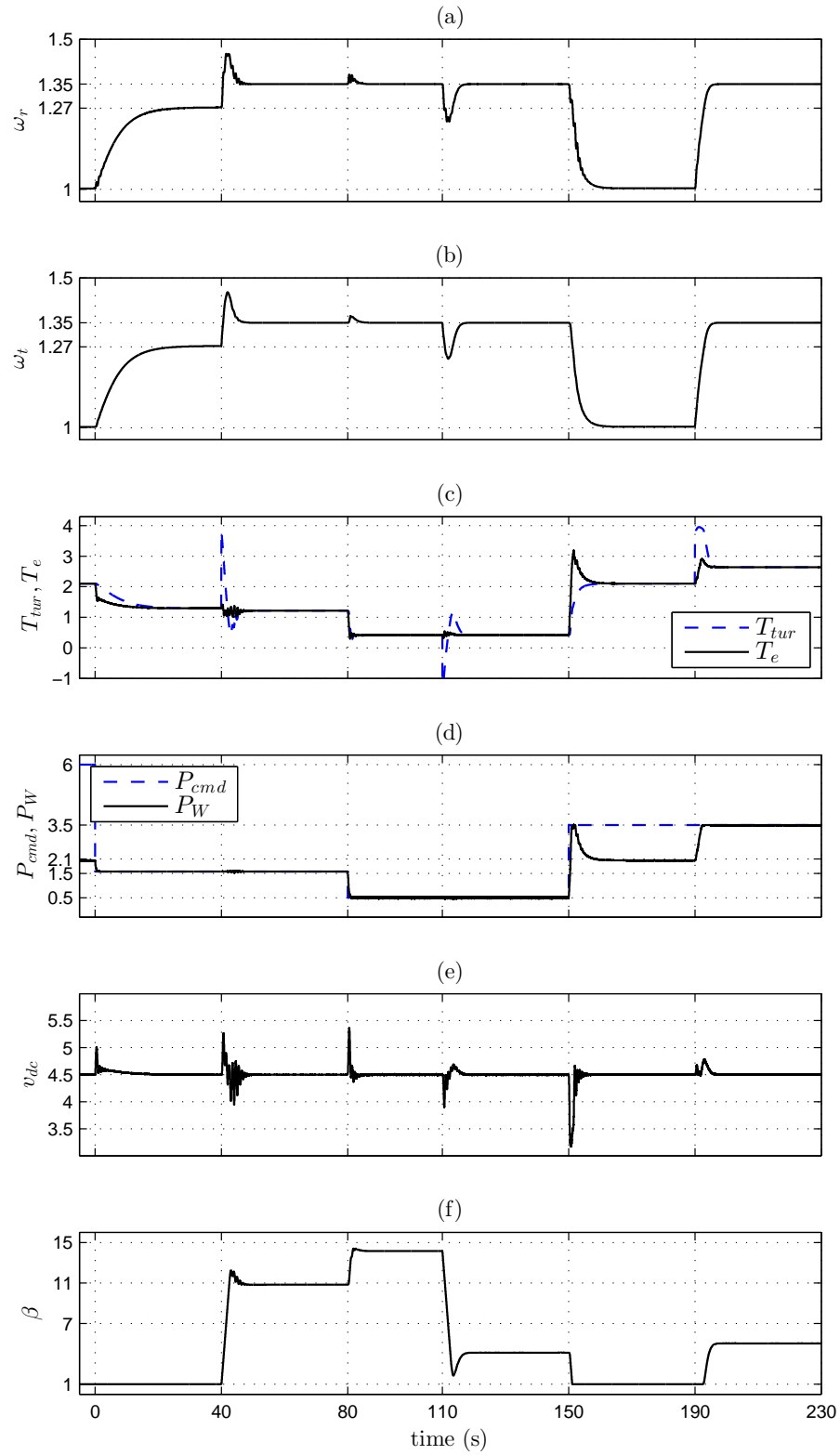


Figure 3.14: Response to changes in operation mode and wind speed.

operates in the CP mode, that is, from  $t = 0$  to 150 s, and from  $t = 190$  s onwards. Figure 3.14 also indicates that wind speed variations, at  $t = 40$  s and 110 s, do not influence the output power command following in the CP mode, but, rather, disturb the variables of the energy capture subsystem, such as  $T_e$  and  $v_{dc}$ .

## 3.6 A Comparative Discussion on the Presented Control Strategies

The performance of the control strategies presented in Chapter 2 and this chapter can be compared in two aspects. One aspect is the way the control tasks are distributed among the converters VSC1 and VSC2, and its impact on the WECS output power, and the other aspect is the effect of the damping mechanism used in each control strategy on different dynamic modes of the WECS. In the control scheme of Chapter 2 [Figure 2.1] the output power experiences transient excursions from its setpoint when the wind speed is changed [Figure 2.15(d)]. This is due to the augmentation of the damping signal into the power control loop. In contrast, the control scheme presented in this chapter [Figure 3.1] decouples the output power control loop from the dynamics of the energy capture subsystem and, thus, mitigates the sensitivity of the WECS output power to power fluctuations caused by wind speed variations and drive-train oscillatory modes [Figure 3.14(d)].

On the other hand, the damping mechanism presented in Chapter 2 more effectively damps the drive-train oscillations and has a negligible impact on the other dynamic modes of the energy capture subsystem. However, because a high-pass filtered measure of the rotor speed is used in the damping scheme, the effectiveness of the control is highly dependant on the filter parameters. In contrast, in the damping mechanism described in this chapter, the need for a high-pass filter measure of the rotor speed is eliminated. Although, the other dynamic modes are also affected by the damping strategy and, therefore, the control system has to be tuned based on a trade-off between the damping of drive-train torsional modes and speed of response of the dc-link voltage.

To test the performance of the PMSG-based WECS under a more realistic environment, Figure 3.15 illustrates the responses of the example WECS with the two presented strategies to a turbulent wind speed, when the output power command is changed similar to the case described in Section 3.5. As Figure 3.15 shows, the large-signal responses of the example WECS under the two aforementioned control strategies are more or less the

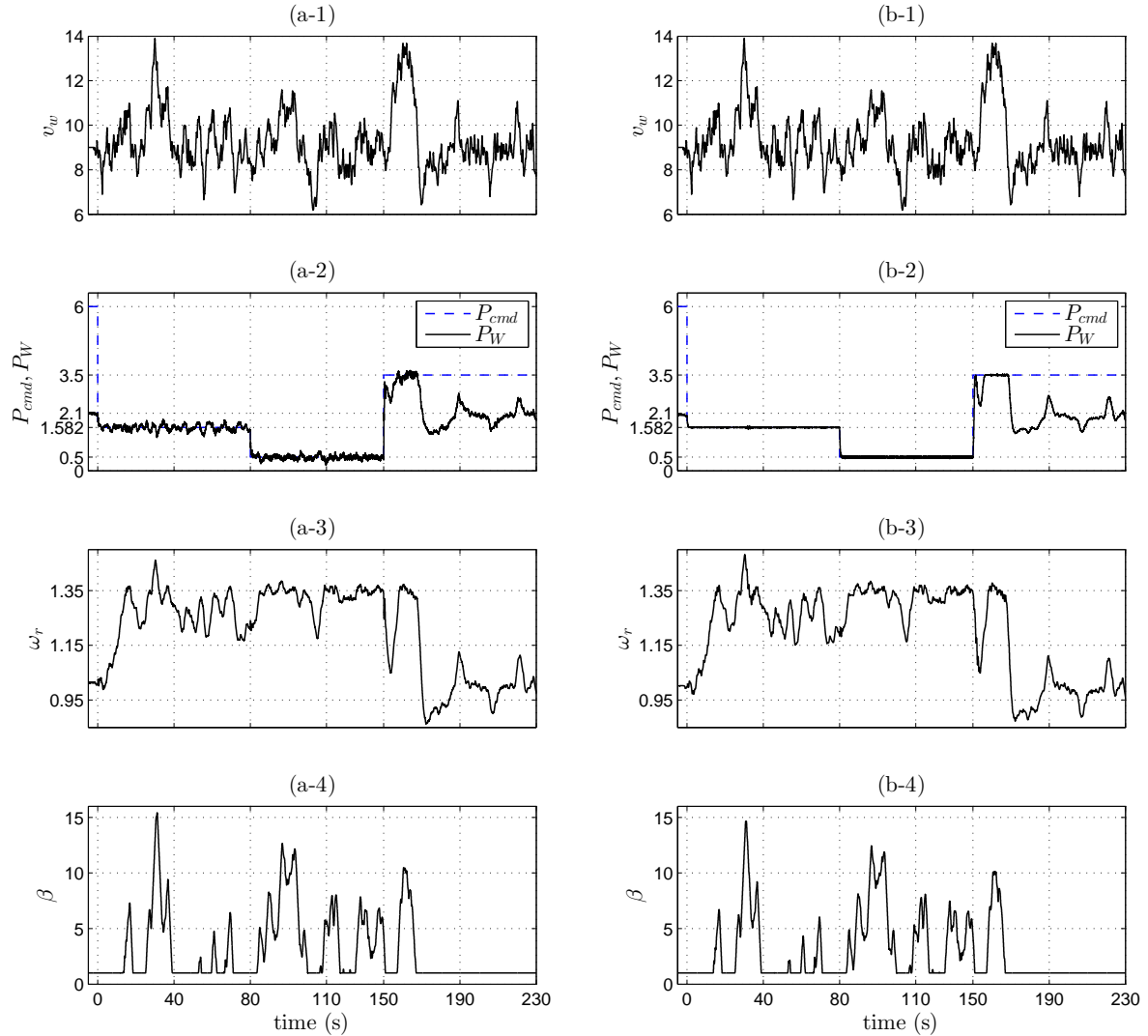


Figure 3.15: Responses to changes in power command under turbulent wind speed; (a) with the control strategy presented in Chapter 2, (b) with the control strategy presented in this chapter.

same. However, with the control strategy presented in Chapter 2, the output power  $P_W$  deviates from its setpoint, in the CP mode of operation. In contrast, with the control strategy presented in this chapter,  $P_W$  is tightly regulated at its setpoint in the CP mode of operation, irrespective of the wind speed condition and dynamics of the energy capture subsystem.

In conclusion, both control strategies can meet the required specifications of a modern WECS including the MPPT control, constant-power control and damping drive-train torsional modes. However, their dynamic responses are different, and, thus, one of the two strategies might be more suitable for an application that demands specific requirements,

such as the smoothness of the output power or a high level of damping due to a highly flexible drive-train.

### **3.7 Summary and Conclusion**

This chapter presented an enhanced control strategy that enables a direct-drive PMSG-based WECS to damp its drive-train torsional modes, even if the output real power of the WECS is regulated. A procedure was presented for tuning of the proposed control, such that the parameters were chosen in view of a trade-off between the damping of drive-train torsional modes and speed of response of the dc-link voltage. The effectiveness of the proposed control strategy was demonstrated by mathematical analysis and time-domain simulation studies. It was shown that the proposed strategy enables rapid control of the output real power, while the internal stability of the host WECS is preserved.

# Chapter 4

## Enhanced Control of WECSs for Contribution to Frequency Response

### 4.1 Introduction

As discussed in Chapter 1, the reduction of the overall inertia in highly wind penetrated power systems can have a wide range of impacts on the operational indices of the power system including ROCOF, system security, and cost of operation [92]. Therefore, WECSs are required to provide a reliable and repeatable inertial frequency response to support the grid and decrease the cost of generation reserve. Moreover, The ever-increasing penetration of wind power into the electric power system indicates that maintaining a generation reserve in WECSs to contribute to the frequency regulation process can become more valuable to a power system than maximizing wind generation. Consequently, evaluating the potential of WECSs in providing frequency response can be vital for modern power systems. It is important to distinguish between the grid integration requirements of WECSs and their actual requirements in system operation. For instance, limiting the output power of a WECS to provide a generation reserve results in the loss of energy, when it might be possible to obtain the generation reserve at less cost from other generation resources. However, the ability of WECSs to regulate their output real power can be essential in case of temporary grid contingencies.

In contrast to a CPP, a variable-speed WECS does not naturally provide frequency response. Therefore, suitable controls must be devised in a variable-speed WECS to offer this service. This chapter proposes an enhanced control strategy that enables a WECS to contribute to frequency regulation process, by effectively using its available

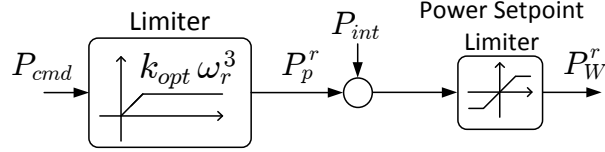


Figure 4.1: Block diagram illustrating the generation of the WECS output power setpoint.

generation reserve and the kinetic energy of its rotor, such that a stable performance of the WECS over the operating range is ensured. If the maximum available wind power, after the initial response of the WECS to a significant frequency change, falls behind the scheduled value for the WECS, the proposed control strategy allows a smooth mode transition of the WECS to the MPPT mode of operation, at steady state. A procedure is also presented in this chapter to adjust the parameters of the proposed control for WECSs to maintain the reliability of an example power system in response to a specific contingency event, under different wind speed regimes. In the following section, the proposed control strategy is described for a direct-drive PMSG-based WECS with a schematic diagram presented in Figure 3.1.

## 4.2 Control Strategy for Frequency Regulation

Figure 4.1 illustrates the proposed mechanism to stipulate the WECS output real-power setpoint,  $P_W^r$ . As Figure 4.1 shows, the setpoint  $P_W^r$  is obtained by passing the sum of two terms including (1) a hard limiter output,  $P_p^r$ , and (2) an inertia-emulating term,  $P_{int}$ , through a limiter. The input signal and upper saturation limit of the hard limiter are the command  $P_{cmd}$  and the value  $k_{opt} \omega_r^3$ , respectively (the lower saturation limit is zero), where  $\omega_r$  is the PMSG rotor speed, and  $k_{opt}$  is calculated as (2.19) for the optimum tip-speed ratio of the turbine and the minimum pitch angle, and is more or less constant over a relatively wide range of wind speeds. Thus,  $P_p^r$  equals  $P_{cmd}$ , as long as  $P_{cmd}$  is smaller than  $k_{opt} \omega_r^3$ ; otherwise,  $P_p^r$  is equal to  $k_{opt} \omega_r^3$  and the WECS operates in the MPPT mode, at steady state. Therefore, to operate the WECS in the MPPT mode at steady state, it is sufficient to set  $P_{cmd}$  to an adequately large value (e.g., larger than the maximum power that the WECS can deliver at the rated wind speed). In this chapter, assuming a fast output power control in the WECS, the output real power,  $P_W$ , and its setpoint  $P_W^r$  are used interchangeably.

To provide a droop-based control of the WECS output real power, the command  $P_{cmd}$

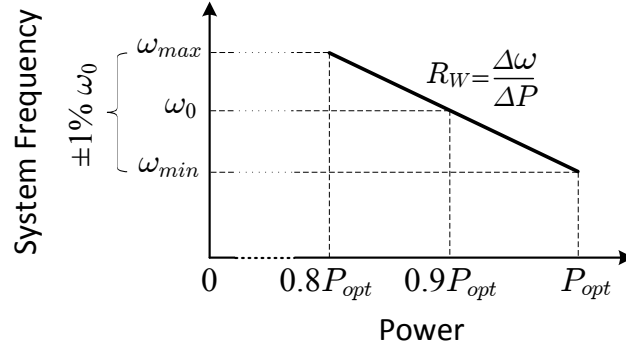


Figure 4.2: Droop characteristic of the WECS.

is determined from the following expression:

$$P_{cmd} = -\frac{1}{R_W}(\omega_0 - \omega) + P_{W0}, \quad (4.1)$$

where  $R_W$  (in rad/MWs) and  $P_{W0}$  (in MW) are constant parameters, and  $\omega_0$  and  $\omega$  are the rated and actual values of the power system angular frequency (in rad/s), respectively.

The term  $P_{int}$  is described as

$$P_{int} = \left( \frac{k_{int}D}{1 + \tau_d D} \right) \omega, \quad (4.2)$$

where  $D(\cdot)$  is the differentiation operator, and  $k_{int}$  (in MWs<sup>2</sup>/rad) and  $\tau_d$  (in s) are constant parameters. Therefore,  $P_{int}$  accepts values during transients when the system frequency is changing, and equals to zero at steady state.

### 4.2.1 Droop-Based Control

The droop-based control requires the WECS to reserve a generation capacity when the frequency of the power system is at its rated value. The droop characteristic shown in Figure 4.2 is assumed for a power reserve of 10% of the WECS maximum available power,  $P_{opt}$ , at the prevailing wind speed. First,  $P_{opt}$  is determined based on the measured or estimated value of the wind speed, for a specific period of time. Then, assuming the acceptable frequency deviation from the rated system frequency to be  $\pm 1\%$ , parameters  $R_W$  and  $P_{W0}$  are calculated based on the droop characteristic of Figure 4.2, and from equation (4.1).



### 4.2.2 Inertia-Emulating Control

An inertial frequency response is created artificially from the WECS by extracting the kinetic energy of its rotor and injecting it to the power system through the power-electronic converter. The objective is to emulate the response of a CPP, which is governed by the equation

$$\frac{1}{2p_G^2} J_G \frac{d(\omega^2)}{dt} = P_{mov} - P_G, \quad (4.3)$$

where the parameter  $J_G$  is the moment of inertia (in  $\text{kgm}^2$ ),  $p_G$  is the number of pole-pairs of the synchronous generator, and the variables  $P_{mov}$  and  $P_G$  respectively signify the actual input (prime mover) and output powers of the synchronous generator (in MW).

Let us assume that  $P_{mov}^r$  is determined based on the following droop characteristic:

$$P_{mov}^r = -\frac{1}{R_G}(\omega_0 - \omega) + P_{G0}, \quad (4.4)$$

where  $R_G$  (in  $\text{rad/MWs}$ ) and  $P_{G0}$  (in MW) are constant parameters. Let us further assume that the delay in the governor response is simply modeled as

$$P_{mov} = \frac{1}{\tau_m s + 1} P_{mov}^r. \quad (4.5)$$

Linearizing and combining (4.3), (4.4) and (4.5), one finds

$$\tilde{P}_G = \frac{1}{R_G} \left( \frac{1}{\tau_m s + 1} \right) \tilde{\omega} - \frac{J_G \omega_0}{p_G^2} \frac{d\tilde{\omega}}{dt}, \quad (4.6)$$

where “ $\tilde{\cdot}$ ” denotes the small-signal perturbation of a variable. Comparing (4.2) and (4.6), one concludes that the parameter  $k_{int}$  in (4.2) can be calculated as (4.7), in order for the WECS to offer the same inertial frequency response as an equivalent CPP.

$$k_{int} = -J_G \omega_0 / p_G^2. \quad (4.7)$$

In practice, direct differentiation of  $\omega$  is avoided [76], and  $d\omega/dt$  is approximated by a band-pass filter. The filtering process corresponds to the right-hand side term of (4.2), and whose high-frequency gain is limited by the time-constant  $\tau_d$ . Moreover,  $\tau_d$  decreases the rate of change of the output power setpoint which, in turn, reduces the impact of the inertia-emulating control on exciting the drive-train torsional modes. The value of this

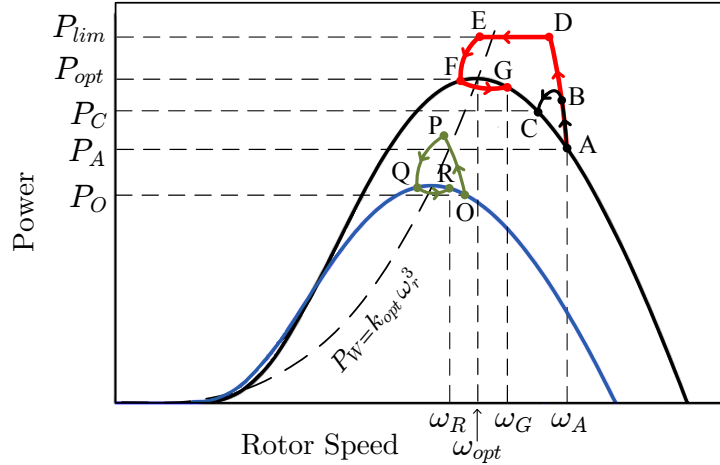


Figure 4.3: Characteristic curves of a wind turbine for two wind speeds.

parameter is selected as  $\tau_d = 0.1$  s.

### 4.2.3 Pitch-Angle Control

The function of the pitch-angle control is identical to the one presented in Chapters 2 and 3, which is to ensure that the WECS speed does not exceed the maximum permissible value,  $\omega_{r-max}$ . Maintaining the pitch angle at its lower value when  $\omega_r$  is smaller than  $\omega_{r-max}$ , while the output power is regulated at its setpoint  $P_W^r$  by the converter VSC2, results in a larger amount of stored kinetic energy in the WECS rotor and, thus, a more effective inertial response contribution of the WECS.

### 4.2.4 Description of the Proposed Control

In this section, the function of the proposed control strategy is described in more detail. Let us assume that the heavy solid line in Figure 4.3 illustrates the characteristic curve of a wind turbine for a given wind speed. Further, let us assume that the frequency of the host power system is, initially, equal to its rated value, and the control scheme of Figure 4.1 and the droop characteristic of Figure 4.2 are applied to a grid-connected WECS. In a steady state, the turbine mechanical power equals the WECS output power at point A on Figure 4.3, where  $P_W^r$  is equal to  $P_{cmd} = P_{W0}$ , at the prevailing wind speed [equation (4.1)]. Therefore, point A on Figure 4.3 is a stable operating point that corresponds to a 10% wind generation reserve in the WECS. If a loss of generation takes place in the power system, the resulting load-generation imbalance initiates a frequency drop. During the initial moments after the frequency deviates from its rated value, the droop-based term,

$P_{cmd}$ , does not change considerably. In contrast, the inertia-emulating term,  $P_{int}$ , rises rapidly due to its direct relation with the ROCOF [equation (4.2)] and, consequently,  $P_W^r$  increases.

Delivering  $P_W^r$  to the grid by extracting the kinetic energy of the WECS rotor results in the deceleration of the rotor speed. If the ROCOF declines to zero after a short period of time, then the term  $P_{int}$  decreases to zero correspondingly. Therefore, the operating point of the WECS moves along the power-speed route of ABC on Figure 4.3. To compensate for the loss of generation in the power system at the steady state, the output powers of the constituting power plants, including the example WECS, are increased based on their droop characteristics and, thus, after a transient response, the power system frequency stabilizes at a new value lower than the rated frequency. Hence, in the example WECS, the output power finally settles at  $P_C$  (which corresponds to point C on Figure 4.3). If the contingency event is more severe due to the loss of a larger amount of generation,  $P_W^r$  may increase further and reach the output power limit of the WECS,  $P_{lim}$ , which is, in turn, determined based on the capacity of the WECS generator and its power-electronic converter rating. This happened at point D on Figure 4.3. The kinetic energy extraction from the WECS rotor continues further along the power-speed route of DEF on Figure 4.3, until the rotor speed reaches a minimum value at point F. After this point, the output power becomes less than the turbine mechanical power (heavy solid line) and, thus, the rotor speeds up again along the power-speed route of FG and finally settles at the new steady state value  $\omega_G$  (which corresponds to point G on Figure 4.3). Because of a more severe contingency event in the later case, the steady state post-contingency output power of the WECS is larger than the one in the former case, to compensate for a larger loss of generation. Figure 4.3 also illustrates the characteristic curve of the example wind turbine for a lower wind speed (light solid line). Let us assume that point O is a stable operating point of the WECS, that corresponds to the given wind speed. After the loss of generation takes place in the power system, WECS delivers  $P_W^r$  in a similar procedure to the one discussed previously and the operating point of the WECS moves along the power-speed route of OPQR on Figure 4.3. However, in this case,  $P_W^r$  does not reach the output power limit of the WECS,  $P_{lim}$ .

Maintaining a 10% wind generation reserve enables the WECS to provide primary frequency response. Moreover, because of the operation of the WECS at a rotor speed higher than  $\omega_{opt}$  (which corresponds to  $P_{opt}$  on the turbine characteristic curve), larger amount of kinetic energy is available to be extracted from the WECS, if required. In the

proposed control scheme, the droop-based term,  $P_{cmd}$ , is not allowed to exceed  $k_{opt}\omega_r^3$ , which, at steady state, limits the WECS output power to the maximum available power,  $P_{opt}$ , at the prevailing wind speed. This ensures a stable performance of the WECS in the whole operating range. In contrast to  $P_{cmd}$ , the inertia-emulating term,  $P_{int}$ , is solely related to the ROCOF and, thus, the kinetic energy of the WECS is used at all operating points to provide an effective inertial frequency response.

It should be mentioned that, after the inertial and primary frequency responses of the constituting power plants stabilize the frequency of the power system at a new value lower (or higher, in case of a sudden loss of load) than the rated frequency, the CPP which is assigned to provide the secondary frequency response in the system is responsible for bringing the frequency back to its rated value. The secondary frequency response of the designated CPP is implemented by passing the frequency error through a slow integrator, whose output is added to the parameter  $P_{G0}$  [equation (4.4)] of its droop characteristic. The secondary response is slower than the inertial and primary responses and gradually brings the frequency back to its rated value. When the frequency settles at its rated value, the 10% wind generation reserve of the WECS is again available to contribute to frequency regulation for the next contingency event in the system.

### 4.3 Case Studies

To further demonstrate the effectiveness of the proposed control strategy, the example power systems shown in Figures 4.4(a) and (b) are simulated in the PSCAD/EMTDC environment. The example power system of Figure 4.4(a) consists of two conventional power plants, CPP1 and CPP2, a wind plant, and a constant power load,  $P_L$ , equal to 27 MW. CPP1 is assumed to have a maximum generation capacity of 22 MW and a 5% droop characteristic with the power setpoint of  $P_{G0-1} = 17.6$  MW, at the rated frequency. The rated frequency is assumed to be 60 Hz. CPP2 provides a constant output power equal to 4 MW and does not have a droop-based control. The CPPs are modeled based on their first-order mechanical equations. Moreover, a first-order delay is assumed, in each CPP, between the prime mover torque setpoint and the actual prime mover torque, to model the delay in the governor response. The example wind plant is assumed to have a rated generation capacity equal to 15 MW. The procedure to derive the switched model of the wind plant is explained in detail in Section 4.3.1.

The capacity factor of the wind plant is assumed to be equal to 40% of its rated

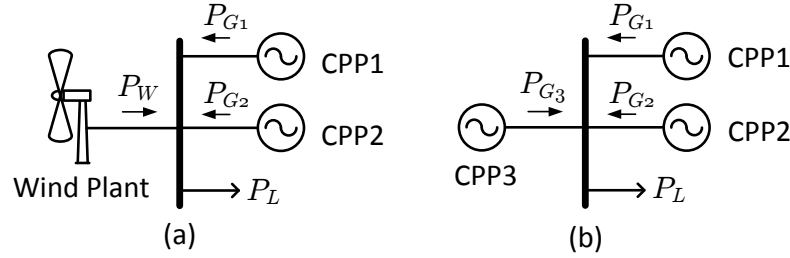


Figure 4.4: The example power systems.

generation capacity, which corresponds to the wind plant average available power of 6 MW. Hence, the wind speed of 8.85 m/s, at which the maximum available power of the wind plant is equal to 6 MW, is referred in this chapter to as the *average wind speed*. The wind speed is assumed to be constant, which is plausible by considering the length of each simulation time interval (several seconds). To provide primary frequency response, the wind plant output power is curtailed to 10% lower than the maximum available power, at the average wind speed. Therefore, at the average wind speed, 0.6 MW wind generation reserve is maintained and the wind plant delivers 5.4 MW to the grid and, thus, 20% of the load in the example power system of Figure 4.4(a) is supplied by the wind plant. Also, the acceptable range in which the frequency of the power system is allowed to deviate from its rated value is assumed to be  $\pm 1\%$  (i.e.,  $\pm 0.6$  Hz).

In the example power system of Figure 4.4(b), the wind plant is replaced by CPP3, which is assumed to have a maximum generation capacity of 6 MW and a 10% droop characteristic with the power setpoint of  $P_{G0-3} = 5.4$  MW. The example power systems have been subjected to various operating conditions as described next and their response to a sudden loss of generation is investigated. The specifications of the example wind plant and the CPPs are reported in Appendix C.

In this chapter, the primary focus is on the short-term responses of the example power systems to the loss of CPP2, which correspond to the inertial and primary frequency responses, and, therefore, the longer-term responses due to the secondary frequency response of CPP1 is not included in the graphs. It should be noted that in real power systems, the worst case contingency event is determined based on the loss of the largest power generation unit in the system. However, in this chapter, the loss of CPP2 in the example power systems is considered as the worst case contingency event, for the sake of analytical studies. In the graphs to follow, the power system frequency is expressed in Hz, the angular velocities are expressed in rad/s, and the powers are expressed in MW.

### 4.3.1 Switched Model of the Example Wind Plant

The example 15 MW wind plant in Figure 4.4(a) is assumed to be comprised of three 5 MW direct-drive PMSG-based WECSs. It is also assumed that the three constituting WECSs employ identical droop characteristics and are exposed to similar wind speed conditions. Therefore, under the aforementioned assumptions, the dynamic and steady-state responses of the constituting WECSs in the example wind plant, to disturbances, are expected to be identical. Hence, in order to provide a benchmark in the PSCAD/EMTDC environment in which the overall dynamic and steady-state performance of the example wind plant with the proposed control strategy can be simulated and analyzed, an aggregated switched model is developed for the example 15 MW wind plant. The aforementioned aggregated model is derived in this section based on the switched model of a constituting 5 MW WECS.

The 15 MW switched model is aimed to produce an output power equal to the total power that would be generated by the three constituting WECSs, if they were to be exposed to a given wind condition. Moreover, the 15 MW switched model should exhibit identical dynamic responses of the drive-train angular speed and dc-link voltage as compared to the ones in a constituting 5 MW switched model, when exposed to identical wind conditions. Thus, the switched model of the 15 MW wind plant possesses similar power structure and control scheme as the ones in a constituting 5 MW WECS. However, the values of the elements in the power circuit and the parameters of the control scheme in the switched model of a WECS are changed properly to derive a 15 MW switched model, such that:

1. The mechanical power of the turbine is three times larger in the 15 MW model as compared to the one in the 5 MW model, while the turbine and PMSG rotor speeds in the 15 MW and 5 MW models are the same. Therefore, the mechanical (and electrical) torque of the turbine is also three times larger in the 15 MW model as compared to the one in the 5 MW model
2. The turbine and PMSG moments of inertia are three times larger in the 15 MW model as compared to the ones in the 5 MW model.
3. The currents passing through the power circuit of the 15 MW model are three times larger as compared to the ones in the 5 MW model, while the voltages at several nodes across the power circuits of the 15 MW and 5 MW models remain the same.

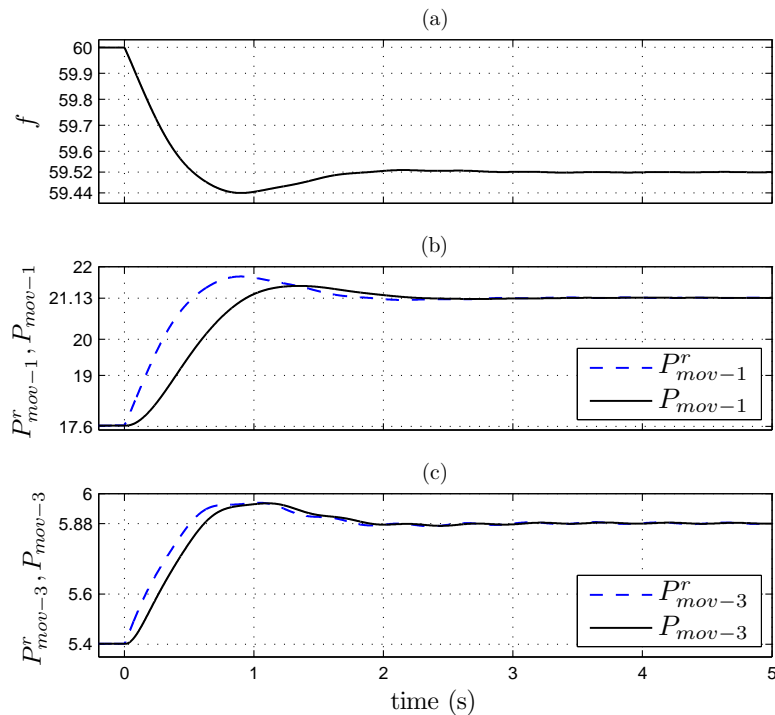


Figure 4.5: Response of the example power system, with only CPPs.

Therefore, the power that is transferred through the power circuit of the 15 MW model is three times larger as compared to the one in the 5 MW model.

4. The capacitance of the dc-link capacitor is three times larger in the 15 MW model as compared to the one in the 5 MW model.
5. The inductances and resistances are three times smaller in the 15 MW model as compared to the ones in the 5 MW model.
6. The parameters of the controllers in the control scheme of the 5 MW switched model are scaled properly to fit into the 15 MW model, based on the scale of their input and output variables.

The specifications of the example 15 MW wind plant in Figure 4.4(a) are listed in Appendix C.

### 4.3.2 Power System with Only CPPs

Figure 4.5 illustrates the response of the example power system in Figure 4.4(b) to a sudden loss of generation. The loss of generation is simulated by a sudden disconnection

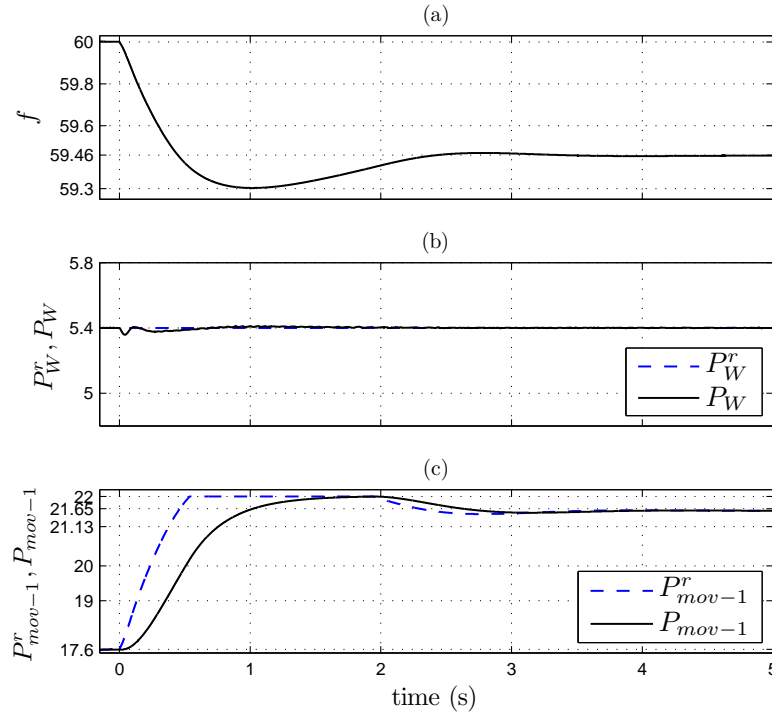


Figure 4.6: Response of the example power system, without frequency response from the wind plant.

of CPP2 from the rest of the power system, at time  $t = 0$  s. Consequently, right after the disconnection of CPP2, 15% of the generation is lost. The loss of CPP2 initiates a frequency drop, as shown in Figure 4.5(a). Figure 4.5(a) further indicates that the minimum and steady state frequencies are equal to 59.44 Hz and 59.52 Hz, respectively, which are both within the acceptable frequency range, i.e.,  $\pm 1\%$  of rated frequency. Figures 4.5(b) and (c) illustrate the setpoint and actual values of prime mover powers in CPP1 and CPP3, respectively. The figures show that the prime mover powers track their setpoints with the given time delays.

### 4.3.3 No Frequency Response from the Wind Plant

Figure 4.6 illustrates the response of the example power system in Figure 4.4(a) to the sudden loss of CPP2, when the wind plant does not provide any frequency response (which corresponds to  $P_{int} = 0$  and  $P_{cmd} = P_{W0}$  in Figure 4.1). Before  $t = 0$  s, wind speed is assumed to be 8.85 m/s (that corresponds to a maximum available power,  $P_{opt}$ , equal to 6 MW in the wind plant) and the output power setpoint of the wind plant is equal to 5.4 MW. Figure 4.6(a) indicates that the minimum frequency is 59.3 Hz, which is



outside the acceptable frequency range of  $\pm 1\%$ . The steady state frequency after the loss of CPP2 is equal to 59.46 Hz, which is within the acceptable range. However, the steady state frequency is less than the case with only CPPs, due to the lack of primary frequency response from the wind plant. Because the output power setpoint of the wind plant is fixed at 5.4 MW, the frequency drop has no impact on the wind plant output power setpoint,  $P_W^r$ , and it is maintained at 5.4 MW after a slight transient, as illustrated in Figure 4.6(b). Hence, CPP1 is required to compensate for the whole generation loss and maintain the stability of the system, which pushes CPP1 towards its maximum capacity, indicated in Figure 4.6(c).

#### 4.3.4 Frequency Regulation at the Average Wind Speed

Figure 4.7 illustrates the responses of the example power system in Figure 4.4(a) to the sudden loss of CPP2, when the wind plant provides (1) only inertial response [Figures 4.7(a)-(d)], (2) only primary response [Figures 4.7(e)-(h)], and (3) both inertial and primary responses [Figures 4.7(i)-(l)], based on the control scheme of Figure 4.1. The wind speed is assumed to be 8.85 m/s, which corresponds to  $P_{opt} = 6$  MW, and the output power setpoint of the wind plant is equal to 5.4 MW. The droop characteristic of Figure 4.2 is employed in modes (2) and (3) for primary response contribution, and  $P_{int} = 0$  in mode (2). Figure 4.7(a) indicates that in mode (1), the minimum frequency after the loss of CPP2 is equal to 59.38 Hz, which is outside the acceptable range of frequency for the example power system. Figure 4.7(b) shows that the wind plant actively contributes to the inertial frequency response, and the wind plant output power increases temporarily. This extra power is extracted from the kinetic energy of the wind plant rotor and, thus, the rotor speed drops, as illustrated in Figure 4.7(c). Before  $t = 0$  s, the wind plant is operating at a rotor speed higher than  $\omega_{opt}$  (1 rad/s, corresponding to  $v_w = 8.85$  m/s). Therefore, as the rotor speed declines, after the loss of CPP2, the turbine mechanical power increases based on the turbine characteristic curve, Figure 4.3. This, in turn, slows down the deceleration of the rotor speed when the wind plant provides inertial response.

Finally, the frequency settles at 59.46 Hz and the wind plant output power returns to its pre-contingency value, i.e., 5.4 MW. Consequently, the turbine mechanical power becomes larger than the output power and the rotor speed accelerates back to settle at its pre-contingency value, as shown in Figure 4.7(c). The figure further indicates that the torsional modes of the drive-train are well damped. It should be noted that because the maximum available power of the wind plant at the given wind speed of 8.85 m/s

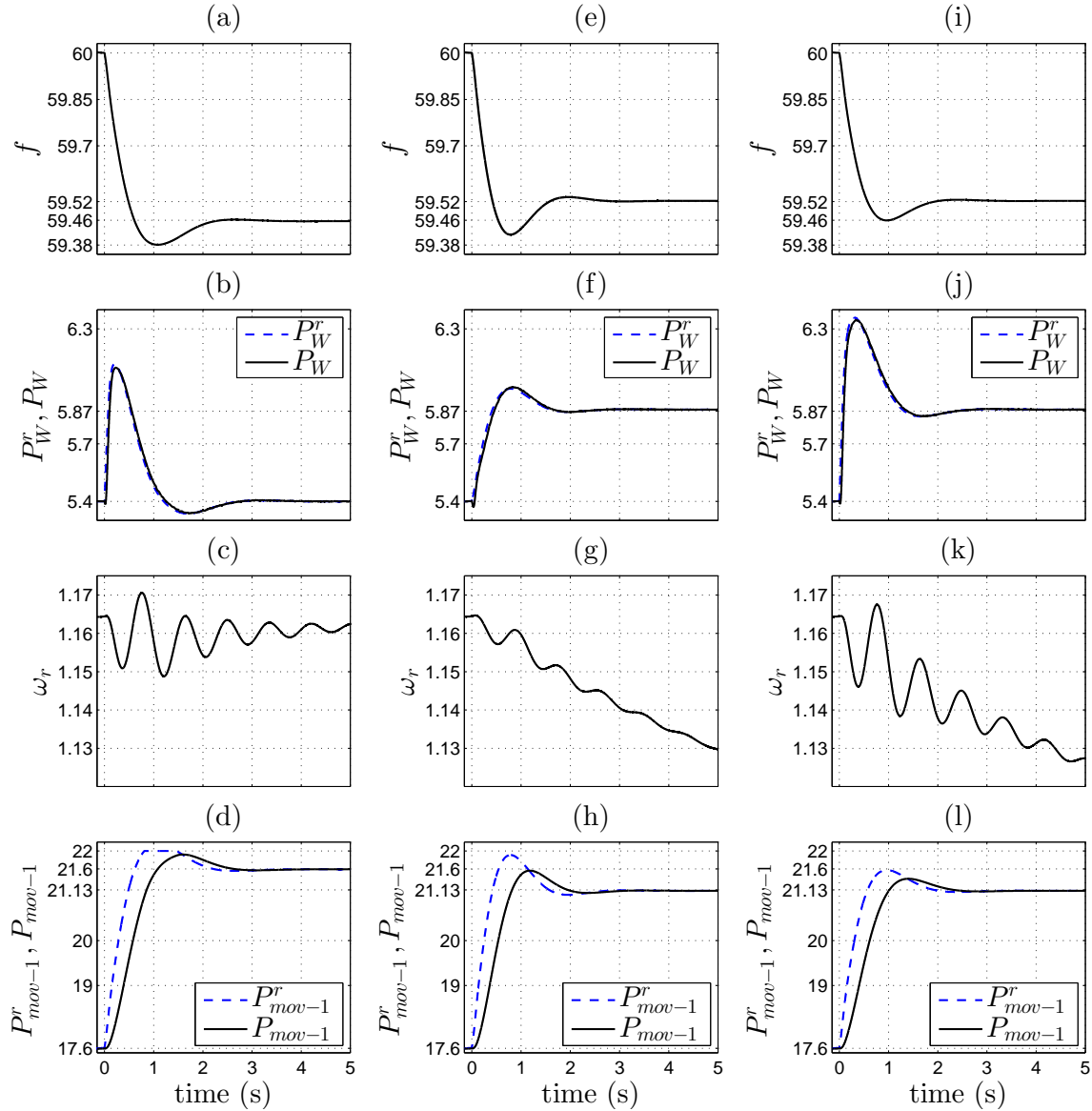


Figure 4.7: Response of the example power system, when the wind plant provides frequency response.

is more than 5.4 MW, the wind plant is able to recover the extracted kinetic energy from its rotor by using its available mechanical power. Therefore, the wind plant does not require to draw recovery power from the grid. Overall, in this mode, the minimum frequency is outside the acceptable range and CPP1 is required to compensate for the whole generation loss, at the steady state.

In mode (2), the steady state frequency after the loss of CPP2 is higher than the one in mode (1), as shown in Figure 4.7(e). This is due to the contribution of the wind plant in the primary frequency response based on its droop characteristic. Figure 4.7(f)

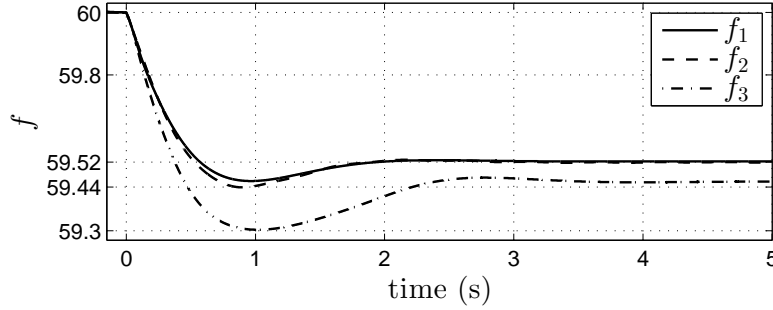


Figure 4.8: Frequency responses of the example power systems to the loss of CPP2.

indicates that the wind plant output power is increased to 5.87 MW, at steady state. The remaining of the 4 MW generation loss is compensated by CPP1 whose output power is increased to 21.13 MW, as shown in Figure 4.7(h). Because the wind plant does not provide any inertial response, the initial ROCOF after the loss of CPP2 is larger than the one in mode (1) and, thus, the frequency undershoot is higher in mode (2), 17%, with respect to the one in mode (1), 11%. Figure 4.7(f) also illustrates that the wind plant output power rapidly tracks its setpoint. As discussed in Subsection 4.2.4, the rotor speed declines [Figure 4.7(g)] until it reaches a new operating point at which the mechanical power is equal to the new output power setpoint. In mode (3), the steady state frequency, after the loss of CPP2, is identical to the one in mode (2). In addition, the inertial response results in an improvement in the ROCOF and, thus, the minimum frequency is also enhanced (frequency undershoot of 9%), as shown in Figure 4.7(i). Figure 4.7(k) indicates that the initial decline in the rotor speed is higher than the one in mode (2), due to the increased extraction of kinetic energy from the rotor.

Figure 4.8 illustrates the frequency responses of the example power systems in Figures 4.4(a) and (b), signified as  $f_1$  and  $f_2$ , respectively. The example wind plant is assumed to provide inertial and primary frequency responses, when  $v_w = 8.85$  m/s, and CPP3 is assumed to have the same generation capacity and droop characteristic as the example wind plant at the average wind speed. As Figure 4.8 indicates, the results show closely matching frequency responses in the two aforementioned cases. However, the minimum frequency in the response of  $f_1$  is slightly higher than the one in  $f_2$ . The reason is that although the wind plant and CPP3 have identical droop characteristics, the wind plant output power tracks its setpoint more rapidly than that in CPP3. This is due to the delay assumed between the setpoint and actual values of the prime mover torque (and, therefore, power) in the model of CPP3. Figure 4.8 further illustrates the frequency response

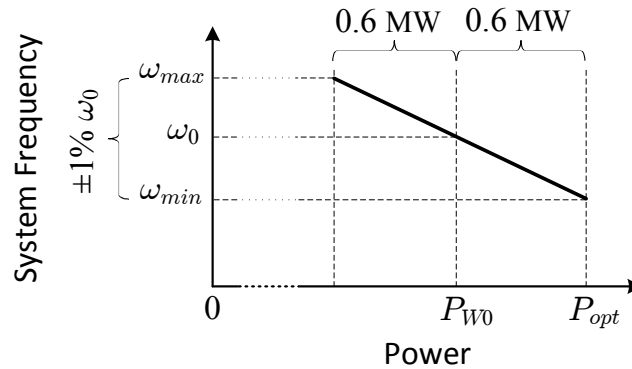


Figure 4.9: Proposed droop characteristic for the example wind plant.

of the example power system in Figure 4.4(a) when the wind plant does not contribute to frequency regulation process and simply maintains its pre-contingency output power after the loss of CPP2, signified as  $f_3$ . It is observed that, in this case, both minimum and steady state frequencies are considerably lower than the previous cases.

### 4.3.5 Frequency Regulation at Different Wind Speeds

A 10% wind generation reserve in the wind plant at the average wind speed ( $P_{opt} = 6$  MW) is equal to 0.6 MW. To maintain a wind generation reserve equal to 0.6 MW at all wind speeds, the droop characteristic shown in Figure 4.9 is proposed for the wind plant in the example power system of Figure 4.4(a), in which the variable  $P_{opt}$  corresponds to the maximum available wind power at the forecasted (or estimated) wind speed, for a specific period of time. Therefore, the parameter  $P_{W0}$  in the droop-based term  $P_{cmd}$  is changed in every time period, based on the wind speed that the wind plant is forecasted (or estimated) to receive over that time period. In contrast, the parameter  $R_W$ , which corresponds to the slope of the droop characteristic curve and is calculated at the average wind speed, is unchanged.

Let us assume that in the example power system of Figure 4.4(a) the wind speed that is forecasted for the time period TP1 is equal to the average wind speed, i.e.,  $v_w = 8.85$  m/s. Therefore, the parameters of the wind plant droop characteristic are calculated as  $R_W = -6.283$  and  $P_{W0} = 5.4$  MW. Moreover, the parameters of CPP1 droop characteristic [equation (4.4)] are determined as  $R_{G-1} = -0.857$  and  $P_{G0-1} = 17.6$  MW. At steady state, the wind plant, CPP1, and CPP2 generate 5.4 MW, 17.6 MW, and 4 MW, respectively, to supply the constant power load of 27 MW. Let us further assume that the forecasted wind speed for the time period TP2 is equal to  $v_w = 9.52$  rad/s,

which corresponds to the maximum available power,  $P_{opt}$ , equal to 7.5 MW. Thus, based on the proposed droop characteristic shown in Figure 4.9,  $P_{W0}$  is changed to 6.9 MW in this time period, whereas  $R_W$  is unchanged. To reach the rated frequency (60 Hz) at steady state, the parameter  $P_{G0-1}$  of CPP1 should be reduced to 16.1 MW, while  $R_{G-1}$  is unchanged. This is achieved by the secondary frequency response of CPP1, as described in Subsection 4.2.4. Therefore, in time period TP2, the output powers of the wind plant, CPP1, and CPP2, at steady state, are 6.9 MW, 16.1 MW, and 4 MW, respectively, and the frequency is settled at 60 Hz. In a similar way, the parameters of the wind plant and CPP1 droop characteristics can be calculated, if the forecasted wind speed is less than the average value. Assuming that the wind speed during time period TP3 is equal to 7 m/s, which corresponds to  $P_{opt} = 3$  MW,  $P_{W0}$  is changed to 2.4 MW to achieve a 0.6 MW wind generation reserve. Therefore, at steady state, the output powers of the wind plant, CPP1, and CPP2 are 2.4 MW, 20.6 MW, and 4 MW, respectively, and the frequency is again settled at 60 Hz.

Let us assume that the example wind plant can ensure to supply to the grid a minimum amount of power equal to 20% of its rated generation capacity, i.e., 3 MW. Thus, the wind speed of 7 m/s at which the maximum available power of the wind plant is equal to 3 MW is referred in this chapter to as the *minimum wind speed*. In the example power system of Figure 4.4(a), the total available generation capacities of the wind plant and CPP1 should be equal or higher than  $P_L = 27$  MW, such that the power system can maintain its stability after CPP2 is lost. Therefore, to meet the two objectives of (1) supplying the constant power load after the loss of CPP2, and (2) maintaining the power reserves in the wind plant and CPP1 similar to the ones at the average wind speed, even if the available wind power is reduced to its minimum value, the maximum generation capacity of CPP1 in the example power system should be increased by 3 MW, which is calculated from the difference between the maximum available powers of the wind plant at the average and minimum wind speeds. Hence, to compensate for the decline of the available wind power from its average value, due to the intermittent nature of wind, the maximum generation capacity of CPP1 in the example power system is raised to 25 MW.

Figure 4.10 illustrates the responses of the example power system after a sudden loss of CPP2, for the three aforementioned time periods as: TP1 [Figures 4.10(a)-(d)], TP2 [Figures 4.10(e)-(h)], and TP3 [Figures 4.10(i)-(l)]. It is observed that the dynamic responses have an identical pattern in all the three cases, due to the same amount of the available generation reserves. However, the pre- and post-contingency steady state

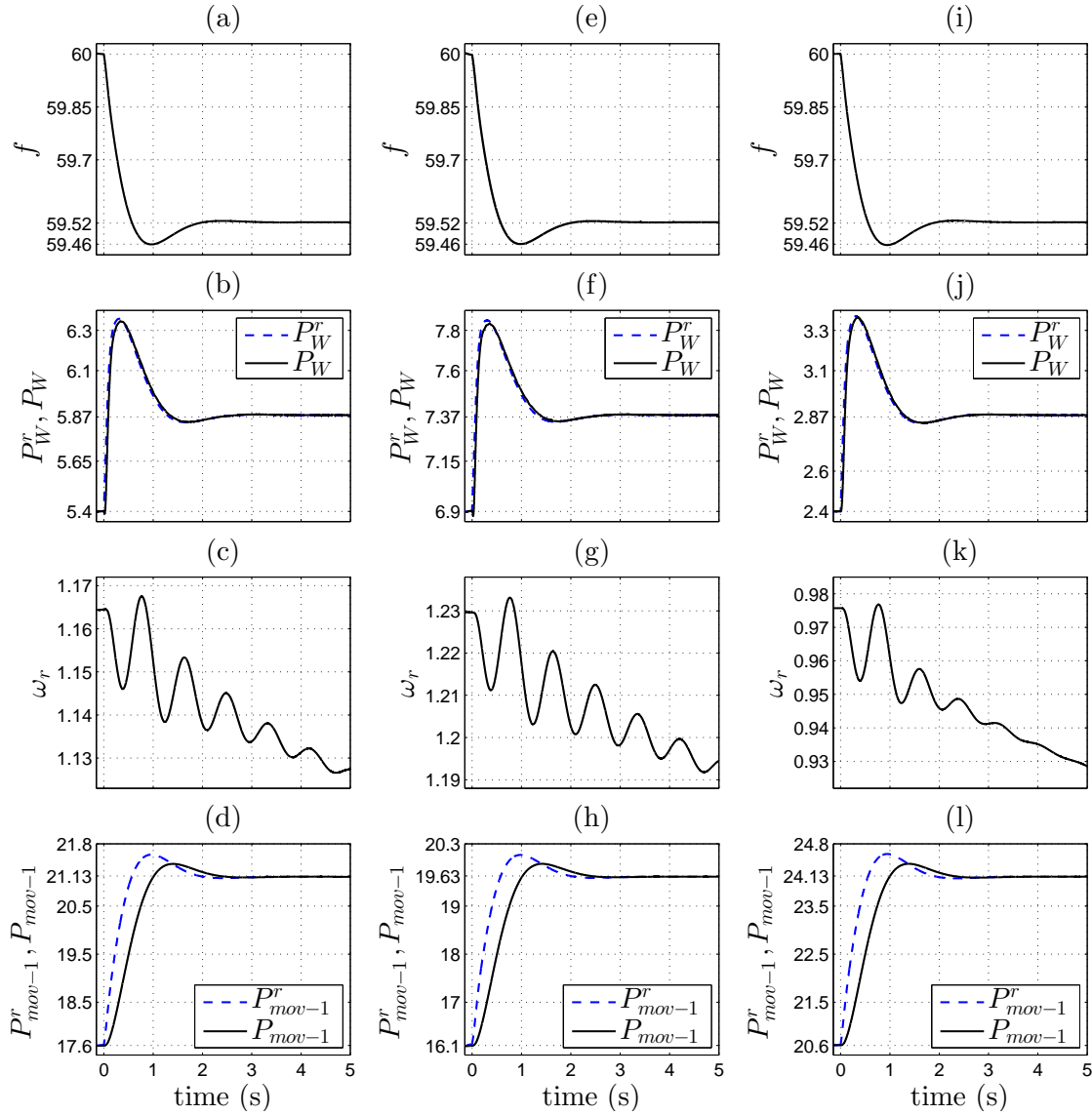


Figure 4.10: Responses of the example power system to a sudden loss of CPP2, at different wind speeds.

values of the wind plant and CPP1 are different.

### 4.3.6 Impact of Wind Speed Intermittency on Frequency Regulation

Due to the stochastic nature of wind, the real wind speed experiences deviations from the forecasted value for a specific period of time. Therefore, to ensure a reliable and safe operation of a power system with large wind power penetration, the impact of wind speed intermittency on the frequency response of the power system must be taken into

account. It should be noted that large variations in aggregated wind generation do not occur suddenly and, instead, they can evolve gradually. Hence, it is assumed that the secondary frequency response of CPP1 can adjust its output power setpoint,  $P_{G0-1}$ , in response to gradual wind power variations, such that the system frequency is maintained at 60 Hz, at steady state, over the normal operation of the example power system.

Let us assume that the wind speed for a given time period is forecasted to be 7.46 m/s, which corresponds to  $P_{opt} = 3.6$  MW. To provide 0.6 MW wind generation reserve,  $P_{W0}$  is chosen equal to 3 MW. Consequently, at steady state, CPP1 generates 20 MW to maintain the frequency at 60 Hz. If the real wind speed declines from the forecasted value towards the minimum wind speed, i.e., 7 m/s, the real available wind generation reserve reduces towards zero, accordingly. However, before the loss of CPP2, the wind plant and CPP1 generate their output power setpoints of 3 MW and 20 MW, respectively. Figures 4.11(a)-(d) illustrate the response of the example power system to a sudden loss of CPP2, when  $v_w = 7.15$  m/s (which corresponds to  $P_{opt} = 3.2$  MW). Initially, the wind plant provides inertial and primary frequency responses by increasing its output power to prevent the frequency from falling below 59.4 Hz. The increase of the output power is supplied from the available wind generation reserve in the wind plant and extraction of the kinetic energy of rotor. Therefore, the rotor decelerates and the saturation limit of the hard limiter in the wind plant control scheme,  $k_{opt}\omega_r^3$ , decreases, until, at  $t = 6.3$  s,  $P_p^r$  becomes saturated. As the rotor speed declines further, the saturation limit (and, consequently,  $P_W^r$ ) continues to decrease, and the frequency experiences another drop due to the decline in the wind power generation. At steady state, the setpoint  $P_W^r$  is equal to  $k_{opt}\omega_r^3$ , and the wind plant is operating in the MPPT mode and is delivering its maximum available power to the grid.

Figures 4.11(e)-(h) illustrate the response of the example power system, when wind speed is at its minimum value. Before  $t = 0$  s, the wind plant is operating in the MPPT mode, due to the saturation of the hard limiter, and there is no generation reserve available in the wind plant. Consequently, after the loss of CPP2, wind plant can only provide inertial frequency response by extracting the kinetic energy of its rotor. Thus, after the initial contribution to system frequency response, the wind plant requires to draw power from the grid to restore its pre-contingency operating condition [Figure 4.11(f)]. As Figure 4.11(e) shows, the minimum frequency in this case is equal to 59.35 Hz, which is outside the acceptable range. Figures 4.11(i)-(l) further illustrate the response of the system when the parameters of the inertia-emulating control are changed to  $\tau_d =$

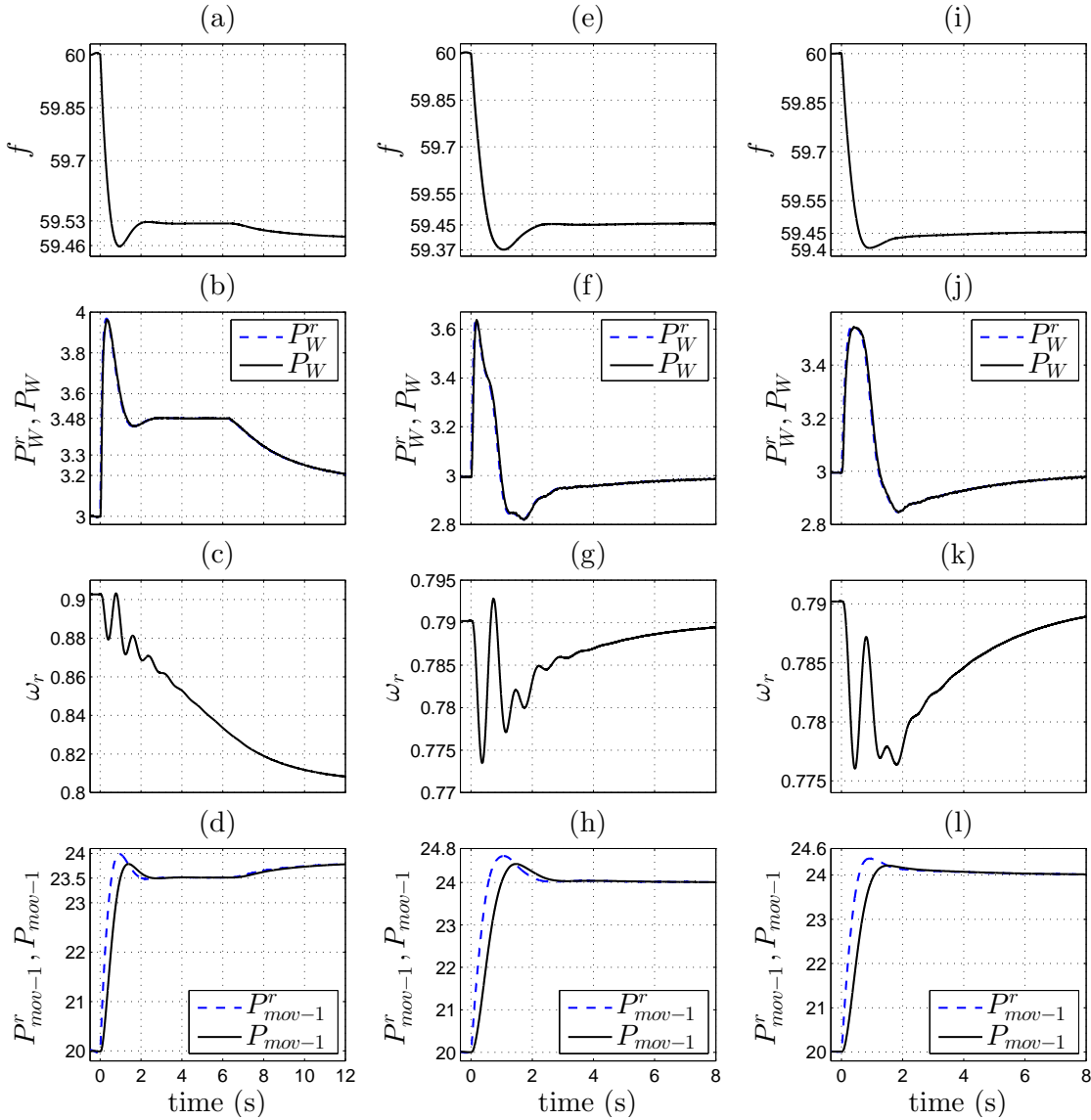


Figure 4.11: Responses of the example power system to the wind speed intermittency.

0.4 s and  $k_{int} = 1.5k_{int0}$ , where  $k_{int0} = -J_G\omega_0/p^2$ . It is observed from Figure 4.11(i) that the minimum frequency is improved to 59.4 Hz.

The impact of changing the parameters  $\tau_d$  and  $k_{int}$  of the inertia-emulating term,  $P_{int}$ , on the system frequency response depends highly on the power system parameters and, thus, care should be taken to ensure that the kinetic energy discharge from the wind plant does not hinder the function of the CPPs. For instance, in the example power system, a large kinetic energy discharge from the wind plant in a short time period, subsequent to the loss of CPP2, reduces the ROCOF such that CPP1 slightly increases its output power. However, the power generation of CPP1 is insufficient and the frequency drops



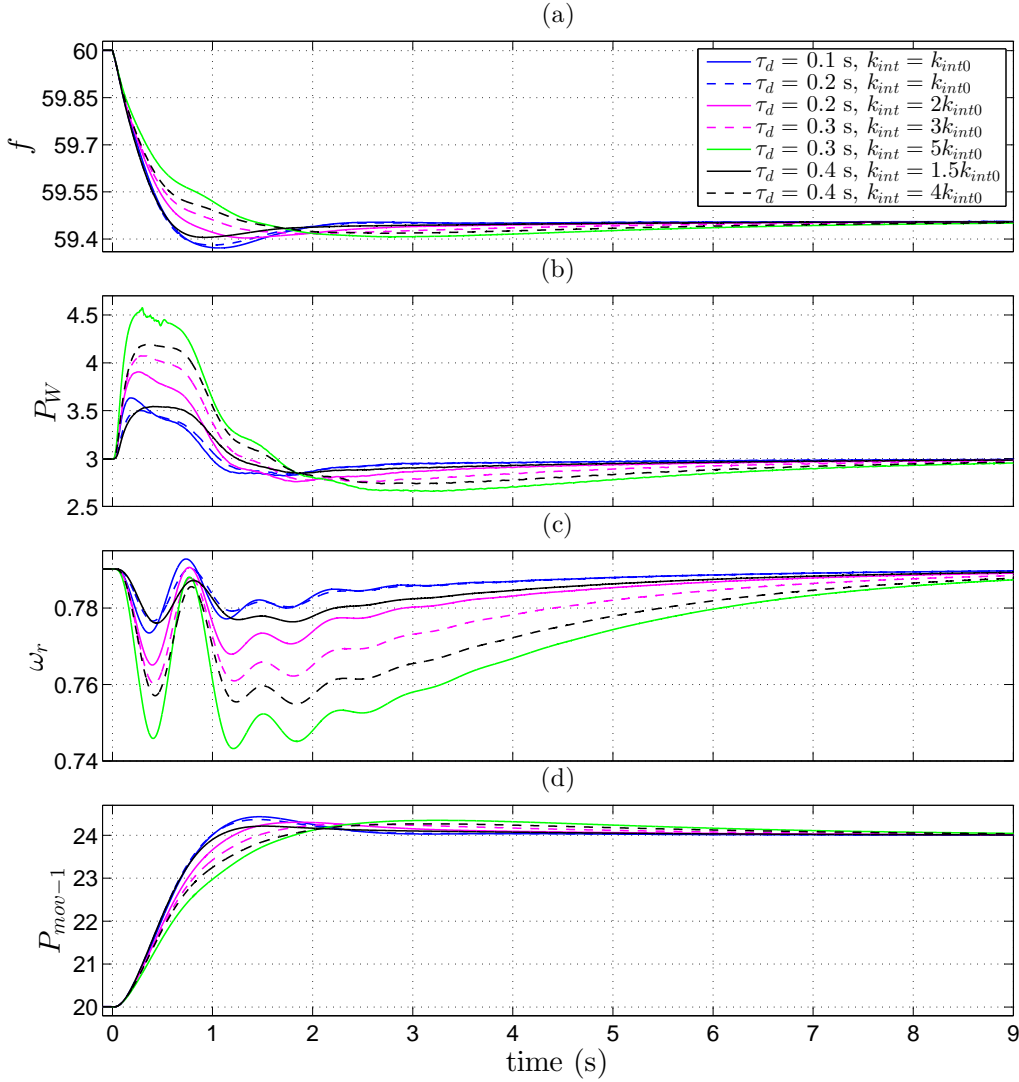


Figure 4.12: Response of the example power system with different values of the inertia-emulating control parameters.

again after the inertial frequency response from the wind plant is over. In contrast, a better frequency response is achieved by a lower kinetic energy discharge from the wind plant which lasts for a longer period of time, such that the governor of CPP1 can follow up. Moreover, the performance of the wind plant at all the operating points should be investigated to ensure the reliability of the whole system over the entire range of wind speeds. Figure 4.12 shows the response of the example power system for different combinations of  $\tau_d$  and  $k_{int}$ , when  $v_w = 7$  m/s and the wind plant is operating in the MPPT mode before  $t = 0$  s.

Figure 4.13 illustrates the frequency response of the example power system, when

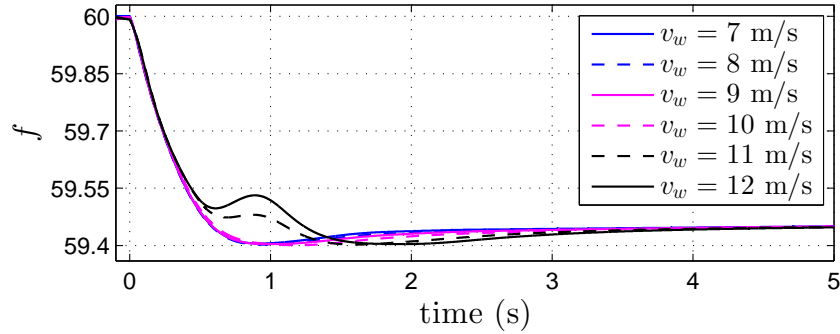


Figure 4.13: Frequency response of the system at different wind speeds.

the wind plant is operating in the MPPT mode before the loss of CPP2, and the wind speed is changed from 7 m/s to 12 m/s, in steps of 1 m/s. The parameters of the wind plant inertia-emulating control are chosen as  $\tau_d = 0.4$  s and  $k_{int} = 1.5k_{int0}$ . It is observed that the minimum frequency of the example power system remains within the acceptable range at all the operating points.

## 4.4 Summary and Conclusion

This chapter proposed an enhanced control strategy that enables a direct-drive PMSG-based WECS to contribute to frequency regulation process, by effectively using its available generation reserve and the kinetic energy of its rotor, such that a stable performance of the WECS over the operating range is ensured. The impact of wind speed intermittency on the frequency response of an example wind plant in a host power system was examined, based on which the parameters of the proposed control was adjusted in order to maintain the reliability of the example power system in response to a specific contingency event, under different wind speed regimes. The effectiveness of the proposed control strategy was demonstrated by time-domain simulation studies. It was concluded that the example wind plant is able to provide a frequency response identical to the one in a CPP. However, due to the stochastic nature of wind, care should be taken to dedicate suitable amount of generation reserve in CPPs to compensate for the potential deficit of wind power.

# Chapter 5

## Summary, Conclusion, and Future Work

### 5.1 Summary

The anticipated large-scale integration of WECSs into the electric power system indicates that the system operators should be able to control the output power of modern WECSs, to more effectively take part in the control of the power system and to operate through grid contingencies. These requirements introduce new challenges to the control of modern WECSs. Extensive research and development efforts have been carried out to introduce new technologies and control strategies for modern WECSs to resolve the technical issues associated with the ever-increasing wind power incorporation. Moreover, direct-drive variable-speed WECSs that employ high-pole PMSGs are expected to be widely deployed in the future, due to their low-loss generators, low maintenance requirements, and quiet drive-trains, which calls for studying their capabilities in meeting the new requirements. The main objective of this research is to address some concerns related to the large-scale integration of WECSs with the power system. The issues studied in the thesis can generally be classified into two parts: (i) output real-power control of a direct-drive PMSG-based WECS and its internal stability, and (ii) contribution of WECSs to the frequency regulation process.

In Chapter 1 of this thesis, the research objectives and contributions of the thesis are presented. Chapter 1 also includes an introduction to WECSs and their advantages and challenges. Chapter 2 of this thesis focuses on the modeling and control of a direct-drive PMSG-based WECS; in this chapter, a strategy for real power control of the WECS is

proposed based on rapid torque control. Then, the internal stability of the WECS is assessed by eigenvalue analysis. A supplementary damping scheme is further presented and tuned for the proposed power control strategy to damp the drive-train torsional modes of the WECS. Moreover, an alternative control structure for the WECS is introduced in Chapter 3, and a damping mechanism is proposed to improve the capability of the WECS to damp the drive-train oscillatory modes and maintain internal stability, even if its output power is regulated.

Chapter 4 of this thesis concentrates on the contribution of WECSs to frequency regulation process in a power system. A control strategy is proposed for a WECS to provide inertial and primary frequency responses similar to the ones in a CPP, by effectively using its available generation reserve and the kinetic energy of its rotor. Moreover, the impact of wind speed intermittency on the frequency response of a power system with a large wind power penetration is studied in Chapter 4, and the control parameters of WECSs are adjusted to ensure a reliable operation of the power system, under different wind speed regimes.

## 5.2 Conclusion

The conclusions of this thesis are as follows:

- It was discussed that rapid torque control in the proposed power control strategy for a PMSG-based WECS can excite its drive-train torsional modes, which can even result in instabilities. Therefore, the thesis presented a supplementary damping scheme and a procedure for tuning its parameters. It was shown that the proposed strategy enables rapid control of the WECS output power, from small values up to the maximum power that corresponds to the prevailing wind conditions, while the internal stability of the WECS is ensured. The thesis also demonstrated that, with the proposed power control strategy, the mode of operation in a WECS can be smoothly switched between the MPPT mode and the controlled-power mode.
- The thesis further explained that the functions of the voltage-sourced converters in a WECS can be switched. The advantage of this alternative control structure over the more common one is that it mitigates the sensitivity of the WECS output power to power fluctuations caused by wind speed variations and drive-train oscillatory modes. The thesis discussed that the basic control of the WECS can not ensure

the damping of oscillations if the output power is regulated. Therefore, a damping mechanism was proposed and it was shown that a trade-off exists between the damping of drive-train torsional modes and speed of response of the dc-link voltage, based on which the parameters of the proposed strategy were tuned.

- Contribution of WECSs to frequency regulation process in the modern power systems can be essential in reducing the operational cost and improving the security of the system. Therefore, the thesis proposed an enhanced control strategy that enables a WECS to provide inertial and primary frequency responses. It was concluded that a WECS is able to provide a frequency response similar to the one in a CPP. However, due to the stochastic nature of wind, care should be taken to dedicate suitable amount of generation reserve in CPPs to compensate for the potential deficit of wind power. The impact of the wind speed intermittency on the frequency response of WECSs was also addressed in the thesis. It was demonstrated that the parameters of the inertia-emulating control in WECSs can be adjusted to improve the transient performance of the power system, subsequent to a generation loss.

### 5.3 Future Work

The following topics are suggested for a future work:

- Developing a damping strategy for a WECS by combining the strategies presented in this thesis, that benefits from the advantages of both methods, by reducing the impact of filter parameters on the effectiveness of the damping mechanism while a fast response of the dc-link voltage is ensured. The control strategies can be further implemented in an experimental setup to study their performance in practice.
- Extending the proposed control strategies in this thesis to a PMSG-based WECS that uses a diode rectifier and a dc-dc step-up converter on the generator side of its full-scale power-electronic converter. The performance of this configuration can be compared with the one presented in this thesis, with regards to operational indices such as output real-power controllability and internal stability achieved by damping torsional modes. The presented control strategies can also be extended to other classes of electronically-interfaced WECSs that are commercially used, such as DFIG-based WECSs or WECS with full-scale converters that employ squirrel cage induction generators.

- Investigating the contribution of WECSs with the proposed control strategies to frequency regulation in larger power systems with different generation resources and various types of consumers, and developing procedures for adjusting the inertial response of WECSs in power systems with different dominant generation technologies. Moreover, an uneven distribution of wind speed among the constituting WECSs in a wind plant can be studied and suitable control strategies can be developed to ensure a stable and effective operation of the wind plant. The possible impacts of reactive power injection (or absorption) by WECSs on their frequency response capabilities can also be studied.

# Appendix A

## Parameters of the Example WECS in Chapters 2 and 3

The parameters of the example WECS in Chapters 2 and 3 are reported in Tables A.1 and A.2. The other parameters are introduced in Table A.3.

Table A.1: Wind Turbine Parameters

Parameters	Value	Comments
rated power	5 MW	
rated angular speed	12.9 rpm	
rated wind speed	12 m/s	
radius	60.5 m	$R$
$k_{opt}$	2023251	
pitch angle range	1-90 deg.	
moment of inertia	12892100 kgm <sup>3</sup>	$J_t$
$\alpha_1, \alpha_2, \alpha_3$	0.73, 151, 0.58	
$\alpha_4, \alpha_5, \alpha_6$	0.002, 2.14, 13.2	
$\alpha_7, \alpha_8, \alpha_9$	18.4, 0.02, 0.003	

Table A.2: PMSG Parameters

Parameters	Value	Comments
rated power	5.0 MW	
rated Voltage	2.2 kV,rms	$l-l$
rated current	1.3 kA,rms	
rated frequency	12.9 Hz	
number of pole pairs	60	$p$
maximum rotor flux	22.25 Wb	$\lambda_m$
$d$ - and $q$ -axis inductance	4.0 mH	$L_d, L_q$
stator resistance	5.35 m $\Omega$	$R_s$
moment of inertia	1371500 kgm <sup>3</sup>	$J_r$

Table A.3: Compensators and Other Parameters

Parameters	Value	Comments
$k_{p1}, k_{i1}$	0.4, 0.535	Fig. 2.2
$k_{p2}, k_{i2}$	0.4, 0.535	Fig. 2.2
$k_{p3}, k_{i3}$	1.0, 2.4	Fig. 2.3
$k_{p4}, k_{i4}$	130, 90	Fig. 2.3
air mass density	1.225 kg/m <sup>3</sup>	$\rho$
drive-train shaft stiffness	106321835 Nm/rad	$k_s$
switching frequency	1500 Hz	



# Appendix B

## Analytical Forms of Matrices

The analytical forms of the matrices  $\mathbf{A}_1$ ,  $\mathbf{A}_2$ ,  $\mathbf{A}_3$ ,  $\mathbf{A}_4$ ,  $\mathbf{B}_1$ ,  $\mathbf{B}_2$ ,  $\mathbf{B}_3$ , and  $\mathbf{B}_4$  are presented in (B.1) through (B.8).

$$\mathbf{A}_1 = \begin{bmatrix} \frac{1}{J_t} k_1 & 0 & -\frac{k_s}{J_t} \\ 0 & 0 & \frac{k_s}{J_r} \\ 1 & -1 & 0 \\ 0 & 0 & 0 \\ 0 & -k_{i3} \bar{T}_e + 3 k_{i3} k_{opt} \bar{\omega}_r^2 & -\frac{k_{p3} k_s}{J_r} \bar{T}_e + \frac{3 k_{p3} k_{opt} k_s}{J_r} \bar{\omega}_r^2 \\ 0 & 0 & 0 \\ -\frac{1}{J_r} & 0 & 0 \\ 0 & 0 & 0 \\ -\frac{1}{\tau_i} & \frac{1}{\tau_i} \\ \frac{k_{p3}}{\tau_i} \bar{\omega}_r + \frac{k_{p3}}{J_r} \bar{T}_e - k_{i3} \bar{\omega}_r - \frac{3 k_{p3} k_{opt}}{J_r} \bar{\omega}_r^2 & -\frac{k_{p3}}{\tau_i} \bar{\omega}_r \end{bmatrix}, \quad (\text{B.1})$$

$$\mathbf{A}_2 = \begin{bmatrix} \frac{1}{J_t} k_1 & 0 & -\frac{k_s}{J_t} & 0 & 0 \\ 0 & 0 & \frac{k_s}{J_r} & -\frac{1}{J_r} & 0 \\ 1 & -1 & 0 & 0 & 0 \\ 0 & 0 & 0 & -\frac{1}{\tau_i} & \frac{1}{\tau_i} \\ 0 & -k_{i3} \bar{T}_e & -\frac{k_{p3} k_s}{J_r} \bar{T}_e & \frac{k_{p3}}{\tau_i} \bar{\omega}_r + \frac{K_{p3}}{J_r} \bar{T}_e - k_{i3} \bar{\omega}_r & -\frac{k_{p3}}{\tau_i} \bar{\omega}_r \end{bmatrix}, \quad (\text{B.2})$$

$$\mathbf{A}_3 = \begin{bmatrix} \frac{1}{J_t} k_1 & 0 & -\frac{k_s}{J_t} \\ 0 & 0 & \frac{k_s}{J_r} \\ 1 & -1 & 0 \\ 0 & 0 & 0 \\ 0 & -k_{i3}\bar{T}_e + 3k_{i3}k_{opt}\bar{\omega}_r^2 & -\frac{k_{p3}k_s}{J_r}\bar{T}_e + \frac{3k_{p3}k_{opt}k_s}{J_r}\bar{\omega}_r^2 \\ 0 & 0 & 0 \\ \frac{k_s}{J_r} & -\frac{k_s}{J_r} & 0 \end{bmatrix}, \quad (B.3)$$

$$\begin{bmatrix} 0 & 0 & 0 & 0 & 0 \\ -\frac{1}{J_r} & 0 & 0 & 0 & 0 \\ 0 & 0 & 0 & 0 & 0 \\ -\frac{1}{\tau_i} & \frac{1}{\tau_i} & \frac{k_d}{\tau_i} & 0 & 0 \\ \frac{k_{p3}\bar{T}_e}{J_r} + \frac{k_{p3}\bar{\omega}_r}{\tau_i} - k_{i3}\bar{\omega}_r - \frac{3k_{p3}k_{opt}\bar{\omega}_r^2}{J_r} & -\frac{k_{p3}\bar{\omega}_r}{\tau_i} & -\frac{k_{p3}k_d}{\tau_i}\bar{\omega}_r & 0 & 0 \\ 0 & 0 & 0 & 1 & 0 \\ \frac{1}{J_r\tau_i} & -\frac{1}{J_r\tau_i} & -\omega_c^2 - \frac{k_d}{J_r\tau_i} & -\frac{\omega_c}{Q} & 0 \end{bmatrix}, \quad (B.3)$$

$$\mathbf{A}_4 = \begin{bmatrix} \frac{1}{J_t} k_1 & 0 & -\frac{k_s}{J_t} \\ 0 & 0 & \frac{k_s}{J_r} \\ 1 & -1 & 0 \\ 0 & 0 & 0 \\ 0 & -k_{i3}\bar{T}_e & -\frac{k_{p3}k_s}{J_r}\bar{T}_e \\ 0 & 0 & 0 \\ \frac{k_s}{J_r} & -\frac{k_s}{J_r} & 0 \end{bmatrix}$$

$$\begin{bmatrix} 0 & 0 & 0 & 0 & 0 \\ -\frac{1}{J_r} & 0 & 0 & 0 & 0 \\ 0 & 0 & 0 & 0 & 0 \\ -\frac{1}{\tau_i} & \frac{1}{\tau_i} & \frac{k_d}{\tau_i} & 0 & 0 \\ \frac{k_{p3}\bar{T}_e}{J_r} + \frac{k_{p3}\bar{\omega}_r}{\tau_i} - k_{i3}\bar{\omega}_r & -\frac{k_{p3}\bar{\omega}_r}{\tau_i} & -\frac{k_{p3}k_d}{\tau_i}\bar{\omega}_r & 0 & 0 \\ 0 & 0 & 0 & 1 & 0 \\ \frac{1}{J_r\tau_i} & -\frac{1}{J_r\tau_i} & -\omega_c^2 - \frac{k_d}{J_r\tau_i} & -\frac{\omega_c}{Q} & 0 \end{bmatrix}, \quad (B.4)$$

$$\mathbf{B}_1 = \left[ \begin{array}{cccccc} \frac{1}{J_t} k_2 & 0 & 0 & 0 & 0 & 0 \end{array} \right]^T, \quad (\text{B.5})$$

$$\mathbf{B}_2 = \left[ \begin{array}{cccccc} \frac{1}{J_t} k_2 & 0 & 0 & 0 & 0 & 0 \\ 0 & 0 & 0 & 0 & k_{i3} & 0 \\ 0 & 0 & 0 & 0 & k_{p3} & 0 \end{array} \right]^T, \quad (\text{B.6})$$

$$\mathbf{B}_3 = \left[ \begin{array}{cccccc} \frac{1}{J_t} k_2 & 0 & 0 & 0 & 0 & 0 \\ 0 & 0 & 0 & 0 & 0 & 0 \\ 0 & 0 & 0 & 0 & 0 & 0 \end{array} \right]^T, \quad (\text{B.7})$$

$$\mathbf{B}_4 = \left[ \begin{array}{cccccc} \frac{1}{J_t} k_2 & 0 & 0 & 0 & 0 & 0 \\ 0 & 0 & 0 & 0 & k_{i3} & 0 \\ 0 & 0 & 0 & 0 & k_{p3} & 0 \end{array} \right]^T. \quad (\text{B.8})$$

The entries of these matrices are functions of the steady-state values of the variables (denoted by the overline). The entries of matrices are also functions of the parameters  $k_1$  and  $k_2$  which are defined as

$$k_1 = \frac{\partial T_{tur}}{\partial \omega_t} = \frac{\partial \left( \frac{P_{tur}}{\omega_t} \right)}{\partial \omega_t} = \left( -\frac{0.5 \rho \pi R^2 C_p v_w^3}{\omega_t^2} \right) + \left( \frac{0.5 \rho \pi R^2 v_w^3}{\omega_t} \right) \frac{\partial C_p}{\partial \omega_t}, \quad (\text{B.9})$$

$$k_2 = \frac{\partial T_{tur}}{\partial v_w} = \frac{\partial \left( \frac{P_{tur}}{\omega_t} \right)}{\partial v_w} = \left( \frac{1.5 \rho \pi R^2 C_p v_w^2}{\omega_t} \right) + \left( \frac{0.5 \rho \pi R^2 v_w^3}{\omega_t} \right) \frac{\partial C_p}{\partial v_w}, \quad (\text{B.10})$$

and  $\partial C_p / \partial \omega_t$  and  $\partial C_p / \partial v_w$  are formulated as

$$\begin{aligned} \frac{\partial C_p}{\partial \omega_t} &= \frac{\partial C_p}{\partial \lambda_i} \frac{\partial \lambda_i}{\partial \lambda} \frac{\partial \lambda}{\partial \omega_t} \\ &= \left[ -\frac{\alpha_1 \alpha_2}{\lambda_i^2} e^{-\frac{\alpha_7}{\lambda_i}} + \left( \frac{\alpha_2}{\lambda_i} - \alpha_3 \beta - \alpha_4 \beta^{\alpha_5} - \alpha_6 \right) \frac{\alpha_1 \alpha_7}{\lambda_i^2} e^{-\frac{\alpha_7}{\lambda_i}} \right] \\ &\times \left[ \frac{1}{(\lambda - \alpha_8 \beta)^2} \left( \frac{1}{\lambda - \alpha_8 \beta} - \frac{\alpha_9}{\beta^3 + 1} \right)^{-2} \right] \times \left( \frac{R}{v_w} \right), \end{aligned} \quad (\text{B.11})$$

$$\frac{\partial C_p}{\partial v_w} = \frac{\partial C_p}{\partial \lambda_i} \frac{\partial \lambda_i}{\partial \lambda} \frac{\partial \lambda}{\partial v_w} = \frac{\partial C_p}{\partial \lambda_i} \frac{\partial \lambda_i}{\partial \lambda} \left( -\frac{R \omega_t}{v_w^2} \right). \quad (\text{B.12})$$

# Appendix C

## Parameters of the Example Wind Plant and CPPs in Chapter 4

The parameters of the CPPs in the example power systems of Chapter 4 are reported in Table C.1. The parameters of the turbine and generator in the model of the example wind plant are also described in Tables C.2 and C.3, respectively.

Table C.1: Conventional Power Plants Parameters

Parameters	Value	Comments
CPP1, rated power	22 MW	
CPP1, rated voltage	2.2 kV	rms $l-l$
CPP1, rated angular speed	3600 rpm	
CPP1, number of pole pairs	1	$p_{G1}$
CPP1, moment of inertia	246.25 kgm <sup>2</sup>	$H = 3.5$ s
CPP1, governor delay	0.29 s	
CPP2, rated power	4 MW	
CPP2, rated voltage	2.2 kV	rms $l-l$
CPP2, rated angular speed	3600 rpm	
CPP2, number of pole pairs	1	$p_{G2}$
CPP2, moment of inertia	1083.52 kgm <sup>2</sup>	$H = 3.5$ s
CPP2, governor delay	0.06 s	
CPP3, rated power	6 MW	
CPP3, rated voltage	2.2 kV	rms $l-l$
CPP3, rated angular speed	3600 rpm	
CPP3, number of pole pairs	1	$p_{G3}$
CPP3, moment of inertia	295.5 kgm <sup>2</sup>	$H = 3.5$ s
CPP3, governor delay	0.09 s	

Table C.2: Wind Plant Model - Turbine Parameters

Parameters	Value	Comments
rated power	15 MW	
rated angular speed	12.9 rpm	
rated wind speed	12 m/s	
radius	60.5 m	$R$
$k_{opt}$	6069753	
pitch angle range	1-90 deg.	
moment of inertia	38676300 kgm <sup>3</sup>	$J_t$
drive-train stiffness	318515505 Nm/rad	$k_s$

Table C.3: Wind Plant Model - Generator Parameters

Parameters	Value	Comments
rated power	15 MW	
rated voltage	2.2 kV	rms $l-l$
rated current	3.9 kA	rms
rated frequency	12.9 Hz	
number of pole pairs	60	$p$
maximum rotor flux	22.25 Wb	$\lambda_m$
$d$ - and $q$ -axis inductance	1.33 mH	$L_d, L_q$
stator resistance	1.78 m $\Omega$	$R_s$
moment of inertia	4114500 kgm <sup>3</sup>	$J_r$

# Bibliography

- [1] Canadian Wind Energy Association (CanWEA), available online: <http://www.canwea.ca>.
- [2] Global Wind Energy Council (GWEC), available online: <http://www.gwec.net>.
- [3] S. Heier, *Grid Integration of Wind Energy Conversion Systems*, Chicester, U.K.: Wiley, 2nd Edition, 2006.
- [4] P. Musgrove, "Wind energy conversion - an introduction", *IEE Proceeding*, vol. 130, No. 9, pp. 506-516, Dec. 1983.
- [5] Global Wind Energy Council (GWEC), Wind Force 12, available online: [http://www.ewea.org/fileadmin/ewea\\_documents/documents/publications/WF12/wf12-2005.pdf](http://www.ewea.org/fileadmin/ewea_documents/documents/publications/WF12/wf12-2005.pdf)
- [6] T. Ackermann, *Wind Power in Power Systems*, John Wiley & Sons, 742 pages, Jan. 2005.
- [7] J. Manwell, J. McGowan, and A. Rogers, *Wind Energy Explained: Theory, Design and Application*, John Wiley & Sons, 2nd Edition, 704 pages, Jan. 2010.
- [8] G. Boyle, *Renewable Energy: Power for a Sustainable Future*, The Open University, Oxford, 2nd Edition, May 2004.
- [9] M.R. Patel, *Wind and Solar Power Systems*, New York, USA: CRC Press, 368 pages, Mar 1999.
- [10] A.D. Hansen, L. Hansen, "Wind turbine concept market penetration over 10 Years (1995-2004)," *Wind Energy*, vol. 10, issue. 1, pp. 81-97, Jan./Feb. 2007.
- [11] Y. Duan and R. G. Harley, "Present and future trends in wind turbine generator designs," in *Proc. IEEE Power Electron. Mach. Wind Appl.*, pp. 1-6, Jun. 2009.

- [12] J. Carrasco, L. Franquelo, J. Bialasiewicz, E. Galvan, et. al. "Power-electronic systems for the grid integration of renewable energy sources: A survey," *IEEE Trans. on Industrial Electronics*, vol. 53, no. 4, pp. 1002-1016, Jun. 2006.
- [13] S. Jockel, VENSYS Energiesysteme GmbH & Co. KG, "High Energy Production plus Built-in Reliability the New VENSYS 70/77 Gearless Wind Turbines in the 1.5 MW Class," The European Wind Energy Conference and Exhibition (EWEC), Athens, Greece, Feb./Mar. 2006.
- [14] Y. Chen, P. Pillary, and A. Khan, "PM wind generator topologies," *IEEE Trans. on Industrial Applications*, vol. 41, no. 6, pp. 1619-1626, Nov./Dec. 2005.
- [15] D. Bang, H. Polinder, G. Shrestha, and J.A. Ferreira, "Review of Generator Systems for Direct-Drive Wind Turbines," in *Proc. European Wind Energy Conference & Exhibition (EWEC)*, Brussels, Belgium, Mar./Apr. 2008.
- [16] L. Soderlund and J. T. Eriksson, "A permanent-magnet generator for wind power applications," *IEEE Trans. on Magnetics*, vol. 32, no. 4, pp. 2389-2392, Jul. 1996.
- [17] C.J.A. Versteegh, GarradHassan & Partners NL, "Design of the Zephyros Z72 wind turbine with emphasis on the direct drive PM generator," in *proc. 4th Nordic Workshop on Power and Industrial Electronics (NORPIE)*, Trondheim, Norway, June 2004.
- [18] Vestas V90 3 MW Wind Turbine Brochure, available online: [http://www.vestas.com/en/products\\_and\\_services/turbines/v90-3\\_0\\_mw](http://www.vestas.com/en/products_and_services/turbines/v90-3_0_mw)
- [19] European Commission, Energy, Renewable sources, *Wind turbine grid connection and interaction*, available online: [http://ec.europa.eu/energy/res/sectors/doc/wind\\_energy/maxibrochure\\_final\\_version.pdf](http://ec.europa.eu/energy/res/sectors/doc/wind_energy/maxibrochure_final_version.pdf)
- [20] W. Qiao, and R. G. Harley, "Grid connection requirements and solutions for DFIG wind turbines," in *Proc. IEEE Energy 2030 Conf.*, Nov. 2008, pp. 1-8.
- [21] P.B. Eriksen, T. Ackermann, H. Abildgaard, P. Smith, W. Winter, and J.M. Rodriguez, "System operation with high wind penetration," *IEEE Power Energy Magazine*, vol. 3, no. 6, pp. 65-74, Nov./Dec. 2005.
- [22] VentdeRaison, *A rationale for specific European WT-regulations*, July 2012, [online]. Available: [http://ventderaison.com/documents/fiches\\_VDR/rationale\\_specific\\_european\\_regulations\\_2012-07-26.pdf](http://ventderaison.com/documents/fiches_VDR/rationale_specific_european_regulations_2012-07-26.pdf)

- [23] P.S. Georgilakis, "Technical challenges associated with the integration of wind power into power systems," *Renewable and Sustainable Energy Reviews*, vol. 12, pp. 852-863, 2008.
- [24] E.N. Hinrichsen and P.J. Nolan, "Dynamics and stability of wind turbine generators," *IEEE Trans. on Power Apparatus Systems*, vol. PAS-101, no. 8, pp. 2640-2648, Aug. 1982.
- [25] J.K. Pedersen, M. Akke, N.K. Poulsen, and K.O.H. Pedersen, "Analysis of wind farm islanding experiment," *IEEE Trans. on Energy Convers.*, vol. 15, no. 1, pp. 110-115, Mar. 2000.
- [26] J.K. Pederson, et al. "Contribution to a dynamic wind turbine model validation from a wind farm islanding experiment," *Electric Power Systems Research*, vol. 64, issue 1, pp. 41-51, Jan. 2003.
- [27] G. Ramtharan, N. Jenkins, O. Anaya-Lara, and E. Bossanyi, "Influence of rotor structural dynamics representations on the electrical transient performance of FSIG and DFIG wind turbines," *Wind Energy*, vol. 10, pp. 293-301, Jul./Aug. 2007.
- [28] V. Akhmatov, H. Knudsen, and A.H. Nielsen, "Advanced simulation of windmills in the electric power supply," *International Journal of Electrical Power & Energy Systems*, vol. 22, pp. 421-434, 2000.
- [29] V. Akhmatov, A.H. Nielsen, J.K. Pedersen, and O. Nymann, "Variable-speed wind turbines with multi-pole synchronous permanent magnet generators, Part I: Modelling in dynamic simulation tools," *Wind Engineering*, vol. 27, no. 6, pp. 531-548, 2003.
- [30] A.H. Church, *Mechanical vibrations*, John Wiley & Sons, New York, 1994.
- [31] A.D. Hansen and G. Michalke, "Modeling and control of variable-speed multi-pole permanent magnet synchronous generator wind turbine," *Wind Energy*, vol. 11, no. 5, pp. 537-554, Sep./Oct. 2008.
- [32] S. Brownlees, B. Fox, D. Flynn, and T. Littler, "Wind farm induced oscillations," *in Proc. 41st Int. UPEC*, vol. 1, pp. 118-122, Sep. 2006.
- [33] T. Petru, and T. Thiringer, "Modeling of wind turbines for power system studies," *IEEE Trans. on Power Systems*, vol. 17, no. 4, pp. 1132-1139, Nov. 2002.



- [34] E. A. Bossanyi, "Wind turbine control for load reduction," *Wind Energy*, vol. 6, pp. 229-244, 2003.
- [35] E. A. Bossanyi, et al. "Advanced controller research for multi-MW wind turbines in the UPWIND project," *Wind Energy* 2012; 15(1): pp. 119-145.
- [36] S. Jockel, B. Hagenkort, T. Hartkopf, H. Schneider, "Direct-drive synchronous generator system for offshore wind farms with active drive train damping by blade pitching," in *Proc. European Wind Energy Conference*, July 2001, Copenhagen, Denmark, pp. 991-994.
- [37] A. J. G. Westlake, J. R. Bumby, E. Spooner, "Damping the power-angle oscillations of a permanent-magnet synchronous generator with particular reference to wind turbine applications," *Electric Power Applications, IEE Proceedings*, vol. 143, Issue 3, pp. 269-280, 1996.
- [38] S. M. Mueeen, et al. "Transient stability analysis of wind generator by using six-mass drive train model," in *Proc. Int. Conf. on Electrical Machines and Systems (ICEMS)*, Nagasaki, Japan, Nov. 2006.
- [39] S. M. Mueeen, et al. "Comparative study on transient stability analysis of wind turbine generator system using different drive train models," *IET Renewable Power Generation*, vol. 1, no. 2, pp. 131-141, June 2007.
- [40] S. K. Salman, and A. L. J. Teo, "Windmill modeling consideration and factors influencing the stability of a grid-connected wind power-based embedded generator," *IEEE Trans. on Power Systems*, vol. 18, no. 2, pp. 793-802, May 2003.
- [41] B. Singh, S. N. Singh, "wind power interconnection into the power system: a review of grid code requirements," *Elsevier the Electricity Journal*, vol. 22, no. 5, pp. 54-63, June 2009.
- [42] L. Freris, and D. Infield, *Renewable energy in power systems*, John Wiley & Sons, ISBN 978-0-470-01749-4, 284 pages, July 2008.
- [43] P. Kundur, *Power System Stability and Control*. EPRI. New York: McGraw-Hill, 1994.

- [44] J. Aho, A. Buckspan, J. Laks, et al. "Tutorial of wind turbine control for supporting grid frequency through active power control ," *in proc. American Control Conference*, Montreal, Canada, June 2012.
- [45] W. Stevenson and J. Grainger, *Power System Analysis*, New York, US: McGraw-Hill, 1994.
- [46] P. Tielens, D. Van Hertem, "Grid inertia and frequency control in power systems with high penetration of renewables", *Young Researchers Symposium in Electrical Power Engineering* edition:6 location:Delft date:16-17 April 2012.
- [47] T. Bublat and T. Gehlhaar, "Comparison of high technical demands on grid connected wind turbines defined in international Grid Codes," *in 7th International Workshop on Large-Scale Integration of Wind Power into Power Systems*, 2008, pp. 310-315.
- [48] A. Mullane, G. Bryans, and M. O'Malley, "Kinetic energy and frequency response comparison for renewable generation systems," *in Proc. Int. Conf. Future Power Systems*, Nov. 16-18, 2005.
- [49] L. Ruttledge, N.W. Miller, J. O'Sullivan, and D. Flynn, "Frequency Response of Power Systems With Variable Speed Wind Turbines," *IEEE Trans. on Sustainable Energy*, vol. 3, no. 4, pp. 683-691, Oct. 2012.
- [50] J. Morren, J. Pierik, and S. Dehaan, "Inertial response of variable speed wind turbines," *Electric Power Systems Research*, vol. 76, no. 11, pp. 980-987, Jul. 2006.
- [51] J. Ekanayake, and N. Jenkins, "Comparison of the response of doubly fed and fixed-speed induction generator wind turbines to changes in network frequency," *IEEE Trans. Energy Conversion*, vol. 19, no. 4, pp. 800-802, Dec. 2004.
- [52] B. H. Chowdhury and H. T. Ma, "Frequency regulation with wind power plants," *in Proc. IEEE Power & Energy Society General Meeting*, Pittsburgh, Pennsylvania, USA, July 2008.
- [53] P. K. Keung, P. Li, H. Banakar, B. T. Ooi, "Kinetic Energy of Wind- Turbine Generators for System Frequency Support," *IEEE Trans. On Power Systems*, vol. 24, no. 1, pp. 279-287, Feb. 2009.

- [54] EWEA, wind energy - The facts. A guide to the technology, economics and future of wind power, London: Earthscan, 2009, p. 568.
- [55] E. Ela, M. Milligan, and B. Kirby, "Operating Reserves and Variable Generation," *Technical Report*, NREL/TP-5500-51978, August 2011.
- [56] P. Li, H. Banakar, P.K. Keung, H.G. Far, C. Luo, and B.T. Ooi, "MACRO-model of spatial smoothing in wind farms," *IEEE Trans. on Energy Conversion*, vol. 22, no. 1, pp. 119-128, Mar. 2007.
- [57] ERCOT Protocols Section 5: Dispatch. June 1, 2010.
- [58] J. Brisebois and N. Aubut, "Wind farm inertia emulation to fulfill Hydro-Quebec's specific need," in *Proc. IEEE Power and Energy Society General Meeting*, Detroit, USA, July 2011.
- [59] Hydro-Qubec Transnergie, Transmission Provider Technical Requirements for the Connection of Power Plants to the Hydro-Qubec Transmission System, February 2009, Available online: [http://www.hydroquebec.com/transnergie/fr/commerce/pdf/exigence\\_raccordement\\_fev\\_09\\_en.pdf](http://www.hydroquebec.com/transnergie/fr/commerce/pdf/exigence_raccordement_fev_09_en.pdf).
- [60] N. Boccard, "Capacity factor of wind power realized values vs. estimates," *Journal of Energy Policy*, vol. 37, no. 7, pp. 2679-2688, 2009
- [61] Z. Chen, J. M. Guerrero, and F. Blaabjerg, "A review of the state of the art of power electronics for wind turbines," *IEEE Trans. on Power Electronics*, vol. 24, no. 8, pp. 1859-1875, Aug. 2009.
- [62] H. Li, K. L. Shi and P. G. McLaren, "Neural-network-based sensorless maximum wind energy capture with compensated power coefficient," *IEEE Trans. on Industrial Applications*, vol. 41, no. 6, pp. 1548-1556, Nov./Dec. 2005.
- [63] Q. Wang and L. Chang, "An intelligent maximum power extraction algorithm for inverter-based variable speed wind turbine systems," *IEEE Trans. on Power Electronics*, vol. 19, no. 5, pp. 1242-1249, Sep. 2004.
- [64] E. Koutroulis and K. Kalaitzakis, "Design of a maximum power tracking system for wind-energy-conversion applications," *IEEE Trans. on Industrial Electronics*, vol. 53, no. 2, pp. 486-494, April 2006.

- [65] S. Bhowmik, R. Spee, and J. Enslin, "Performance optimization for doubly fed wind power generation systems," *IEEE Trans. on Industrial Applications*, vol. 35, no. 4, pp. 949-958, Jul./Aug. 1999.
- [66] C. Jauch, "Transient and dynamic control of a variable speed wind turbine with synchronous generator," *Wind Energy*, vol. 10, pp. 247-269, May-Jun. 2007
- [67] H. Geng, D. Xu, B. Wu, and G. Yang, "Active damping for PMSG-based WECS with dc-link current estimation," *IEEE Trans. on Industrial Electronics*, vol. 58, no. 4, pp. 1110-1119, April 2011.
- [68] J. Licari, C.E. Ugalde-Loo, J.B. Ekanayake, and N. Jenkins, "Damping of torsional vibrations in a variable-speed wind turbine," *IEEE Trans. on Energy Conversion*, vol. 28, no. 1, pp. 172-180, March 2013.
- [69] J. F. Conroy, and R. Watson, "Frequency response capability of full converter wind turbine generators in comparison to conventional generation," *IEEE Trans. on Power Systems*, vol. 23, no. 2, pp. 649-656, May 2008.
- [70] Z.S. Zhang, Y.Z. Sun, J. Lin, G.J. Li, "Coordinated frequency regulation by doubly fed induction generator-based wind power plants," *IET Renewable Power Generation*, vol. 6, no. 1, pp. 38-47, Jan. 2012.
- [71] Y. Wang, G. Delille, H. Bayem, X. Guillaud, and B. Francois, "High Wind Power Penetration in Isolated Power Systems Assessment of Wind Inertial and Primary Frequency Responses," *IEEE Trans. on Power Systems*, vol. 28, no. 3, pp. 2412-2420, Aug. 2013.
- [72] FRCC Event Analysis Team (FEAT) Interim Recommendations Report, Available online: <https://www.balch.com/files/upload/FRCC-Interim-Report-6-3-08.pdf>.
- [73] G. C. Tarnowski, P. C. Kjar, P. E. Sorensen, and J. Ostergaard, "Variable speed wind turbines capability for temporary over-production," in *Proc. IEEE Power & Energy Society General Meeting*, Calgary, Alberta, Canada, July 2009.
- [74] N.W. Miller, K. Clark, M. Shao, "Impact of frequency responsive wind plant controls on grid performance," in *Proc. 9th Annual Large-Scale Integration of Wind Power into Power Systems and Transmission Networks for Offshore Wind Power Plant*, Quebec, Canada, October 2010.

- [75] A.B.T. Attya, T. Hartkopf, "Control and quantification of kinetic energy released by wind farms during power system frequency drops," *IET Renewable Power Generation*, vol. 7, no. 3, pp. 210-224, May 2013.
- [76] M. Kayikci and J.V. Milanovic, "Dynamic Contribution of DFIG-Based Wind Plants to System Frequency Disturbances," *IEEE Trans. on Power Systems*, vol. 24, no. 2, pp. 859-867, May 2009.
- [77] I. O. Margaris, S. A. Papathanassiou, N. Hatziaargyriou, A. Hansen, P. Sorensen, "Frequency control in autonomous power systems with high power penetration," *IEEE Trans. on Sustainable Energy*, vol. 3, no. 2, pp. 189-199, April 2012.
- [78] M.F.M. Arani, E.F. El-Saadany, "Implementing Virtual Inertia in DFIG-Based Wind Power Generation", *IEEE Trans. on Power Systems*, vol. 28, no. 2, pp. 1373-1384, May 2013.
- [79] G. Ramtharan, J.B. Ekanayake, N. Jenkins, "Frequency support from doubly fed induction generator wind turbines," *IET Renewable Power Generation*, vol. 1, pp. 3-9, 2007.
- [80] L. C. Chien, W. T. Lin, and Y. C. Yin, "Enhancing frequency response control by DFIGs in the high wind penetrated power systems," *IEEE Trans. Power System*, vol. 26, no. 2, pp. 710-718, May 2011.
- [81] G. C. Tarnowski, P. C. Kjr, J. stergaard, P. E. Srensen, "Frequency control in power systems with high wind power penetration," in *Proc. 9th international workshop on large-scale integration of wind power into power systems*, Oct. 2010, Quebec, Canada
- [82] K.V. Vidyanandan, N. Senroy, "Primary frequency regulation by deloaded wind turbines using variable droop," *IEEE Trans. on Power Systems*, vol. 28, no. 2, pp. 837-846, May 2013.
- [83] E. Muljadi and C.P. Butterfield, "Pitch-controlled variable-speed wind turbine generation," *IEEE Trans. Industry Applications*, vol. 37, no. 1, pp. 240-246, Jan./Feb. 2001.
- [84] F.A. Bhuiyan and A. Yazdani, "Multimode control of a DFIG-based wind-power unit for remote applications," *IEEE Trans. Power Delivery*, vol. 24, no. 4, pp. 2079-2089, Oct. 2009.

- [85] G. Michalke, A. Hansen, T. Hartkopf, "Control strategy of a variable speed wind turbine with multipole permanent magnet synchronous generator," *European wind energy conference and exhibition*, May 2007.
- [86] H.W. Kim, S.S. Kim, H.S. Ku, "Modeling and control of PMSG-based variable-speed wind turbine," *Electric Power Systems Research*, vol. 80, issue 1, pp. 46-52, Jan. 2010.
- [87] A. Yazdani, and R. Iravani, *Voltage-Sourced Converters in Power Systems*, IEEE/John-Wiley, ISBN: 978-0-470-52156-4, 464 pages, Feb. 2010.
- [88] E. Spooner and A.C. Williamson, "Direct coupled, permanent-magnet generators for wind turbine applications," *Electric Power Applications, IEE Proceedings*, vol. 143, no. 1, pp. 1-8, Jan. 1996.
- [89] S. Morimoto, H. Nakayama, M. Sanada, Y. Takeda, "Sensorless output maximization control for variable-speed wind generation system using IPMSG," *IEEE Transaction on Industry Applications*, vol. 41, no. 1, pp. 60-67, Jan./Feb. 2005.
- [90] PSCAD/EMTDC v. 4.2, Manitoba HVDC Research Centre, Winnipeg, MB, Canada.
- [91] H. Geng, D. Xu, and G. Yang, "Comparison of oscillation damping capability in three power control strategies for PMSG-based WECS," *Wind Energy*, vol. 14, pp. 389-406, 2011.
- [92] I. Erlich, and M. Wilch, "Primary Frequency Control by Wind Turbines," *IEEE Power and Energy Society General Meeting*, July 2010.
- [93] EnerNex Corporation, *Eastern wind integration and transmission study*, Prepared for the National Renewable Energy Laboratory (NREL), Revised February 2011, Available online: <http://www.nrel.gov/docs/fy11osti/47078.pdf>.

# Curriculum Vitae

**Name:** Omid Alizadeh

**Post-Secondary Education and Degrees:** Western University  
London, ON, Canada  
2008 - 2014, Ph.D. in Electrical Engineering

University of Tehran  
Tehran, Iran  
2005 - 2008, M.Sc. in Electrical Engineering

K.N. Toosi University of Technology  
Tehran, Iran  
2001 - 2005, B.Sc. in Electrical Engineering

## Related Work

**Experience:** • Research and Teaching Assistant, Western University, 2008-2014.

## Publications:

- O. Alizadeh, A. Yazdani, "A control strategy for power regulation in a direct-drive WECS with flexible drive-Train," revised and resubmitted to *IEEE Trans. on Sustainable Energy*, Feb. 2014.
- O. Alizadeh, A. Yazdani, "Enhanced control of a WECS for contribution to power system frequency response," submitted to *IEEE Trans. on Power Systems*, Nov. 2013.
- O. Alizadeh, A. Yazdani, "A strategy for real-power control in a direct-drive PMSG-based wind energy conversion system," *IEEE Trans. on Power Delivery*, vol.28, no.3, pp.1297-1305, Jul. 2013.
- O. Alizadeh, A. Yazdani, "Enhancing frequency response by PMSG-based wind turbines," presented in the 28th Canadian Wind Energy Association Annual Conference & Exhibition, Toronto, Canada, Oct. 2012.